

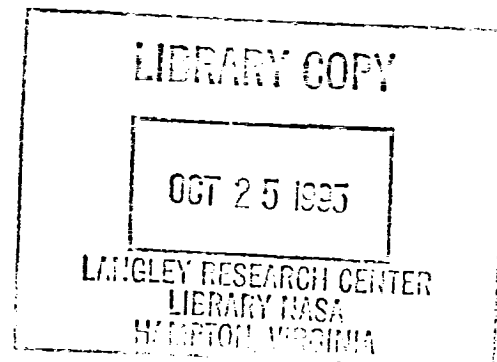
Feasibility of Coupling Between a Single-Mode Elliptical-Core Fiber and a Single Mode Rib Waveguide Over Temperature

Margaret L. Tuma
Lewis Research Center
Cleveland, Ohio

October 1995



National Aeronautics and
Space Administration





FEASIBILITY OF COUPLING BETWEEN
A SINGLE-MODE ELLIPTICAL-CORE FIBER AND
A SINGLE MODE RIB WAVEGUIDE OVER TEMPERATURE

A Dissertation
Presented to
The Graduate Faculty of The University of Akron

In Partial Fulfillment
of the Requirements for the Degree
of Doctor of Philosophy

Margaret L. Tuma
August 1995

ABSTRACT

To determine the feasibility of coupling the output of an optical fiber to a rib waveguide in a temperature environment ranging from 20°C to 300°C, a theoretical calculation of the coupling efficiency between the two was investigated. This is a significant problem which needs to be addressed to determine whether an integrated optic device can function in a harsh temperature environment. Because the behavior of the integrated-optic device is polarization sensitive, a polarization-preserving optic fiber, via its elliptical core, was used to couple light with a known polarization into the device. To couple light energy efficiently from an optical fiber into a channel waveguide, the design of both components should provide for well-matched electric field profiles.

The rib waveguide analyzed was the light input channel of an integrated-optic pressure sensor. Due to the complex geometry of the rib waveguide, there is no analytical solution to the wave equation for the guided modes. Approximation or numerical techniques must be utilized to determine the propagation constants and field patterns of the guide. In this study, three solution methods were used to determine the field profiles of both the fiber and guide: the effective-index method (EIM), Marcatili's approximation, and a Fourier method. These methods were utilized independently to calculate the electric field profile of a rib channel waveguide and elliptical fiber at two temperatures, 20°C and 300°C. These temperatures were chosen to represent a nominal and a high temperature that the device would experience.

Using the electric field profile calculated from each method, the theoretical coupling efficiency between the single-mode optical fiber and rib waveguide was calculated using the overlap integral and results of the techniques compared. Initially, perfect alignment was assumed and the coupling efficiency calculated. Then, the coupling efficiency calculation was repeated for a range of transverse offsets at both temperatures. Results of the calculation indicate a high coupling efficiency can be achieved when the two components were properly aligned. The coupling efficiency was more sensitive to alignment offsets in the y direction than the x , due to the elliptical modal profile of both components. Changes in the coupling efficiency over temperature were found to be minimal.

ACKNOWLEDGEMENTS

The author wishes to thank her employer, the NASA Lewis Research Center, and its personnel for encouraging me to pursue my doctorate. Also appreciated was the time and effort put forth by the members of my dissertation committee. Thanks are extended to my advisor, Dr. Nathan Ida, for suggestions regarding this research. The author greatly appreciates contributions from Dr. Joseph Boyd and Gregory De Brabander, from the University of Cincinnati, for the design and fabrication of the sensor.

TABLE OF CONTENTS

LIST OF TABLES	x
LIST OF FIGURES.	xi
NOMENCLATURE	xv
CHAPTER	
I. INTRODUCTION	1
1.1 Fiber Optic and Integrated Optic Benefits.	1
1.2 Dissertation Objectives.	3
1.3 Organization	5
II. BACKGROUND INFORMATION	6
2.1 Introduction	6
2.2 Previous Research	6
2.2.1 Rib Field Calculation	7
2.2.2 Fiber Field Calculation.	10
2.2.3 Coupling Efficiency	11
2.3 Ring Resonator	17
III. COUPLING COMPONENTS - RIB GUIDE AND ELLIPTICAL FIBER.	19
3.1 Introduction	19
3.2 Rib Waveguide	19
3.2.1 Materials	19
3.2.2 Substrate and Isolation Layer	20
3.2.3 Guiding Layer	21

3.2.4 Overlayer.	23
3.2.5 Deposition Procedure.	23
3.2.6 Parameter Variations with Temperature . . .	25
3.3 Fiber	28
3.3.1 Characteristics	28
3.3.2 Physical Parameters	30
3.3.3 Parameter Variations with Temperature . . .	31
3.4 Summary	31
IV. METHODS USED TO DETERMINE THE ELECTRIC FIELD PROFILES	33
4.1 Introduction	33
4.1.1 Three-Layer Planar Waveguide - Analytical Solution	33
4.1.2 TE Mode Development - Guided Modes.	35
4.1.3 TE Results for a Planar Waveguide - Guided Modes	38
4.1.4 TM Results - Guided Modes.	39
4.1.5 Radiation Modes	40
4.1.6 Rib Waveguide	40
4.1.7 Elliptical-Core Fiber	42
4.2 Methods	43
4.2.1 Effective-Index Method (EIM).	46
Rib Waveguide	46
Fiber Field - EIM	52

4.2.2	Marcatili's Method	53
	Rib Waveguide	53
	Perturbation Correction - Guide Effective Index.	57
	Marcatili - Fiber Electric Field. . . .	58
	Perturbation Correction - Fiber Effective Index.	59
4.2.3	The Fourier Method60
	Rib Waveguide.60
	Fiber Field - the Fourier Method. . . .	62
	Fourier Method - Validity	63
4.3	Coupling Efficiency Calculation69
4.4	Concluding Remarks	75
V.	RESULTS76
5.1	Rib Waveguide Results (20°C).76
	5.1.1 Field Results76
	5.1.2 Effective Index Results - Rib77
	5.1.3 Comparison	79
5.2	Fiber Results (20°C).79
	5.2.1 Field Results79
	5.2.2 Effective Index Results - Fiber81
	5.2.3 Comparison	83
5.3	Coupling Efficiency Results83

5.4 Rib Waveguide Results - 300°C87
5.4.1 Physical Changes Due to Temperature87
5.4.2 Field Results - Rib89
5.4.3 Effective-Index Results - Rib91
5.4.4 Comparison - Rib.91
5.5 Fiber Results - 300°C91
5.5.1 Physical Changes Due to Temperature Increase.91
5.5.2 Field Results93
5.5.3 Effective Index Results - Fiber93
5.5.4 Comparison of Fiber Results94
5.6 Coupling Efficiency Results95
5.7 Coupling Efficiency Optimization.97
5.8 Coupling Efficiency Results97
VI. CONCLUSION.	100
6.1 Summary	100
6.2 Significance of Work.	101
6.3 Future Work	102
REFERENCES104

LIST OF TABLES

3.1	Temperature Dependence of Silicon and Silicon Dioxide	32
3.2	Parameter Change Calculation.	32
3.3	Parameter Change Calculation for Fiber	32
4.4	Effective Index Results.	75
5.5	Rib Effective Index Results (20°C).	78
5.6	Fiber Effective Index Results (20°C)	82
5.7	Maximum Coupling Efficiency (20°C)	88
5.8	Rib Guide Parameter Changes with Temperature	88
5.9	Rib Effective Index Results (300°C)	92
5.10	Fiber Parameter Changes With Temperature	92
5.11	Fiber Effective Index Results (300°C)	92
5.12	Maximum Coupling Efficiency (300°C)	96

LIST OF FIGURES

2.1	V-groove in silicon for fiber alignment.	14
2.2	Silicon v-groove coupling structure with tapered fibers for improved alignment.	15
2.3	Integrated optic ring resonator interferometer.	18
3.4	Cross sections of rib waveguide and elliptical-core optical fiber.	20
3.5	SiO ₂ isolation layer thickness vs. SiON guide thickness. . .	22
3.6	Guide effective index calculated for various SiO ₂ overlayer thicknesses.	24
3.7	Three layer structure for analysis.	25
4.8	Three-layer planar waveguide.	34
4.9	Rib waveguide.	42
4.10	Channel waveguide structure.	43
4.11	Buried rib waveguide structure.	44
4.12	EIM constituent slab waveguides.	47
4.13	EIM separable refractive index profile shown in its respective region - shorter dimension analyzed first.	50
4.14	EIM separable refractive index profile shown in its respective region - longer dimensions analyzed first.	51
4.15	Elliptical-core fiber with pseudo-guide (rectangle).	53

4.16 Marcatili's method: pseudo-guide used to approximate rib guide.	54
4.17 Elliptical-core fiber with regions defined for perturbation cor- rection to the propagation constant.	59
4.18 E^2 at $(\frac{L_x}{2} - 0.05, \frac{L_y}{2})$ vs. box size	64
4.19 $E^2(x, y)$ vs. number of expansion terms at a point.	64
4.20 Rib waveguide field magnitude at $x = 0$ vs. y calculated using the Fourier method.	65
4.21 Rib waveguide field magnitude at $x = \frac{W}{2}$ vs. y calculated using Galerkin's method.	66
4.22 Geometry of rib 1 from Robertson paper	67
4.23 Electric field contour plot calculated using finite difference method.	67
4.24 Electric field contour plot calculated using the EIM.	68
4.25 Electric field contour plot calculated using the Fourier method	68
4.26 Geometry of rib 2 from Kolk paper	69
4.27 Field intensity contour plot for rib 2.	70
4.28 Field intensity contour plot for Rib 2.	71
4.29 Circular-core fiber and rectangles used for approximation. . .	71
4.30 Field amplitude versus radial distance for circular-core optical fiber.	72
4.31 Exact field solution for circular-core fiber.	73
5.32 EIM: electric field contours of rib guide.	77

5.33	Marcatili's method: electric field contours of rib guide. . . .	78
5.34	Fourier Method: electric field contours of rib guide.	78
5.35	Difference between Fourier field result and EIM field result for the rib waveguide.	80
5.36	Difference between Fourier field result and Marcatili's field result for the rib waveguide.	80
5.37	EIM: electric field contours of elliptical-core fiber.	81
5.38	Marcatili's method: electric field contours of elliptical fiber. .	82
5.39	Fourier method: electric field profile of elliptical-core fiber. .	82
5.40	Difference between Fourier field result and EIM's field result for the elliptical-core fiber.	84
5.41	Difference between Fourier field result and Marcatili's field result for the elliptical-core fiber.	85
5.42	Calculated coupling efficiency vs. x offset.	86
5.43	Calculated coupling efficiency vs. y offset.	86
5.44	EIM: electric field contours of rib at 300°C.	89
5.45	Marcatili's method: electric field contours of rib at 300°C. .	90
5.46	Fourier method: electric field contours of rib at 300°C. . . .	90
5.47	EIM: electric field contours of fiber at 300°C.	93
5.48	Marcatili's method: electric field contours of fiber at 300°C.	94
5.49	Fourier method: electric field contours of fiber at 300°C. . .	95
5.50	Calculated coupling efficiency vs. x offset at 300°C.	96
5.51	Calculated coupling efficiency vs. y offset at 300°C.	98

5.52 Optimum rib waveguide coupling efficiency vs. x offset from the preliminary study.	98
5.53 Optimum rib waveguide coupling efficiency vs. y offset from the preliminary study.	99

NOMENCLATURE

$2a$	Elliptical-core major axis diameter
$2b$	Elliptical-core minor axis diameter
β	Propagation constant of wave within a waveguide
BPM	Beam Propagation Constant
CW	Continuous Wave
\mathbf{E}	Electric field vector
EIM	Effective-Index Method
$E_x(x, y)$	Electric field profile
ϵ_o	Permittivity of free space
\mathbf{H}	Magnetic field vector
k_o	Defined as $\frac{2\pi}{\lambda_o} = \omega\sqrt{\epsilon_o\mu_o}$
λ_o	Free space wavelength of light source (830 nm)
LiNbO ₃	Lithium Niobate
LPCVD	Low Pressure Chemical Vapor Deposition
NA	Numerical Aperature
n_1	Index of refraction of guiding layer
n_2	Index of refraction of substrate
n_3	Index of refraction of overlayer

n_{core}	Index of refraction of fiber core
n_{clad}	Index of refraction of fiber cladding
n_e	Effective index of a medium
PECVD	Plasma Enhanced Chemical Vapor Deposition
Q	Quality Factor
SiON	Silicon Oxynitride
SiO ₂	Silicon Dioxide
Si	Silicon
TE	Transverse Electric field
TM	Transverse Magnetic field
μ_o	Permeability of free space

CHAPTER I

INTRODUCTION

1.1 Fiber Optic and Integrated Optic Benefits

Transmitting fields via lossless dielectric cylinders was theoretically demonstrated as early as 1910 [1]. This concept was not experimentally studied until the advent of low-loss optical fiber [2], which has revolutionized the communication industry. Copper telephone wires are now being replaced by optical fibers due to benefits which include: fewer repeaters required compared to electrical wires over the same distance; larger amounts of information transmitted over smaller diameter fibers due to the higher bandwidth; and an improved signal to noise ratio.

The advantages seen in communications can be applied to aeronautics. On an airplane, optical sensors can be located remotely from the processing electronics with a fiber connection. Since optical sensors can be made compact, they can non-intrusively detect environmental parameters. These sensors are inherently immune to electromagnetic interference (EMI), such as radar, which can corrupt an electrical sensor's performance. This is a very important property because sensors are often required to operate in harsh electromagnetic environments. To use electrical sensors in these environments requires additional components for proper shielding. For aeronautics applications, this added shielding increases the weight of an aircraft, which is an undesired result as added weight reduces the amount of passengers and cargo that can be transported as well as the aircraft range and speed [3]. Unlike electric

wires and sensors, optical fibers and sensors do not exhibit sparking, short circuit, or fire hazards caused by the degradation of the wire insulation [4]. These hazards can present serious safety concerns on an aircraft. Ground loop problems are also avoided using optics which reduces noise. Transmitting sensitive information via optical fibers can improve security because the electromagnetic field strength outside a fiber is much smaller than that outside an electrical wire, thus making interception nearly impossible. Optical sensors are amenable to multiplexing, which can greatly improve efficiency. Sensors distributed in a matrix can map a measured physical parameter over the aircraft. Therefore, to replace electronic components with optical components would have wide-spread benefit. However, because this technology is still maturing, it is more expensive than its electrical counterpart and hence not widely utilized.

For aeronautics applications, an optical sensor must perform to its design specifications while located in a hostile environment. This is a challenge because if not properly designed, the high temperatures of an aircraft engine can seriously degrade or destroy the device. Modeling has become an important tool in predicting the waveguide's behavior with temperature. To model the behavior of an optical device over temperature, changes in both the refractive index of the layers and the physical dimensions must be determined. Temperature-induced changes in the materials due to thermal expansion and stress must be taken into account in order to determine the device properties at an elevated temperature.

This research explored the coupling efficiency between a single-mode optical fiber and a rib waveguide. Single mode sensors are generally more sensitive than multimode sensors, which was one of the main reasons it was desirable to determine the coupling feasibility between single-mode components. The optical fiber transmits the source light into the guide, which serves as the input to an integrated optic pressure sensor. Due to the geometry of these two components, approximation and numerical techniques have been used to determine the electric field profiles and hence the theoretical coupling efficiency. Because this sensor is to be used in a temperature varying environment on an airplane, changes in the coupling efficiency over temperature are of interest.

1.2 Dissertation Objectives

Presently, single-mode fibers and waveguides are not considered viable for use in an aircraft environment due to the coupling problem [5],[6]. The majority of devices are not optimized for coupling, resulting in reduced maximum coupling efficiency, such that a slight misalignment drastically reduces the power transfer. Thus, the results of fiber to rib guide coupling are a critical factor in predicting device feasibility because a sufficient amount of input light power is required for the waveguide output to be detected. If theoretical calculations indicate a high interconnect loss, then modifications must be made prior to fabrication with the goal to improve the coupling efficiency.

Calculating the theoretical coupling efficiency between an elliptical-core optical fiber and a rib waveguide at two temperature conditions with various alignment

positions, to determine interconnect feasibility, was the objective of this research. To do so required the calculation of the electric field profiles of both components in order to evaluate the well-known overlap integral. Because there is no analytical solution to the field of the rib guide, two approximation and one numerical technique were used and the results of these techniques for the rib were compared. The two approximation techniques chosen, the EIM [7],[8],[9],[10],[11],[12] and Marcatili's method [10],[13],[14],[15], are widely accepted techniques that have been extensively studied. The numerical technique, the Fourier method, was chosen due to its reported excellent agreement with known exact solutions [16].

The fiber field can be calculated analytically using a series of Mathieu functions [2], however, the solution cannot be determined in closed form because the eigenvalue equation involves infinite determinants [17]. It was determined that the same methods used to calculate the rib guide characteristics were applicable to the fiber [16],[17],[18].

The effective index, n_e , related to the modal propagation constant, is a result of the field calculation and was used for comparison purposes. Both the n_e and coupling efficiency calculations were performed at the two temperatures. As a consequence, it was necessary to determine the index and physical dimensions of both components at the two temperatures, producing a different field profile for each.

The two temperatures were chosen to represent a nominal temperature and a high temperature that such a device would experience near the inlet of an aircraft engine [4]. The maximum theoretical coupling efficiencies at each temperature were compared to determine if the temperature change was significant to affect the sensor performance.

1.3 Organization

The organization of this dissertation is briefly outlined here. Chapter II provides an overview of documented research related to this dissertation. A brief description of the sensor whose input is being studied is also given in Chapter II. The fiber and sensor physical parameters are discussed in Chapter III along with the physical parameters' behavior with temperature. In Chapter IV the three methods used to calculate the electric field profiles of both the fiber and rib waveguide are discussed. Chapter V is divided into two parts, room temperature (20°C) and 300°C results. These results include the field profiles and corresponding coupling efficiency results for transverse offsets. Using the three methods independently, the results were compared. A discussion on maximizing the theoretical coupling efficiency by altering the waveguide parameters is given in Chapter V. The conclusion and plans for future work are discussed in Chapter VI. A list of acronyms used with corresponding definitions is provided in the on page xv.

CHAPTER II

BACKGROUND INFORMATION

2.1 Introduction

This chapter describes previous research and is divided into rib, fiber, and coupling efficiency subsections which provide an overview of the research regarding field solutions required to calculate fiber to guide coupling. The first two subsections explore the field profile calculations documented to date on the two coupling components. The third subsection discusses research on the coupling efficiency between a fiber and a rib waveguide. A few specific examples from the literature survey will be explored to illustrate the differences between previous research and that of this dissertation. A brief description of the pressure sensor for which the rib waveguide is the light input is also given.

2.2 Previous Research

The problem of transmitting the output light from a fiber into an integrated optic device is relatively new. Until the advent of low loss fibers in the 1960's, it was impractical to attempt coupling, as the fiber exhibited such high loss. The communications industry has addressed this coupling issue extensively for lithium niobate (LiNbO_3) devices. Results from the literature search performed in preparation for this research will be discussed.

The majority of the research calculates the propagation characteristics of either an optical fiber or a waveguide. For this calculation, there are many techniques

from which to choose. These methods include: finite element method, EIM, Marcanti's method, Fourier method, variational method, and beam propagation method (BPM).

2.2.1 Rib Field Calculation

Due to the complex geometry of the rib waveguide, approximation or numerical solution techniques are necessary to determine its propagation characteristics. Two review articles, one by Chiang [19] and the other by Saad [20], discuss the methods that have been used to solve for the propagation characteristics of waveguides. A discussion of several of the methods will be given.

The EIM has been used to calculate the profile of a rib [8],[11],[19]. Caution must be exercised when using this technique, because inaccurate results may occur if applied to a device which does not meet the approximation assumptions. For example, field boundary conditions are not satisfied using this approximation technique [10]; thus narrow ribs are not accurately modeled using this method. Determination of the accuracy of this method relies upon comparison with a numerical technique [21]. The EIM is known to be accurate for ribs with small etch depths, such as the rib under study. However, it consistently yields propagation constants that are larger than those provided by the numerical results. Because this technique is only applicable to a specific rib geometry, it is not widely recognized as useful for field calculations, but rather only for the determination of the propagation constant [10]. However, this remains one of the most popular techniques for the analysis of rectangular structures. Variations on this method are numerous [22],[23],[24],[25],[26] with the intent to improve results.

Marcatili's method [13] has been applied to both rib and strip-loaded waveguides. Results from this technique compared well with numerical solutions [14],[15]. This method assumes the field is tightly confined to the core such that the field in the outer regions is negligible. The technique has even been applied to modes in anisotropic rectangular waveguides [27]. A perturbation correction to the propagation constant calculated using Marcatili's method can improve the accuracy [14]. A perturbation correction can also be applied to the EIM [28]. The major advantage of the EIM and Marcatili's technique is their simplicity.

Goell [29] reported a numerical technique based on the expansion of circular harmonic functions. This method produces accurate results for the propagation constant, but becomes cumbersome for devices with aspect ratios other than unity. Many researchers refer to Goell's work for comparison, yet it is infrequently used.

The finite element method is an application of the Rayleigh-Ritz procedure to a set of basis functions which are confined to a small spatial region [30]. When applied properly, this method has been determined to be very accurate and can be applied to many geometries [31]; unfortunately, it requires an enormous amount of computing resources.

The variational method has also been applied to a rib guide to determine the rib field profile. The accuracy of this technique is dependent upon the choice of the trial field function. Taking the trial function and varying its constants until an integral relation with the propagation constant is maximized, produces the field result. This is an application of the Rayleigh-Ritz procedure based on an expansion of a set of independent basis functions [30]. An integral relation is derived from the

scalar wave equation and defined as

$$\beta^2 = \frac{k_o^2 \int n^2(x, y) |\Phi(x, y)|^2 da - \int |\nabla_t \Phi(x, y)|^2 da}{\int |\Phi(x, y)|^2 da}, \quad (2.1)$$

where the integration is taken over the guide cross section, $\Phi(x, y)$ is the field trial function, and k_o is defined as $\frac{2\pi}{\lambda_o}$ where λ_o is the wavelength in free space. The variational method has received a fair amount of attention recently [32],[33],[34].

The beam propagation method (BPM) is used to solve the scalar equation and cannot be adapted to solve the vector wave equation. Yevick and Hermansson compared the results of the finite element method with the beam propagation method [30]. Accurate results can be obtained for straight guides, but the BPM becomes inaccurate when applied to curved sections. The BPM is particularly useful for determining the coupling between two adjacent, parallel waveguides.

The Fourier method has also been applied to a rib waveguide [35],[36],[37]. The electric field is calculated using a series of sine functions. Inserting this field expansion into the scalar wave equation and exploiting the orthogonality produces a matrix equation. Using sine basis functions, the boundary condition of zero field at infinity is not satisfied. Thus, the field must be enclosed in an artificial rectangular boundary, such that the accuracy of the results depends on its size [16] and the number of expansion terms used.

After exploring the different methods for determining the field profile of a rib waveguide, three methods were chosen. The EIM and Marcatili's approximation method were chosen because both have demonstrated accurate results for a rib waveguide. The Fourier method was chosen as the numerical technique because it produces

smaller matrix equations than the other numerical techniques [16]. This reduces the computing time required for the calculations, while maintaining accuracy. Due to the flexibility of the three chosen techniques, they can be applied to both coupling components.

2.2.2 Fiber Field Calculation

The exact solution for the propagation characteristics of an elliptical-core fiber involves complicated transcendental dispersion equations. These equations require numerical analysis to determine the fiber propagation constants. Consequently, most of the recent work on elliptical-core fibers has been based on approximation or numerical techniques [38].

Yeh [2] provided an exact analysis of an elliptical-fiber using Mathieu and modified Mathieu functions. From this analysis, a numerical technique is needed to produce the solutions. Using Yeh's analysis, Dyott et. al. [39] developed a computer program to solve for the propagation characteristics of the fiber using the finite element method. This solution is very complex and is not conducive to the coupling efficiency calculation.

The EIM is applicable to elliptical-core fibers [18],[40]. The solution is a set of spatially dependent analytic functions which are conducive to evaluation of the overlap integral. Fiber birefringence can also be calculated using this method.

Another approximation method which can be applied to the fiber is Marcanti's technique [41],[42]. This method has been proven to accurately predict the propagation behavior of a highly elliptical-core fiber [43]. Birefringence results using this method compared favorably with those obtained by Dyott [39].

The Fourier method has also been used to calculate the field profile of an elliptical-core fiber. This method utilizes an orthogonal set of basis functions to convert a differential equation into a set of simultaneous linear equations [44],[35]. Results from this method accurately predicted the modal propagation constant and the field profile when compared with known results.

From the above solution methods, the EIM, Marcatili's approximation, and the Fourier method were chosen for this study. Both the EIM and Marcatili's approximation methods have been successfully applied to elliptical-core fibers. The numerical technique chosen was the Fourier method, based on its accurate results for elliptical fibers. Also, knowing a priori that (1) the Fourier method was chosen for the rib field calculation and (2) the overlap integral calculation was to be performed, choosing the Fourier method as the numerical technique for the fiber was a logical choice. All three methods produce field solutions conducive to calculating the overlap integral.

2.2.3 Coupling Efficiency

The goal of this research was to determine the feasibility of coupling light from an optical fiber into a rib waveguide. This required a comprehensive analysis of the propagation characteristics of both the elliptical-core fiber and rib waveguide over temperature. Results of this analysis were used to determine the theoretical coupling efficiency between the single-mode components for various alignment positions at two temperatures to determine interconnect feasibility.

There are several methods of coupling a fiber to a waveguide, which include: prisms, gratings, evanescent field coupling, lenses, and end-fire coupling. All of these

methods were explored, but the most practical approach for an aircraft was end-fire coupling [45]. Prisms or gratings require the fiber to be incident at a particular angle, which is impossible in the vibrating environment of an aircraft engine. Evanescent coupling requires the fiber to be stripped of its cladding and placed directly on top of the guide. Scratches on the upper surface of the guide cause scattering loss and precise alignment with the $2.7\ \mu\text{m}$ wide rib is difficult. Fabricating a laser diode source directly on the device substrate [46] was not a viable option for this device since it was to operate in a temperature range from 20°C to 300°C , because the output wavelength of the laser diode would shift with temperature, corrupting the device output. End-fire coupling requires the fiber tip to be in physical contact with the guide cross section and precisely aligned, which is the most feasible coupling method for this application.

Burns and Hocker [47] explored end-fire coupling in 1977, and discussed the issue of mode mismatch between components, which decreases the coupling efficiency. The coupling efficiency depends on the spatial overlap of the transverse fields of the optical modes in the fiber and channel guide, therefore any differences between their field profiles will produce a loss. The calculations performed by Burns and Hocker [47] approximated the fields of both components as Gaussian, to simplify the integral calculation.

Approximating the fields of the two coupling components greatly simplifies the evaluation of the overlap integral. A closed form solution has been derived using the Gaussian approximation [48]. From this solution, the coupling efficiency between a GaAlAs laser diode and a LiNbO_3 device was determined.

Ghosh [49] performed an interesting theoretical probability analysis of the alignment between two components. Using a circular-core fiber which was smaller than the circular device, the probability of alignment was determined. For this case, 100% coupling efficiency was possible because the fiber was smaller than the device. As long as the fiber was positioned entirely within the device cross-section, 100% coupling efficiency is achieved. This geometry was in contrast with the case under study where the fiber is larger than the device, being nearly two times as high. Thus, 100% coupling efficiency can never be obtained for the device being studied.

The majority of coupling research used LiNbO_3 for the waveguide, however, this material cannot be operated at high temperatures. Also, circular-core single mode fibers were used as the light input, thus simplifying the theoretical coupling calculation. Most papers simplified the coupling efficiency calculation by assuming the field of one or both of the components as Gaussian [50],[51].

Chung [52] addressed the problem of experimentally aligning the fiber with the guide, as well as the need for a polished waveguide end face to reduce scattering. The use of grooves fabricated directly on the waveguide for fiber placement improved alignment. A v-groove configuration is illustrated in Figure 2.1, where the angle θ is the crystallographically defined angle of silicon. This approach is widely accepted and has been extensively used [53],[54]. Using v-grooves for fiber alignment is considered a self-alignment technique, because it reduces the necessary active alignment to one direction, z . Using LiNbO_3 devices, Murphy and Rice [55] experimentally fabricated a multiple fiber-waveguide alignment technique using a series of v-grooves on silicon. This design is suitable for both single-mode and multi-mode fibers. The required

groove width can be calculated using

$$w_o = \sqrt{6}r - 2\Delta, \quad (2.2)$$

where w_o is the groove width, r is fiber radius and Δ is the distance from the silicon surface to the center of the fiber core. In practice, groove widths can be controlled to $\pm 1 \mu m$; this variation in the groove width produces a transverse offset causing coupling loss. The coupling efficiency was theoretically calculated assuming Gaussian mode profiles for both the fiber and waveguide. The fiber/guide system was thermally cycled between $20^\circ C$ and $70^\circ C$, with minimal coupling efficiency change.

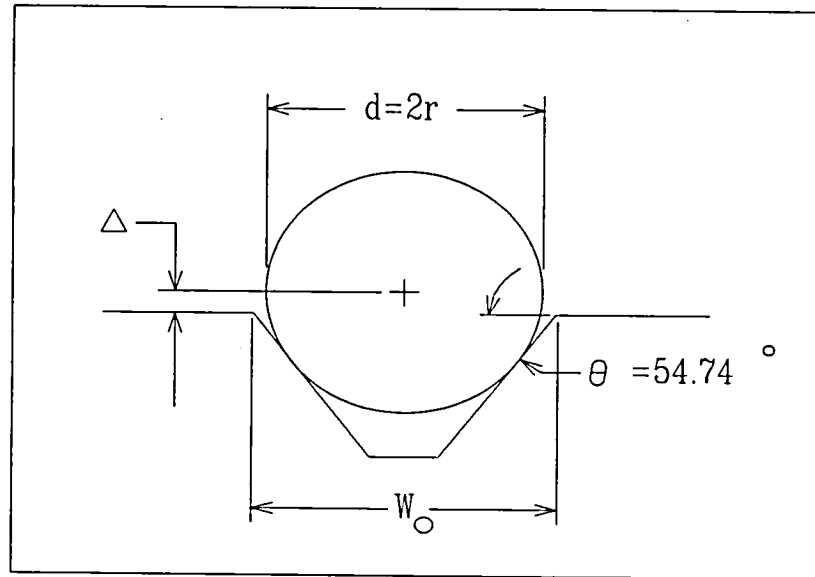


Figure 2.1: V-groove in silicon for fiber alignment.

For alignment improvement, a fiber with a tapered diameter can be inserted in the groove and translated until the maximum coupling efficiency is achieved [56]. This scheme is illustrated in Figure 2.2. Using a LiNbO_3 device, coupling efficiencies of 70% or more have been experimentally achieved with this configuration [56].

Flip-chip alignment is similar to the v-groove concept. V-grooves in the substrate chip are used to align the fiber while another v-groove chip is placed on top and upside down such that the v-grooves are aligned. This method keeps the fiber(s) more securely in place.

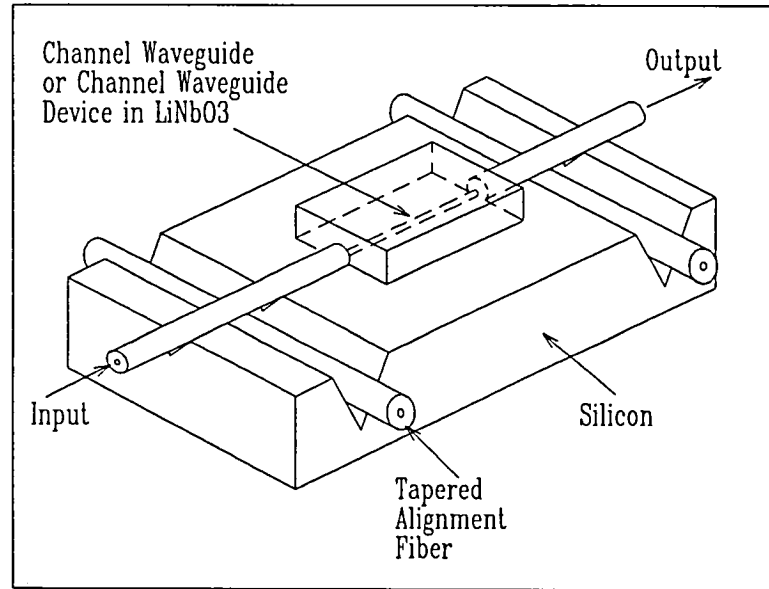


Figure 2.2: Silicon v-groove coupling structure with tapered fibers for improved alignment.

Fabricating a lens on a fiber tip to improve field matching between the components is theoretically feasible, but experimentally difficult to achieve. Cai et. al. proposed the utilization of a coupling waveguide to improve field matching between

a single-mode fiber and a thin-film waveguide [57]. A $10\ \mu\text{m}$ core polarization-maintaining fiber and $1.2\ \mu\text{m}$ thick guide were used for coupling, which are much larger than the components being studied, with a calculated coupling efficiency of 64%.

More recent research involves gallium arsenide (GaAs) waveguide devices [54],[58]. Vezzetti and Munowitz [59] explored coupling between a single-mode circular-core fiber and a strip-loaded waveguide composed of GaAs using the Fourier method. They maximized the predicted coupling efficiency by altering the strip-loaded waveguide physical dimensions and indices so that its field more closely matched that of a circular-core fiber. Their research differed from this dissertation in that (1) the waveguide was a strip-loaded channel, (2) the fiber was circular-core, (3) the material used was GaAs, and (4) parameter changes with temperature were not explored.

Experimentally, using a single-mode fiber, a 0.5 dB coupling loss to a GaAs device was reported, which corresponds to an 89% coupling efficiency [54]. This work was purely experimental, and no calculations of the fields of the components were performed. Another experimental group used a polarization-maintaining fiber and determined the coupling efficiency between it and a LiNbO_3 device. Intrinsic loss due to the field mismatch was approximately 0.5 dB [53].

A relevant paper compared the calculated coupling efficiency between four rib waveguides and a circular-core single-mode fiber using three different methods for the rib: the EIM, finite difference, and function fitting [60]. The function fitting method utilized the Rayleigh-Ritz procedure. The waveguide modes were assumed TE and propagating in the z direction, which are the same assumptions used in

this work. However, the fiber used in the paper was a circular-core single mode fiber having a spot size of $5\ \mu m$, with the field approximated as Gaussian. Results of the work indicated that the EIM was most accurate for ribs with small height and large widths, similar to the rib studied in this dissertation. Coupling efficiency variances due to transverse offsets and temperature change were not explored by these researchers.

Only a few researchers addressed coupling a polarization-maintaining fiber to a waveguide. Of those, most approximated the field as Gaussian, and no calculations were performed to determine the coupling efficiency versus transverse offsets [61].

Thus, of the literature surveyed, none calculated the coupling efficiency using rigorous field solution techniques for both the fiber and rib waveguide to calculate overlap integral, and then determined changes in the coupling efficiency with transverse offsets at two temperatures.

2.3 Ring Resonator

The rib channel investigated for this research was the input to a micro-machined ring resonator pressure sensor, shown in Figure 2.3. There are several modulation techniques which can be used to deduce a measurand. These have been described elsewhere [62]. For the sensor investigated, wavelength modulation was used. Light propagates from the input rib channel waveguide through the first Y -branch and is split at the second Y -branch. A portion of this light then travels around the ring where it crosses the diaphragm. The light continues around the ring to the first Y -branch and interferes with the incoming light. The effective index of the ring, n_e , is altered when the diaphragm is perturbed by an applied pressure. The

round trip phase shift of the ring is given by [63]

$$\phi = \frac{2\pi}{\lambda_o} \int_0^L n_e(l) dl, \quad (2.3)$$

where λ_o is the wavelength of the source and n_e is integrated around the perimeter of the ring having length L . At resonance, the ring and input light constructively interfere such that $\phi = 2\pi m$, where m is an integer, which causes the transmissivity of the ring resonator to be a maximum. When $\phi = 2\pi(m + \frac{1}{2})$, the transmissivity is a minimum. This sensor exhibits cross-sensitivity to temperature which may be reduced by shortening the path length [64]. Because the sensor is polarization sensitive, the input fiber must be polarization-maintaining. The ring resonator configuration can be used to measure other parameters by replacing the diaphragm in Figure 2.3 with an appropriate sensing mechanism.

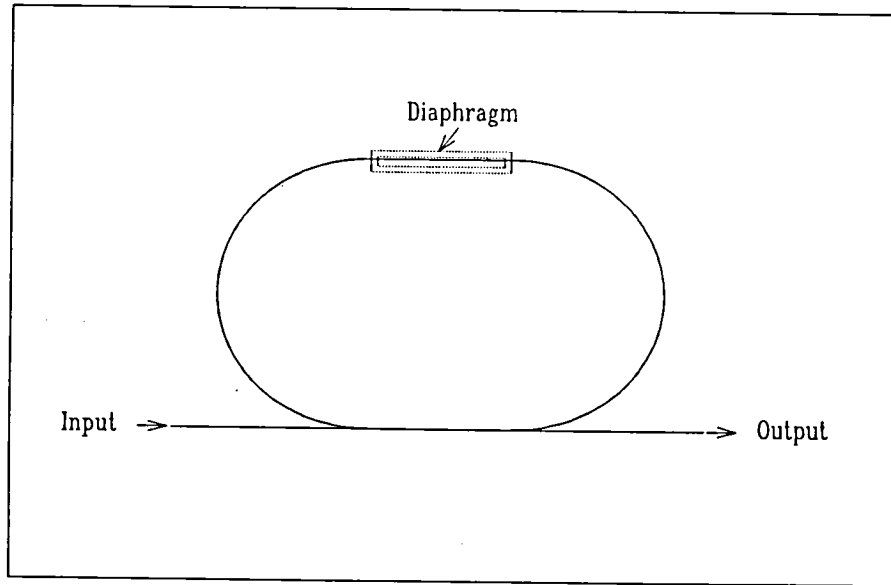


Figure 2.3: Integrated optic ring resonator interferometer.

CHAPTER III

COUPLING COMPONENTS - RIB GUIDE AND ELLIPTICAL FIBER

3.1 Introduction

The channel waveguide discussed was the input stage of an integrated-optic pressure sensor. The pressure sensor was based on a strain sensitive ring resonator, combined with a micromachined silicon diaphragm. This sensor was polarization sensitive, thus interrogation with TE or TM polarized light each produced a different output [63]. In this investigation, only the incident TE mode was analyzed. The rib guide and elliptical-core optical fiber were the two components studied such that the theoretical coupling efficiency of the light output from the fiber into the input rib guide was calculated, with the goal being to maximize the coupling efficiency between the two. Both coupling components were single mode. The sensor design and fabrication was performed at the University of Cincinnati [63]. The physical parameters of both the sensor input and elliptical-core fiber, illustrated in Figure 3.4, are discussed in the following sections.

3.2 Rib Waveguide

3.2.1 Materials

Materials for the rib waveguide were judiciously chosen, consisting of a semiconductor substrate followed by an isolation layer, guiding layer, and an overlayer. Each film layer is discussed in this order which was also the deposition order.

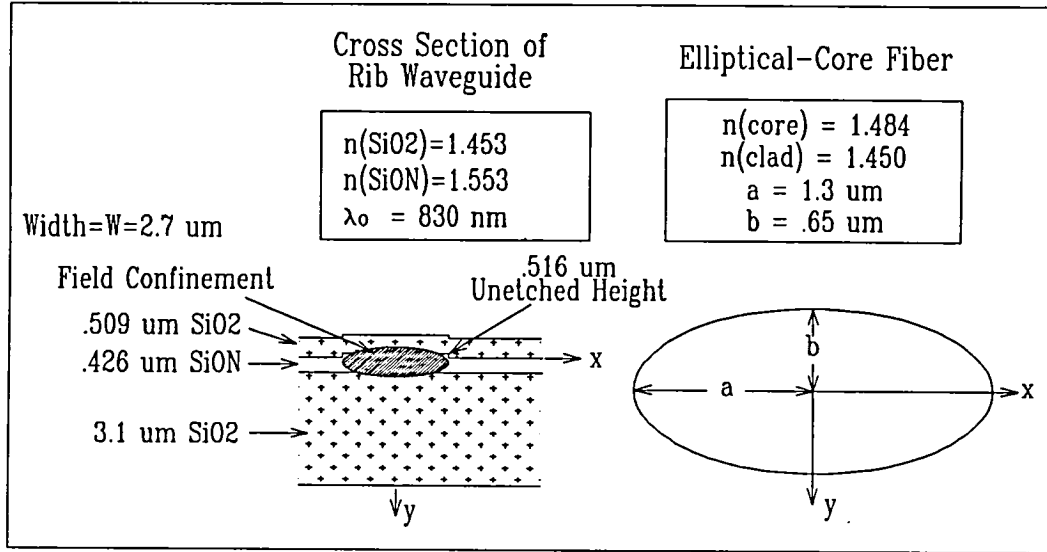


Figure 3.4: Cross sections of rib waveguide and elliptical-core optical fiber.

3.2.2 Substrate and Isolation Layer

Silicon was chosen as the substrate material due to its excellent waveguiding and mechanical properties [65]. For field confinement via total internal reflection, the index of the guiding region must be larger than the surrounding layers. The index of refraction of silicon at 830 nm is 3.67 [66] at room temperature. Because the index of all materials varies with wavelength, it is referenced to a wavelength. Unless otherwise indicated, all indices discussed in this dissertation are referenced to 830 nm. The index of silicon is higher than most candidate films used in high temperature applications. Therefore, an isolation layer of low index material must be deposited between the guiding layer and the substrate in order to utilize a silicon substrate and silicon micromachining technology. For this case, silicon oxynitride (SiON) was chosen as the guiding film, making silicon dioxide (SiO₂) a natural choice

for the isolation layer. SiO_2 is dense, smooth, highly adherent to silicon substrates, uniform in refractive index and thickness, simple to produce, has a lower index than SiON , and can be fabricated nearly defect free.

Because the isolation layer was finite, there was loss due to substrate coupling. Consequently, the waveguide's modes were not strictly bound modes, but rather leaky modes [9],[67]. To minimize this effect, the thickness of the SiO_2 layer was chosen to nearly isolate the guide from the substrate. A theoretical analysis was performed [68] to determine the required isolation layer thickness to produce a 0.1 dB/cm loss. According to the graphical results shown in Figure 3.5, the isolation layer thickness must be at least to $2.0 \mu\text{m}$ for a $0.516 \mu\text{m}$ thick guide to reduce the substrate coupling loss to 0.1 dB/cm. For the sensor, the isolation layer was $3.1 \mu\text{m}$; thus, the guiding layer did not 'see' the substrate and the effects of substrate coupling were negligible. For modeling purposes, the isolation layer was considered to be the substrate.

3.2.3 Guiding Layer

Silicon nitride, Si_3N_4 , was first explored as the waveguiding core material because of its ability to withstand high temperatures without degrading. However, it was discovered that Si_3N_4 films tend to crack for thicknesses exceeding approximately $0.2 \mu\text{m}$. Also, there is a large difference in the index of refraction between Si_3N_4 ($n \approx 2.0$) and an optical fiber ($n \approx 1.5$) which is not conducive for coupling, because Fresnel reflection would add a significant contribution to the loss. Using Si_3N_4 , the calculated coupling efficiency would generally be less than 10%, which is unacceptable for this sensor application [69].

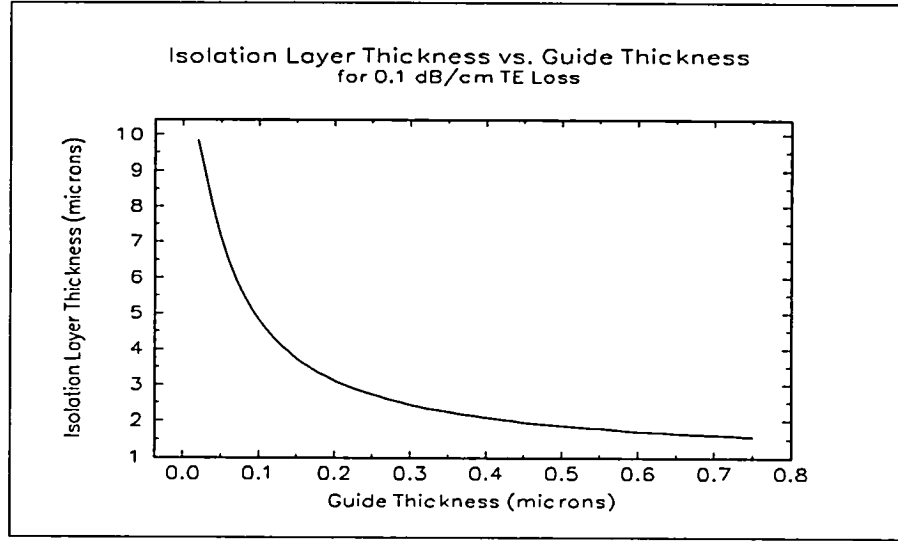


Figure 3.5: SiO_2 isolation layer thickness vs. SiON guide thickness.

To maximize the fiber-guide coupling efficiency, the cross sectional area of the two components should be nearly identical, as well as the core indices. Therefore, SiON [70],[71] was the material of choice for the guiding layer. The benefits of this material include the following: (1) film index can be varied from 1.46 - 2.02 with the fabrication process, (2) high quality deposited films, (3) ability to deposit thicker films as compared to Si_3N_4 , and (4) better index matching to optical fibers.

Ideally, the film thickness should equal that of the input fiber ($1.3 \mu\text{m}$), but Low Pressure Chemical Vapor Deposited (LPCVD) SiON films deposited thicker than approximately $0.5 \mu\text{m}$ become multimode, and cannot be used for a ring resonator sensor. The actual film thickness of the SiON layer was $0.516 \mu\text{m}$. Using photolithography, portions of the film were selectively etched to $0.426 \mu\text{m}$ to produce the rib. This etch depth was chosen to provide optimal field confinement while

maintaining a single-mode guide. The rib width was chosen to optimize the sensor performance, taking into account bends in the ring, and attempting to closely match the $2.6\ \mu\text{m}$ major axis diameter of the fiber. For the device to remain single mode it was required that the channel width be approximately $2.4\ \mu\text{m}$. A mask was designed for this width, however, due to variations in the fabrication process, the actual width was $2.7\ \mu\text{m}$. The thickness of the guide was chosen to match that of the elliptical fiber. In this study, the fiber diameters along the major and minor axes were $2.6\ \mu\text{m}$ and $1.3\ \mu\text{m}$, respectively.

3.2.4 Overlayer

An overlayer of LPCVD SiO_2 was deposited on top of the rib guide structure. This overlayer reduced the guide propagation loss by insulating the guiding film from the exposed surface, which minimized scattering effects due to surface imperfections. Similar to the isolation layer thickness, the overlayer thickness was chosen such that it appeared infinite to the guide. The effective index of a four layer guide consisting of ($\text{SiO}_2\backslash\text{SiON}\backslash\text{SiO}_2\backslash\text{air}$) was calculated for a SiO_2 overlayer thickness varying between 0 and $2.0\ \mu\text{m}$. As illustrated in Figure 3.6, there was minimal change in the effective index for an overlayer oxide thickness exceeding approximately $0.5\ \mu\text{m}$. Because the upper SiO_2 layer was $0.509\ \mu\text{m}$ thick, it was modeled as an infinite layer. Thus, the rib guide structure was modeled as a three-layer structure as shown in Figure 3.7.

3.2.5 Deposition Procedure

The fabrication process, performed at the University of Cincinnati [63], began with a 2" silicon wafer which was polished on both sides. The diaphragm was

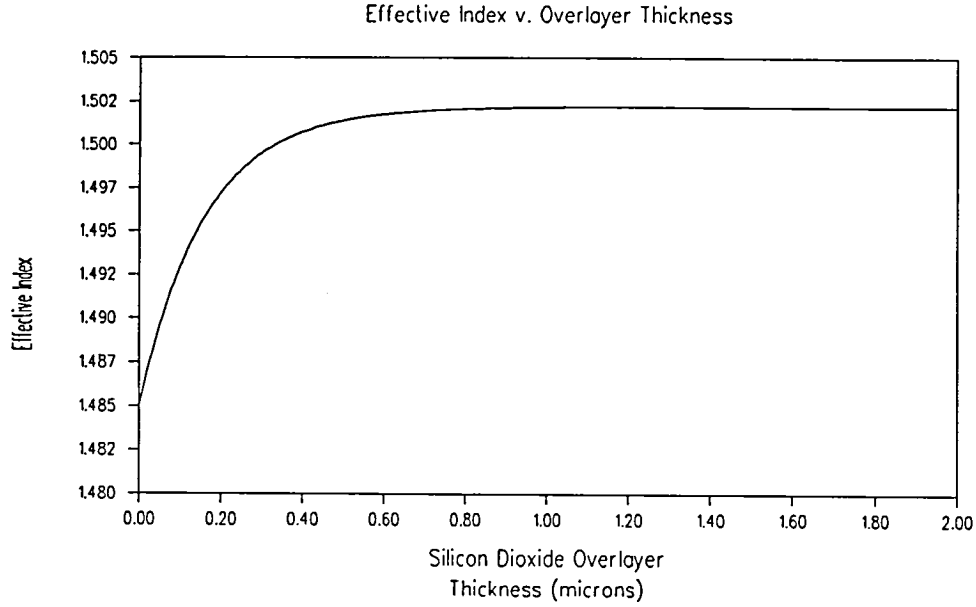


Figure 3.6: Guide effective index calculated for various SiO_2 overlayer thicknesses.

fabricated first, then the wafer was stripped of any native oxide and placed in an oxidation furnace where a thermal oxide was grown in a wet oxygen environment. After the oxide was grown to the desired thickness, the wafer was placed in an LPCVD chamber to deposit the SiON guiding layer.

Compared to other techniques, such as sputtering or Plasma Enhanced Chemical Vapor Deposition (PECVD), LPCVD produced the highest quality guiding films with the lowest loss [70],[71]. Increasing the amount of oxygen gas flow during deposition decreases the film refractive index, with the lower index limit being that of pure SiO_2 , which is 1.453 [66]. Actual film refractive index tends to vary between runs even on the same equipment using identical conditions; hence there is no standard procedure to fabricate a film with a given thickness and refractive index.

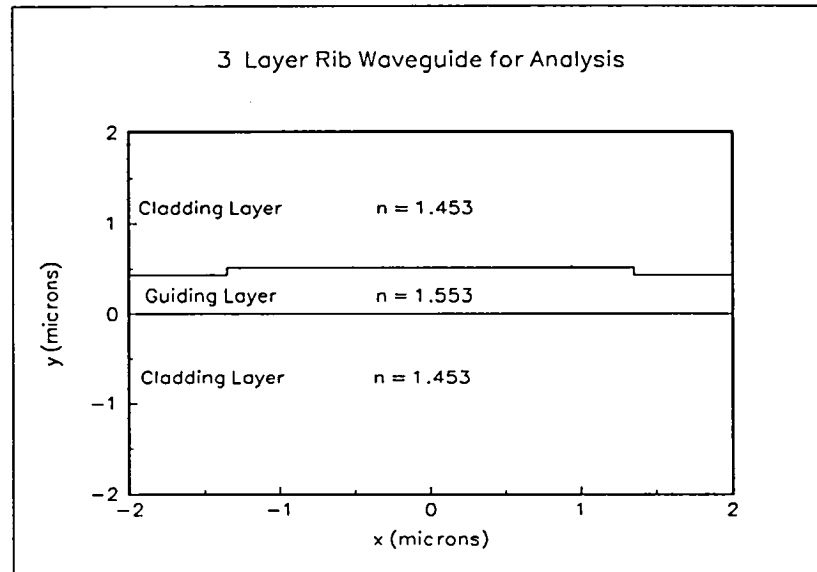


Figure 3.7: Three layer structure for analysis.

During the deposition run, the wafers were rotated to ensure uniformity of the film thickness and index.

After the guide film was deposited, the ring resonator was fabricated using photolithography. Using a mask to define the rib sections, photoresist was deposited, and the unprotected SiON regions were etched in acid by $0.9 \mu\text{m}$. After the rib was formed, an SiO_2 overlayer was deposited. Because SiO_2 films grow extremely slowly over SiON in an oxidation furnace, the SiO_2 overlayer was deposited using LPCVD.

3.2.6 Parameter Variations with Temperature

The effective index and field profile of the rib are expected to change with temperature. Three mechanisms can produce this change: (1) thermal expansion of the layers causing the width and thickness of the structure to vary, (2) stress induced

by the mismatch in the coefficient of thermal expansion of each layer, altering the refractive index via the photoelastic effect, and (3) index of refraction change with temperature. All of these mechanisms were taken into account to determine how the rib guide parameters changed with temperature [63].

For each layer of the rib waveguide, values for the thermal change in the refractive index, $\frac{dn}{dT} \left(\frac{1}{^\circ C} \right)$, coefficient of thermal expansion $\varepsilon_{thermal} \left(10^{-6} \frac{m}{m - ^\circ C} \right)$, photoelastic coefficients (p_{11} and p_{12}), and the Poisson ratio (ν) were determined. These values can be found in the literature for all the rib constituents, except SiON. Values for silicon and SiO₂ vary with temperature, with averages over temperature given in Table 3.1 [72].

Compared to SiO₂ and crystalline silicon whose thermal properties are known, SiON is not strictly defined since its index can vary from 1.453 to 2.008 [66]. Its thermal properties vary as well and are dependent upon both the substrate material and film thickness [70]. The index of the SiON layer is 1.553 and its temperature sensitivity was approximated as that of SiO₂, whose refractive index is 1.453.

For 0.1 μm thick LPCVD SiON films on quartz (SiO₂), an experimental data set indicated that the film refractive index varied with temperature as $1.5 \times 10^{-4}/^\circ C$, whereas for SiON films on a silicon substrate, it varied as $-1.1 \times 10^{-4}/^\circ C$ [70]. This rib structure had a silicon substrate with a thick SiO₂ isolation layer, hence the refractive index dependence with temperature was expected to be between these two results, which that of the SiO₂ satisfies.

The following development is from De Brabander [63]. Since the rib layers were much thinner than the silicon substrate, changes in the film dimensions parallel

to the substrate (x and z directions) were the same as that of a substrate without any films, which is,

$$\varepsilon_{x,thermal} = \varepsilon_{z,thermal} = 2.33 \times 10^{-6} \frac{m}{m - ^\circ C}. \quad (3.4)$$

If the thin SiO_2 and SiON films were removed from the substrate, they would experience a strain which is expressed as

$$\varepsilon_{x,thermal} = \varepsilon_{z,thermal} = \varepsilon_{y,thermal} = 0.55 \times 10^{-6} \frac{m}{m - ^\circ C}. \quad (3.5)$$

Hence, there is a strain parallel to the substrate face which changes the refractive index via the photoelastic effect, denoted as

$$\varepsilon_{x,photoelastic} = \varepsilon_{z,photoelastic} = (2.33 - 0.55) \times 10^{-6} \frac{m}{m - ^\circ C}. \quad (3.6)$$

The substrate stretches or compresses the film and induces an additional strain in the y direction, through Poisson coupling, which is expressed as

$$\varepsilon_{y,photoelastic} = \frac{-\nu}{1 - \nu} (\varepsilon_{x,photoelastic} + \varepsilon_{z,photoelastic}) = -0.7292 \times 10^{-7} \frac{m}{m - ^\circ C}, \quad (3.7)$$

where ν is the Poisson ratio, with value 0.17 [72].

For the rib waveguide, the thickness and index changes with temperature were small, hence applying each effect separately and adding produces the same result as applying all the effects simultaneously [63]. For example, the thickness change in the y direction is determined by the sum of the thermal and photoelastic strains, as given by

$$\varepsilon_{y,total} = \varepsilon_{y,thermal} + \varepsilon_{y,photoelastic} = -1.791 \times 10^{-7} \frac{m}{m - ^\circ C}. \quad (3.8)$$

For each parameter of interest, the expression and result for a $1^\circ C$ change of temperature is given in Table 3.2, where the abbreviation $\epsilon_{i,pe}$ where $i = x, y, \text{ or } z$ was used to denote $\epsilon_{i,photoelastic}$.

3.3 Fiber

3.3.1 Characteristics

Compared to multimode fibers, single-mode fibers have much smaller core diameters. Thus, alignment is more critical when coupling a single-mode fiber to an integrated-optic device. Circular-core single-mode fibers can be characterized as having $V < 2.40$, where V is defined as

$$V = \frac{2\pi a \sqrt{n_{core}^2 - n_{clad}^2}}{\lambda_o}, \quad (3.9)$$

and a is the core radius [74]. Due to the symmetric geometry of a circular fiber, the field profile can be approximated as Gaussian. A circular-core single-mode fiber actually propagates two orthogonal fundamental modes, corresponding to TE and TM polarization [39]. Thus, to maintain the polarization state of the input light through a fiber requires an alteration of the standard circular fiber. Preliminary calculations were conducted using the specification data from commercially available circular-core single-mode fibers. For a circular-core radius of $4 \mu m$, the calculated coupling efficiency was unacceptably low, 45% [75]. In an effort to improve the coupling efficiency, other fibers were explored.

An elliptical-core polarization-maintaining fiber was chosen because it was expected to provide the highest coupling efficiency due to its geometry and refractive index being closely matched to the guide's. Polarization-maintaining fibers can be one of two types: (1) a circular-core fiber under stress from the cladding or (2) an elliptical-core fiber. For this study, an elliptical-core fiber was used because its dimensions and field profile more closely matched that of the guide, reducing coupling loss. These types of fibers can be used in coherent optical communication systems, fiber-optic sensors, and for coupling into polarization-sensitive integrated optic devices [27]. The latter case applies to this research. Elliptical-core fibers have received more attention recently due to the availability of longer wavelength sources and detectors. Prior to this, the lower wavelengths available required the elliptical-core dimensions for polarization preservation to be too small for fabrication [39].

An elliptical core-fiber has two preferred directions of polarization; along the major axis and along the minor axis [74]. Polarized light coupled into the fiber will propagate as two orthogonal modes, denoted EH and HE. EH denotes modes with strong axial magnetic field strength, H_z , corresponding to a quasi-TE mode whereas HE denotes modes with strong axial electric field strength, E_z , corresponding to a quasi-TM mode [76]. Each mode travels at a different velocity, known as birefringence. The fiber modal birefringence is defined as [74]

$$B = \frac{(\beta_x - \beta_y) \lambda_o}{2\pi}, \quad (3.10)$$

where β_x is the TE mode propagation constant and β_y is the TM. Because $\beta_x > \beta_y$, the EH mode is more strongly guided [39].

By deliberately inducing a large degree of birefringence in a fiber, establishes a preferred polarization direction into which all the power is launched [77]. The beat length of a fiber is inversely related to its birefringence, and is defined by

$$L = \frac{\lambda_o}{B}. \quad (3.11)$$

For short beat lengths or high birefringence, transfer of power to the orthogonal mode is precluded. Hence, the output remains polarized in the direction of the preferred axis.

Highly birefringent fibers are less susceptible to mode transitions, such that the output polarization mode is the same as the input polarization. Less birefringent fibers are susceptible to perturbations in fiber dimensions and indices along its length such that an input TE polarization may transfer to the TM polarization state, which is an undesirable property for this application. Highly birefringent fibers are considered polarization-maintaining [74], the desired property for this application.

3.3.2 Physical Parameters

The fiber used was commercially available [78]. Data from the manufacturer indicated that the diameter of the major and minor axes of the core ellipse were $2.6 \mu m$ and $1.3 \mu m$, respectively. The nominal values of the core and cladding indices were 1.484 and 1.450, respectively. The numerical aperture (NA) of the fiber, defined as

$$NA = \sqrt{n_{core}^2 - n_{clad}^2}, \quad (3.12)$$

was 0.316. These parameters will vary slightly between batches, but for this study, the nominal values were used. A fiber is characterized as “weakly guiding” if the difference between the core and cladding index is small. For this fiber, the difference was approximately 2.3%, hence it can be classified as weakly guiding [76].

3.3.3 Parameter Variations with Temperature

The elliptical-core fiber investigated had a silica cladding with a germanium doped core. Generally, the cladding material has a slightly higher coefficient of thermal expansion than the core [79]. However, lacking data for the doped core, the same coefficient of thermal expansion for the cladding was used, $5.9 \times 10^{-6} \frac{m}{m \cdot ^\circ C}$, which is valid from $0^\circ C$ to $300^\circ C$ [78]. Thus, the stress induced by differences in expansion between the core and cladding was neglected. Similarly, the core change in refractive index due to temperature was approximated as that of the cladding. Parameter changes for a $1^\circ C$ change in temperature are given in Table 3.3.

3.4 Summary

Both the rib waveguide and polarization-maintaining fiber were discussed in this chapter. Reasons for choosing the material for each rib layer and its respective dimensions were given. The elliptical-core fiber was selected due to its geometry closely matching the rib and its polarization-maintaining properties. The index and dimensional variations of both components with respect to temperature were discussed. Results of these calculations will be presented in Chapter V. The methods used to independently calculate the electric field profile and propagation constants of both coupling components will be explored in the next chapter.

Table 3.1: Temperature Dependence of Silicon and Silicon Dioxide

MATERIAL	$\frac{dn}{dT}$ [73]	$\epsilon_{thermal}$ [65]	p_{11} [72]	p_{12} [72]	ν [72]
Silicon	1.5×10^{-4}	2.33	NA	NA	NA
SiO ₂	1.28×10^{-5}	0.55	0.121	0.27	0.17

Table 3.2: Parameter Change Calculation

PARAMETER	Expression For Temperature Dependence	Change $\left(\frac{1}{^\circ C}\right)$
W	$\epsilon_{x,total}$	$6.291 \times 10^{-6} \mu m$
$t_{overlayer}$	$\epsilon_{y,total}$	$-9.116 \times 10^{-8} \mu m$
$t_{unetched}$	$\epsilon_{y,total}$	$-9.241 \times 10^{-8} \mu m$
t_{etched}	$\epsilon_{y,total}$	$-7.632 \times 10^{-8} \mu m$
$n_{overlayer}$	$-\left(n_{overlayer}^3/2\right) \{\epsilon_{x,pe}p_{11} + [\epsilon_{z,pe} + \epsilon_{y,pe}]p_{12}\} + \frac{dn}{dT}$	1.2035×10^{-5}
n_{rib}	$-\left(n_{rib}^3/2\right) \{\epsilon_{x,pe}p_{11} + [\epsilon_{z,pe} + \epsilon_{y,pe}]p_{12}\} + \frac{dn}{dT}$	1.1865×10^{-5}
$n_{isolation}$	$-\left(n_{isolation}^3/2\right) \{\epsilon_{x,pe}p_{11} + [\epsilon_{z,pe} + \epsilon_{y,pe}]p_{12}\} + \frac{dn}{dT}$	1.2035×10^{-5}

Table 3.3: Parameter Change Calculation for Fiber

PARAMETER	Temperature Dependence	Calculated change $\left(\frac{1}{^\circ C}\right)$
a	$\epsilon_{x,fiber}$	$7.67 \times 10^{-6} \mu m$
b	$\epsilon_{y,fiber}$	$3.84 \times 10^{-7} \mu m$
n_{core}	$\frac{dn}{dT}$	1.28×10^{-5}
$n_{cladding}$	$\frac{dn}{dT}$	1.28×10^{-5}

CHAPTER IV

METHODS USED TO DETERMINE THE ELECTRIC FIELD PROFILES

4.1 Introduction

As fiber optic and integrated-optic device technology areas have developed, so has the need for understanding the modal characteristics of these structures. This need arises from the desire to accurately predict the performance of a device prior to fabrication. In particular, rib, channel, and strip-loaded waveguide devices have received more attention due to improvements in fabrication, particularly micromachining. These structures have been developed for practical uses as sensors, couplers, and electro-optic devices.

4.1.1 Three-Layer Planar Waveguide - Analytical Solution

To provide a basis for understanding a rib waveguide, a discussion of the three-layer planar guide solution will be given following the development of Marcuse [10]. Each dielectric layer is characterized by its index of refraction, n . The index of refraction is a dimensionless quantity relating the speed of light, c , to the phase velocity, v , of the electromagnetic fields within the dielectric material. That is,

$$n = \frac{c}{v} = \sqrt{\mu_r \epsilon_r}, \quad (4.13)$$

where $\epsilon = \epsilon_o \epsilon_r$ and $\mu = \mu_o \mu_r$ are the permittivity and permeability of the medium with ϵ_o and μ_o denoting the free-space values. The three-layer planar waveguide

is shown in Figure 4.8 where n_1 is the core index of refraction and n_2 and n_3 are the cladding indices. The x , y , and z coordinates illustrated in the figure are used consistently throughout this dissertation.

To confine the electromagnetic field within the guiding layer requires that $n_1 > n_2$ and $n_1 > n_3$. Generally, the overlayer has a smaller index than the lower cladding such that the confining condition can be written as $n_1 > n_2 \geq n_3$. A planar waveguide confines the field only in the y direction while the field in the x direction extends to infinity. The field propagates in the z direction via total-internal-reflection at each of the dielectric interfaces, n_1/n_2 and n_1/n_3 interfaces.

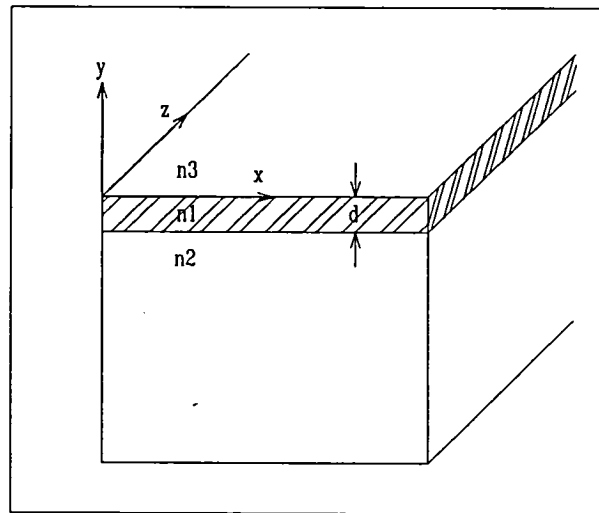


Figure 4.8: Three-layer planar waveguide.

The derivation begins with Maxwell's equations for linear, homogeneous, and isotropic nonmagnetic media,

$$\nabla \times \mathbf{H} = \epsilon_o n^2 \frac{\partial \mathbf{E}}{\partial t}, \quad (4.14)$$

$$\nabla \times \mathbf{E} = -\mu_o \frac{\partial \mathbf{H}}{\partial t}, \quad (4.15)$$

where \mathbf{H} and \mathbf{E} are the time-dependent magnetic and electric field vectors. The analysis is simplified by assuming no field variation in the x direction, denoted $\partial/\partial x = 0$. For brevity, only the transverse electric (TE) development for guided mode solutions will be given here. The TM development is analogous to the TE, hence only the TM results will be given.

4.1.2 TE Mode Development – Guided Modes

TE modes have only three field components, E_x , H_y , and H_z . When $E_y = E_z = H_x = 0$, equations (4.14) and (4.15) become

$$\frac{\partial H_y}{\partial z} - \frac{\partial H_z}{\partial y} = \epsilon_o n^2 \frac{\partial E_x}{\partial t}, \quad (4.16)$$

$$\frac{\partial E_x}{\partial z} = -\mu_o \frac{\partial H_y}{\partial t}, \quad (4.17)$$

$$\frac{\partial E_x}{\partial y} = -\mu_o \frac{\partial H_z}{\partial t}. \quad (4.18)$$

The time and z dependence of \mathbf{E} and \mathbf{H} are given by $e^{i(\omega t - \beta z)}$, which describes a wave traveling in the positive z direction with phase velocity $\nu = \omega/\beta$, where $\omega = 2\pi f$ is the radian frequency of the wave and β is the propagation constant. When $e^{i(\omega t - \beta z)}$ is inserted into equations (4.16) - (4.18), they become

$$-i\beta H_y - \frac{\partial H_z}{\partial y} = i\omega \epsilon_o n^2 E_x, \quad (4.19)$$

$$i\beta E_x = -i\omega\mu_o H_y, \quad (4.20)$$

$$\frac{\partial E_x}{\partial y} = -i\omega\mu_o H_z. \quad (4.21)$$

Rewriting equations (4.19) - (4.21) in terms of E_x yields

$$E_x = -\frac{\beta}{\omega\epsilon_o n^2} H_y + \frac{i}{\omega\epsilon_o n^2} \frac{\partial H_z}{\partial y}, \quad (4.22)$$

$$H_y = -\frac{\beta}{\omega\mu_o} E_x, \quad (4.23)$$

$$H_z = \frac{i}{\omega\mu_o} \frac{\partial E_x}{\partial y}. \quad (4.24)$$

Substituting equations (4.23) and (4.24) into equation (4.22) and multiplying by $i\omega\mu_o$ produces

$$-\beta^2 E_x + \frac{\partial^2 E_x}{\partial y^2} = -\omega^2 \epsilon_o \mu_o n^2 E_x, \quad (4.25)$$

which upon rearrangement is the one-dimensional wave equation,

$$\frac{\partial^2 E_x}{\partial y^2} + (n^2 k_o^2 - \beta^2) E_x = 0, \quad (4.26)$$

where $k_o^2 = \omega^2 \epsilon_o \mu_o = (2\pi/\lambda_o)^2$, λ_o is the wavelength of light in free space, and n is defined as

$$n = n_3 \quad \text{for } (y > 0), \quad (4.27)$$

$$n = n_1 \quad \text{for } (0 > y > -d), \quad (4.28)$$

$$n = n_2 \quad \text{for } (y < -d). \quad (4.29)$$

Solutions to equation (4.26) must satisfy the boundary conditions at the dielectric interfaces, $y = 0$ and $y = -d$. The tangential \mathbf{E} and \mathbf{H} fields must be continuous at the dielectric discontinuities. That is, E_x and H_z are continuous at $y = 0$ and

$y = -d$ and the solutions for E_x must approach zero as y approaches $\pm \infty$. Thus, solutions to E_x with implicit time and z dependence, $e^{i(\omega t - \beta z)}$, are of the form

$$E_x(y) = Ae^{-\delta y} \quad \text{for } y \geq 0, \quad (4.30)$$

$$E_x(y) = [A\cos(\kappa y) + B\sin(\kappa y)] \quad \text{for } 0 \geq y \geq -d, \quad (4.31)$$

$$E_x(y) = [A\cos(\kappa d) - B\sin(\kappa d)]e^{\gamma(y+d)} \quad \text{for } y \leq -d. \quad (4.32)$$

These are the solutions of Maxwell's equations producing the electric field of an antisymmetric three-layer planar waveguide in the three dielectric regions. If n_3 does not equal n_2 , the guide is antisymmetric; conversely, if n_3 equals n_2 , the planar guide is symmetric. The parameters δ , κ , and γ are given by

$$\delta = \sqrt{\beta^2 - n_3^2 k_o^2}, \quad (4.33)$$

$$\kappa = \sqrt{n_1^2 k_o^2 - \beta^2}, \quad (4.34)$$

$$\gamma = \sqrt{\beta^2 - n_2^2 k_o^2}. \quad (4.35)$$

To solve equation (4.26), the boundary condition for H_z must be enforced; hence H_z must be determined in the three dielectric regions. The results for H_z in regions n_3 , n_1 , and n_2 , with implicit time and z dependence, $e^{i(\omega t - \beta z)}$, are as follows;

$$H_z(y) = \frac{-i\delta}{\omega\mu_o} Ae^{-\delta y}, \quad (4.36)$$

$$H_z(y) = \frac{-ik}{\omega\mu_o} [A\sin(\kappa y) - B\cos(\kappa y)], \quad (4.37)$$

$$H_z(y) = \frac{i\sigma}{\omega\mu_o} [A\cos(\kappa d) - B\sin(\kappa d)]e^{\gamma(y+d)}. \quad (4.38)$$

4.1.3 TE Results for a Planar Waveguide - Guided Modes

Imposing the continuity requirement of H_z at the two interfaces produces two equations

$$\delta A + \kappa B = 0, \quad (4.39)$$

$$[\kappa \sin(\kappa d) - \cos(\kappa d)]A + [\kappa \cos(\kappa d) + \sin(\kappa d)]B = 0. \quad (4.40)$$

Solving this system of equations yields the eigenvalue equation for a three-layer planar waveguide,

$$\tan(\kappa d) = \frac{\kappa(\gamma + \delta)}{\kappa^2 - \gamma\delta}, \quad (4.41)$$

where δ , γ , and κ are functions of the propagation constant β , as given in equations (4.33) - (4.35).

Solutions to this transcendental equation, equation (4.41), can be exactly determined. The number of solutions obtained yields the number of guided modes which can be excited in the guide. For a single-mode three-layer planar guide, there is only one solution, denoted the fundamental mode. For many applications it is desirable for the device to operate as single mode because higher order modes have larger attenuations.

For the symmetric slab waveguide case, $n_3 = n_2$ and $\gamma = \delta$, and equation (4.41) becomes

$$\tan\left(\frac{2\kappa d}{2}\right) = \frac{2 \tan\left(\frac{\kappa d}{2}\right)}{\left[1 - \tan^2\left(\frac{\kappa d}{2}\right)\right]} = \frac{2\left(\frac{\gamma}{\kappa}\right)}{\left[1 - \left(\frac{\gamma}{\kappa}\right)^2\right]}. \quad (4.42)$$

Equation (4.42) is second-order in $\tan(\kappa d/2)$, yielding two solutions,

$$\tan(\kappa d/2) = \gamma/\kappa, \quad (4.43)$$

and

$$\tan(\kappa d/2) = -\kappa/\gamma. \quad (4.44)$$

Equations (4.43) and (4.44) correspond to the even and odd modes of a planar waveguide, respectively. The fundamental mode is denoted mode zero, the next higher mode is one (odd), followed by two (even), etc. Generally, the thicker the guide region, the more modes it will support. These equations yield exact solutions for β and the effective index of the guide is then calculated using

$$n_e = \beta/k_o. \quad (4.45)$$

4.1.4 TM Results - Guided Modes

For the transverse magnetic (TM) incident case, the field has H_x , E_y , and E_z components. Using the same procedure as in section 4.1.1, the eigenvalue equation for the asymmetric planar guide is given by

$$\tan(\kappa d) = \frac{n_1^2 \kappa (n_3^2 \gamma + n_2^2 \delta)}{(n_2 n_3 \kappa)^2 - n_1^4 \gamma \delta}. \quad (4.46)$$

For the symmetric slab case, $n_2 = n_3$, the eigenvalue equation can be determined for the even and odd modes. Even modes are given by

$$\tan(\kappa d/2) = \left(\frac{n_1^2}{n_2^2} \right) \frac{\gamma}{\kappa}, \quad (4.47)$$

and odd modes by

$$\tan(\kappa d/2) = - \left(\frac{n_2^2}{n_1^2} \right) \frac{\kappa}{\gamma}. \quad (4.48)$$

Boundary conditions require H_x and E_z to be continuous at $y = 0$ and $y = -d$ and H_x to vanish as y approaches $\pm \infty$. The electric field profile can then be determined from the H_x solution.

4.1.5 Radiation Modes

Radiation modes are solutions to Maxwell's equations that also satisfy the boundary conditions. The radiation field is considered a mode not confined to the core but rather one that extends to infinity in the y direction. For this type of mode, the propagation constants are not restricted to a discrete set of values, because they are related to the plane wave angle of incidence. These propagation constants form a continuum, hence the radiation modes do so as well.

The radiation modes can be further divided into substrate radiation modes, air radiation modes, and evanescent modes. All of the modes can be categorized by the value of the propagation constant. For guided modes, the propagation constant is in range $kn_1 < \beta < kn_2$. For substrate radiation modes, it is confined to $kn_2 < \beta < kn_3$, for air radiation modes it is confined to $0 < \beta < kn_3$, and evanescent modes are denoted by imaginary β values [81]. Because this research was concerned with the guided field profile, radiation modes were discussed for completeness but were irrelevant to the coupling efficiency calculation [10].

4.1.6 Rib Waveguide

For this study, a rib waveguide structure was investigated. A rib waveguide, illustrated in Figure 4.9, is a planar-slab waveguide with a raised height section of given width [29], which provides lateral confinement. Thus, this structure confines

the light both vertically and horizontally, analogous to a channel guide, illustrated in Figure 4.10. That channel can be readily analyzed due to its simple geometry; however, rough sidewall edges are inevitable when fabricating such a device. These rough edges greatly increase the guide's propagation loss, making it undesirable for aircraft applications since the higher the propagation loss [80], the more input light power is required for interrogation. Hence, the rectangular channel guide works well in theory, but cannot be fabricated with a low enough propagation loss for practical use.

Experimental results using various channel geometries such as channel, strip-loaded, rib, and buried rib, indicate that the buried rib waveguide produces the lowest propagation loss, which is desirable for a sensing device [63],[82]. A buried rib is a rib guide with an overlayer as illustrated in Figure 4.11. Propagation loss can be caused from leakage into the substrate, scattering at each guide/cladding interface and/or scattering due to imperfections in the film. Using the buried design decreases the field amplitude at the surface, thereby reducing scattering effects due to surface contamination, scratches, and dust.

Unlike the planar guide, there is no exact solution to the two-dimensional Maxwell wave equation, due to the complex geometry of the rib channel waveguide. Therefore, approximation and numerical methods must be utilized. Several review papers have been written describing these methods [19],[20]. A discussion of the three chosen methods will follow in the next section.

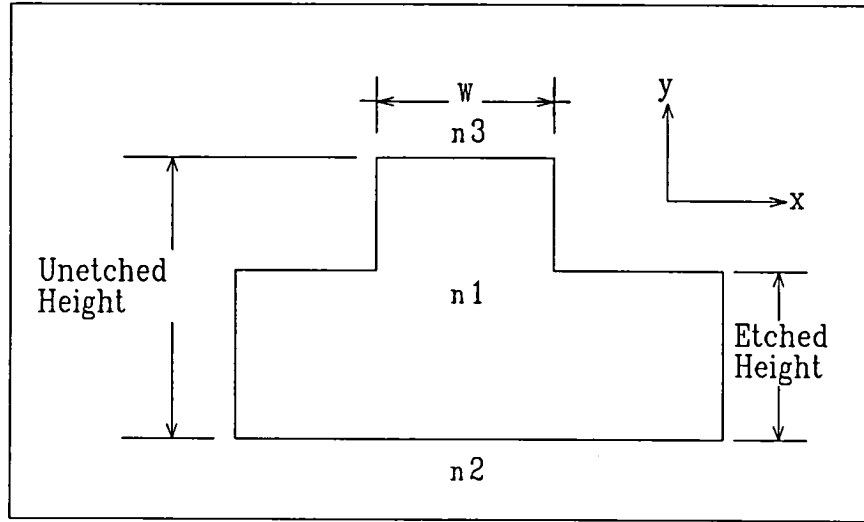


Figure 4.9: Rib waveguide.

4.1.7 Elliptical-Core Fiber

The propagation constant of an elliptical-core fiber can be solved analytically using a series of Mathieu functions [2]. As such, the field components inside and outside the core must be represented by an infinite product of terms of Mathieu and modified Mathieu functions and the propagation constant determined from the roots of an infinite determinant [2]. A numerical technique such as the method of successive approximations must be utilized to determine these roots. This numerical procedure is complex and time-consuming and the results are not conducive to the coupling efficiency calculation in this case. Thus, the same approximation and numerical techniques chosen to solve the propagation and field profile of the rib guide have also been used for the elliptical fiber.

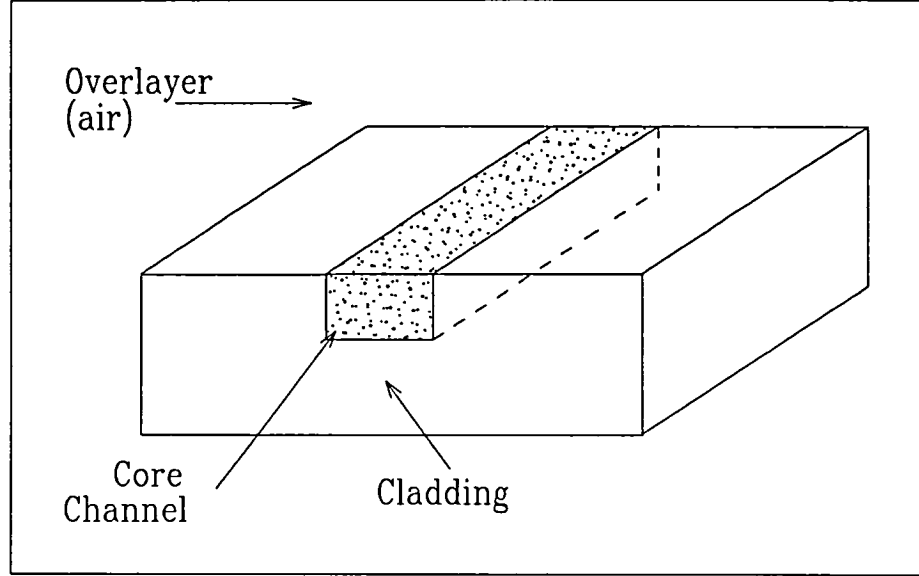


Figure 4.10: Channel waveguide structure.

4.2 Methods

For the rib channel guide and optical fiber, three methods of calculating the propagation constant and electric field profiles were utilized: the effective-index method (EIM), Marcatali's technique, and the Fourier method. All solve the scalar-wave equation. For completeness, a development of the wave equation, based on that of Marcuse [16], is given. Beginning with Maxwell's equations,

$$\nabla \times \mathbf{H} = i\omega\epsilon_0 n^2 \mathbf{E}, \quad (4.49)$$

$$\nabla \times \mathbf{E} = -i\omega\mu_0 \mathbf{H}, \quad (4.50)$$

the curl is taken of equation (4.50) and the result of equation (4.49) substituted on the right hand side, producing

$$\nabla \times (\nabla \times \mathbf{E}) = n^2 k_o^2 \mathbf{E}. \quad (4.51)$$

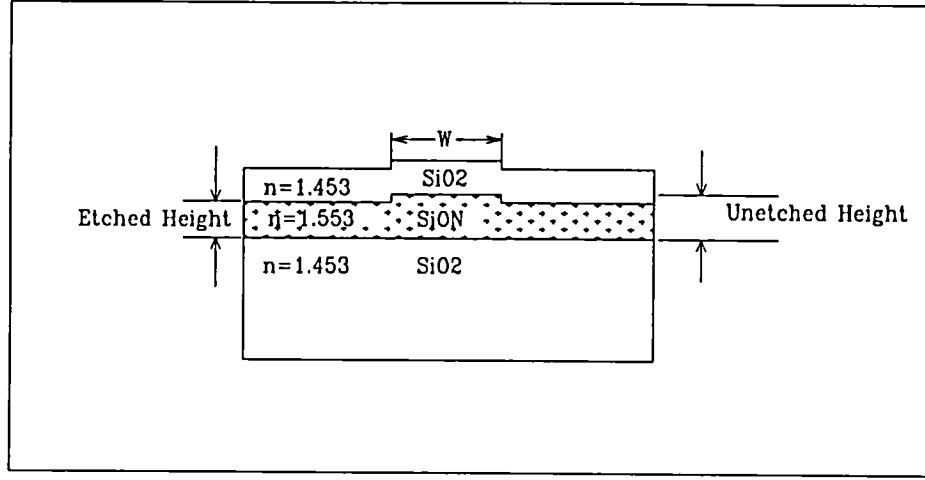


Figure 4.11: Buried rib waveguide structure.

Using the relations

$$\nabla \times (\nabla \times \mathbf{E}) = \nabla (\nabla \cdot \mathbf{E}) - \nabla^2 \mathbf{E} \quad (4.52)$$

and

$$\nabla \cdot (n^2 \mathbf{E}) = \mathbf{E} \cdot \nabla n^2 + n^2 \nabla \cdot \mathbf{E} = 0, \quad (4.53)$$

one can obtain the vector wave equation for the electric field, which is

$$\nabla^2 \mathbf{E} + \nabla \left(\mathbf{E} \cdot \frac{\nabla n^2}{n^2} \right) + n^2 k_o^2 \mathbf{E} = 0. \quad (4.54)$$

The guided mode solutions have a z dependence of $e^{-i\beta z}$; thus the Laplace operator is of the form

$$\nabla^2 = \frac{\partial^2}{\partial x^2} + \frac{\partial^2}{\partial y^2} - \beta^2. \quad (4.55)$$

The wave equation, equation (4.54), can be decomposed into x , y , and z components.

Using the previously mentioned property that the field components can be expressed in terms of E_x and E_y , only two of the three equations are needed. Using this and

the assumption that

$$\frac{\partial n}{\partial z} = 0, \quad (4.56)$$

produces the coupled equations for the x and y components of the vector wave equation, which are

$$\frac{\partial^2 E_x}{\partial x^2} + \frac{\partial^2 E_x}{\partial y^2} + [n^2(x, y)k_o^2 - \beta^2] E_x + 2 \frac{\partial}{\partial x} \left[E_x \frac{\partial \ln(n)}{\partial x} + E_y \frac{\partial \ln(n)}{\partial y} \right] = 0, \quad (4.57)$$

and

$$\frac{\partial^2 E_y}{\partial x^2} + \frac{\partial^2 E_y}{\partial y^2} + [n^2(x, y)k_o^2 - \beta^2] E_y + 2 \frac{\partial}{\partial y} \left[E_x \frac{\partial \ln(n)}{\partial x} + E_y \frac{\partial \ln(n)}{\partial y} \right] = 0. \quad (4.58)$$

If the index difference between the core and cladding of the guide is small, such that

$$\Delta = \frac{n_1 - n_2}{n_1} \ll 1, \quad (4.59)$$

where n_1 is the core and n_2 is the cladding index, then the component is considered to be weakly guiding [40]. For the rib waveguide $\Delta = 0.064$ and for the fiber $\Delta = 0.023$, which are both much less than unity, satisfying the weakly guiding condition. Thus, the last bracketed term in both equations (4.57) and (4.58) can be neglected. This yields the scalar-wave equation for E_x and E_y ,

$$\frac{\partial^2 E_x(x, y)}{\partial x^2} + \frac{\partial^2 E_x(x, y)}{\partial y^2} + [n^2(x, y)k_o^2 - \beta^2] E_x(x, y) = 0, \quad (4.60)$$

and

$$\frac{\partial^2 E_y(x, y)}{\partial x^2} + \frac{\partial^2 E_y(x, y)}{\partial y^2} + [n^2(x, y)k_o^2 - \beta^2] E_y(x, y) = 0. \quad (4.61)$$

The solution to these two scalar wave equations are identical. For quasi-TE modes propagating in the z direction, the electric field is of the form

$$\mathbf{E}(x, y, z) = \hat{x} E_x(x, y) e^{i(\omega t - \beta z)}, \quad (4.62)$$

where $E_x(x, y)$ is the field profile. The electric field of a TE mode has x and y components, however, the quasi-TE mode electric field has only an x component. All three of the chosen techniques, the EIM, Marcatili, and the Fourier method, produce solutions to the two-dimensional scalar wave equation (4.60), where $n(x, y)$ is the spatially dependent function for the index of refraction and k_o was previously defined.

4.2.1 Effective-Index Method (EIM)

Rib Waveguide

The EIM reduces the two-dimensional scalar wave equation, equation (4.60), into two one-dimensional problems. This is achieved by first dividing the rib guide into three separate planar guides oriented perpendicular to the y axis, as shown in Figure 4.12. Slabs A and C, which have identical characteristics, correspond to the etched portion of the waveguide, while Slab B corresponds to the unetched portion. The effective index of each slab was determined using the procedure for the three-layer planar guide discussed in section 4.1.1 assuming TE incident light. N_I is the effective index of Slab B and N_{II} is the effective index of Slabs A and C, where $N_{I,II} = \beta_{I,II}/k_o$. To determine the degree of confinement in the x direction, a symmetric slab waveguide, Slab D, is constructed perpendicular to the x axis. Due to the orientation of the guide, the effective index of Slab D is determined for the TM case. Slab D uses N_I and N_{II} as the core and cladding indices, respectively, and the rib width W as the core thickness. The analytic solution of Slab D yields the effective index, n_e , of the rib guide.

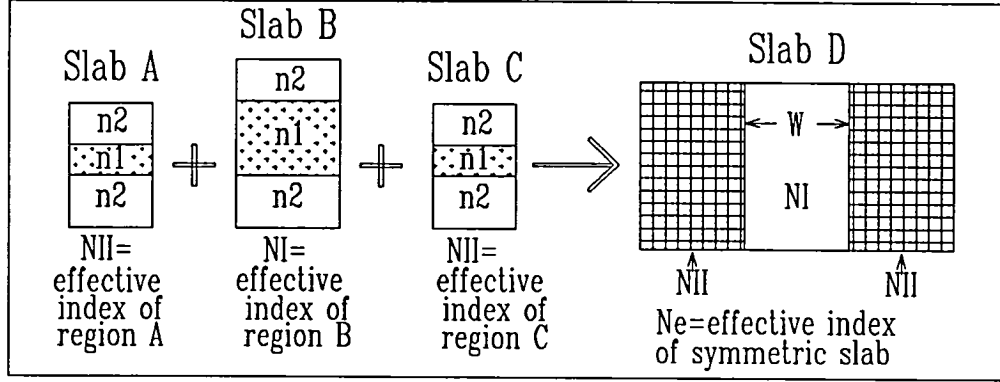


Figure 4.12: EIM constituent slab waveguides.

While not applicable to this particular rib, it should be noted that when analyzing the slabs, it is possible for Slab B to be single mode while Slabs A and C are cutoff. If either Slab A or C is cutoff, there is no guided-mode solution for these planar regions. An approach to circumvent this situation is to assume an effective index of unity in these regions [83].

Quantitatively, for the TE mode, the transverse field is given by

$$\mathbf{E}_x = E_{xx}\hat{x} + E_{xy}\hat{y}, \quad (4.63)$$

where E_{xx} and E_{xy} are the x and y components of the field profile. Substituting equation (4.63) into the vector wave equation, (4.54), produces a pair of coupled equations,

$$\nabla^2 E_{xx} + (n^2 k_o^2 - \beta_x^2) E_{xx} = -\frac{\partial}{\partial x} \left[\frac{E_{xx}}{n^2} \frac{\partial(n^2)}{\partial x} \right] - \frac{\partial}{\partial x} \left[\frac{E_{xy}}{n^2} \frac{\partial(n^2)}{\partial y} \right] \quad (4.64)$$

$$\nabla^2 E_{xy} + (n^2 k_o^2 - \beta_x^2) E_{xy} = -\frac{\partial}{\partial y} \left[\frac{E_{xx}}{n^2} \frac{\partial(n^2)}{\partial x} \right] - \frac{\partial}{\partial y} \left[\frac{E_{xy}}{n^2} \frac{\partial(n^2)}{\partial y} \right]. \quad (4.65)$$

For $E_{xx} \gg E_{xy}$, by an order of Δ given in equation (4.59), the right hand side of these coupled vector equations is near-zero for small index discontinuities. These coupled vector equations can then be approximated by the scalar wave equation, equation (4.60).

For a rectangular waveguide, the EIM can first be applied to either the rectangle oriented perpendicular to the x axis (short guide height), or the rectangle oriented perpendicular to the y axis (large guide height). Kumar et. al. [84] have compared the results for the same guide calculated both ways. They determined that the EIM produces more accurate results if applied to the shorter dimension first.

The EIM uses the method of separation of variables to solve the scalar-wave equation, where the index profile is approximated as

$$n^2(x, y) = n'^2(x) + n''^2(y). \quad (4.66)$$

As discussed for the rib, the field profile, E_x , is defined in equation (4.77). Using equation (4.66), the two-dimensional scalar wave equation can then be written in the form

$$\frac{1}{X(x)} \frac{d^2 X(x)}{dx^2} + \frac{1}{Y(y)} \frac{d^2 Y(y)}{dy^2} + \left\{ k_o^2 \left[n'^2(x) + n''^2(y) \right] - \beta^2 \right\} = 0. \quad (4.67)$$

For the planar waveguide analyzed, $n''(y)$ is denoted as

$$n''(y) = n_1 \quad \text{for } y < |b'| \quad (4.68)$$

$$n''(y) = n_2 \quad \text{for } y < -b' \quad (4.69)$$

$$n''(y) = n_3 \quad \text{for } y > b' \quad (4.70)$$

and $Y(y)$ satisfies the one-dimensional wave equation,

$$\frac{1}{Y(y)} \frac{d^2 Y(y)}{dy^2} + [k_o^2 n''^2(y) - \beta_y^2] = 0. \quad (4.71)$$

Subtracting equation (4.71) from equation (4.67) produces

$$\frac{1}{X(x)} \frac{d^2 X(x)}{dx^2} + \left\{ k_o^2 \left[n'^2(x) + \frac{\beta_y^2}{k_o^2} \right] - \beta^2 \right\} = 0, \quad (4.72)$$

where β is the propagation constant of the fundamental mode of the planar guide whose index profile is given by the bracketed term,

$$n'^2(x) + \frac{\beta_y^2}{k_o^2} = \frac{\beta_y^2}{k_o^2} \quad \text{for } |x| < a' \quad (4.73)$$

$$n'^2(x) + \frac{\beta_y^2}{k_o^2} = n_4^2 \quad \text{for } |x| > a' \quad (4.74)$$

which provides the x dependent index profile,

$$n'^2(x) = 0 \quad \text{for } |x| < a' \quad (4.75)$$

$$n'^2(x) = - \left[\frac{\beta_y^2}{k_o^2} - n_4^2 \right] \quad \text{for } |x| > a' \quad (4.76)$$

Substituting the results for $n'^2(x)$ and $n''^2(y)$ into equation (4.66) produces the separable refractive index profile, $n^2(x, y)$, the EIM uses to solve the two-dimensional scalar wave equation. This index profile is shown in Figure 4.13 and is larger than the actual index profile when $|x| > a'$ and $|y| < b'$, by $n_1^2 - \frac{\beta_y^2}{k_o^2}$ and smaller in the corner regions by $\frac{\beta_y^2}{k_o^2} - n_4^2$. Since the field magnitude is smaller in the corner regions than the cladding regions, the effective index calculated using the EIM is always larger than the actual effective index, hence, this method consistently overestimates the propagation constant of the guide [84].

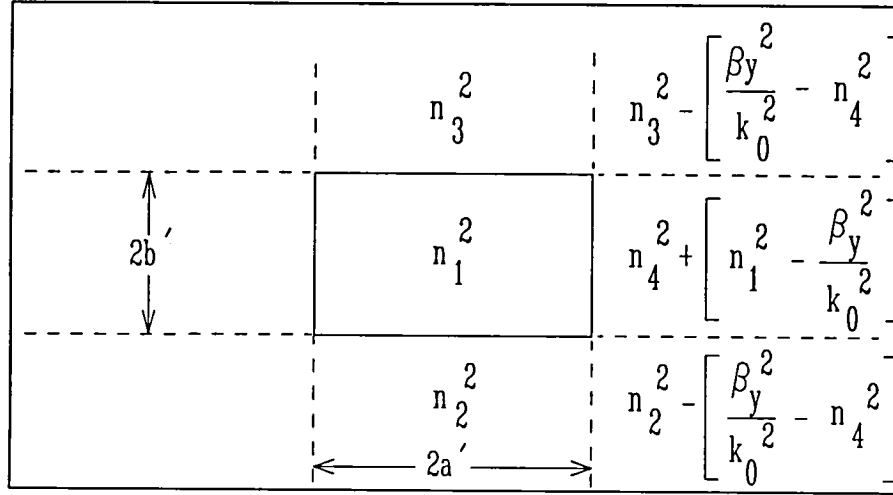


Figure 4.13: EIM separable refractive index profile shown in its respective region - shorter dimension analyzed first.

Following the same procedure, but starting with the x -slab (larger dimension) first, the EIM approximates the waveguide shown in Figure 4.14. In this case the index in regions $y < -b'$ and $y > b'$ is larger by $n_1^2 - \frac{\beta_x^2}{k_0^2}$ and lower in the corner regions by $\frac{\beta_x^2}{k_0^2} - n_4^2$. The error in the propagation constant is larger due to the overestimation of the index in the cladding regions along the shorter rectangle dimension, where the field magnitude is greater than in the outer cladding region. Thus, when analyzing a rectangular guide oriented perpendicular to the x -axis using the EIM, the results are more accurate if the y -slab is analyzed first.

The electric field profile of the rib is the product of the field distribution of Slab B, $X(x)$, and that of D, $Y(y)$, i.e.,

$$E_x(x, y) = X(x) Y(y). \quad (4.77)$$

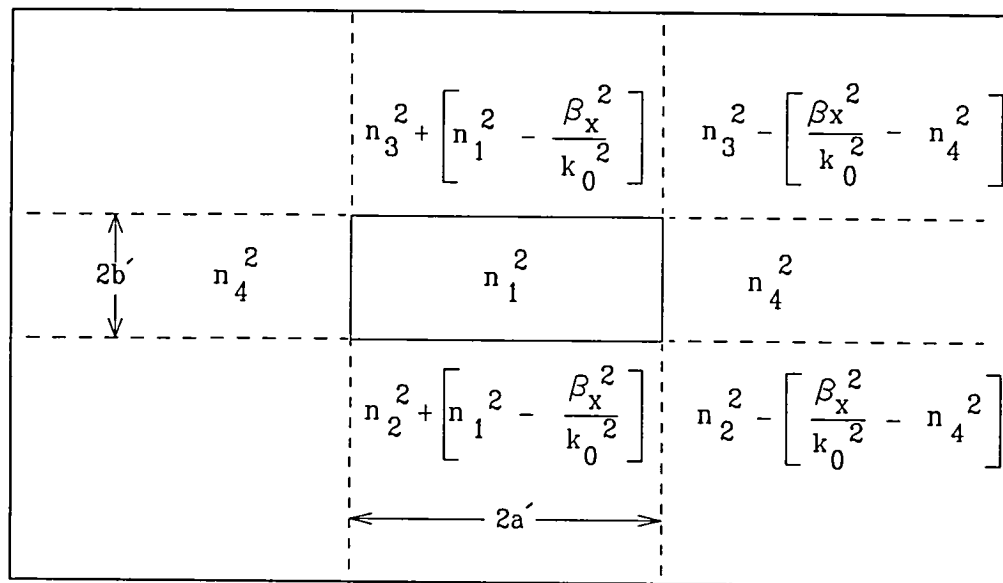


Figure 4.14: EIM separable refractive index profile shown in its respective region - longer dimension analyzed first.

The field function, $X(x)$, is determined using equations (4.30) - (4.32) and $Y(y)$ is determined from the eigenvalue equation (4.47), applying the boundary conditions for the TM case.

The EIM has intuitive appeal; however, because the guide is analyzed as three separate slabs, the field continuity conditions at the interfaces are not satisfied. Therefore, the results from this method are most accurate for ribs with small height and large width [60]. This condition was satisfied in this study as the guide etch depth was $0.09 \mu m$ which is small when compared to its $2.7 \mu m$ width. Several researchers have attempted to improve this method but none significantly change the results [22],[23],[24],[25],[26],[28],[85] and they tend to apply to specific cases.

Fiber Field - EIM

The fiber shown in Figure 4.15 is a single-mode polarization-maintaining elliptical-core fiber. Thus, the Gaussian approximation commonly used for circular-core fibers was not valid for this case [18],[40]. The electric field and propagation constant of the elliptical-core fiber were calculated using the EIM [18], where the fiber was approximated as a rectangle with dimensions a' and b' such that the rectangle and ellipse have the same area and aspect ratio. Since an ellipse has an area of πab , these dimensions are given by

$$a' = a \frac{\sqrt{\pi}}{2} \quad (4.78)$$

and

$$b' = b \frac{\sqrt{\pi}}{2}. \quad (4.79)$$

Using the procedure given in section 4.2.2, the fiber field and effective index were determined for this rectangle. Marcattili's method was designed to evaluate rectangles,

hence, for comparison purposes between the two approximation techniques, the fiber was modelled as a rectangle for the EIM.

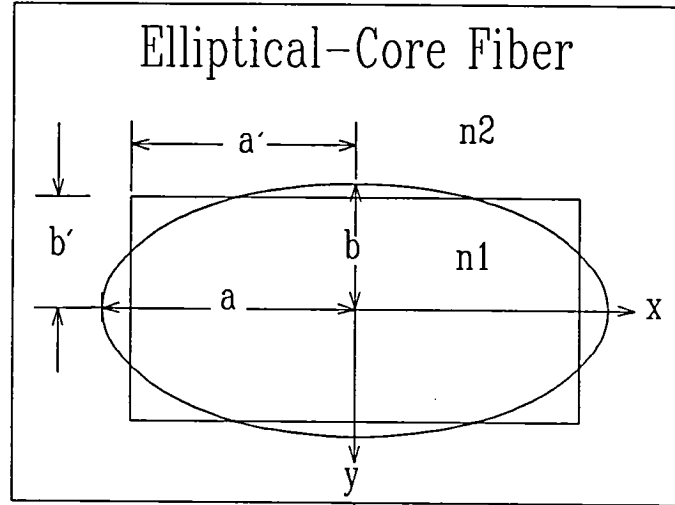


Figure 4.15: Elliptical-core fiber with pseudo-guide (rectangle).

4.2.2 Marcatili's Method

Rib Waveguide

For modes far from cutoff, the majority of the field energy is confined to the central core region. If this assumption applies, a pseudo-rectangular waveguide can be utilized to approximate the rib structure [15]. The cross section of the waveguide is divided into nine regions as shown in Figure 4.16, in which t is the etch depth and r is the thickness of the etched SiON layer, such that the unetched height is $r + t$.

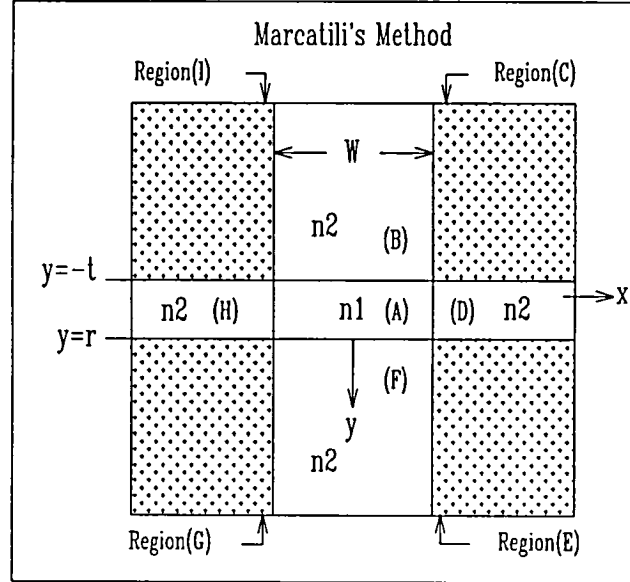


Figure 4.16: Marcatili's method: pseudo-guide used to approximate rib guide.

The pseudo-guide is assigned a refractive index profile which approximates that of the actual rib. This profile provides readier analysis because $n^2(x, y)$ is separable in the x and y coordinates, as defined by [15]

$$n^2(x, y) = n'^2(x) + n''^2(y) - n_1^2, \quad (4.80)$$

where

$$n'(x) = n_1 \quad \text{for } |x| < \frac{W}{2}, \quad (4.81)$$

$$n'(x) = n_2 \quad \text{for } |x| > \frac{W}{2}, \quad (4.82)$$

and

$$n''(y) = n_1 \quad \text{for } -t < y < r, \quad (4.83)$$

$$n''(y) = n_2 \quad \text{for } (y < -t) \text{ or } (y > r). \quad (4.84)$$

Analogous to the EIM, this method reduces the two-dimensional wave equation into two separate one-dimensional problems. Substituting equations (4.81) - (4.84) into equation (4.80) produces an index, $n(x, y)$, which is separable in x and y . Using this index distribution in equation (4.60) yields

$$\left[\frac{d^2}{dx^2} + k_o^2 n'^2(x) - \beta_1^2 \right] X(x) = 0, \quad (4.85)$$

and

$$\left[\frac{d^2}{dy^2} + k_o^2 n''^2(y) - \beta_2^2 \right] Y(y) = 0, \quad (4.86)$$

where

$$\beta_1^2 + \beta_2^2 - k_o^2 n_1^2 = \beta^2. \quad (4.87)$$

When the mode is well-guided, the majority of the field energy is in the central core (n_1 region) which is the key assumption of this theory [10]. The refractive-index profile of the rib waveguide and pseudo guide differs in the outer shaded regions and sections D and H of Figure 4.16. The index of refraction in the shaded regions is $\sqrt{2n_2^2 - n_1^2}$. In regions D and H the actual index is

$$n = n_2 \quad \text{for } (-t < y < 0) \quad (4.88)$$

$$n = n_1 \quad \text{for } (0 < y < r). \quad (4.89)$$

However, for this approximation, it is assumed that n_2 is the index throughout regions D and H. Because the modal power in these outer regions is small, the mode field profile of the pseudo-guide should closely resemble that of the rib guide. This assumption is generally applicable for ribs with large etch depths ($t \gg r$). However, for this channel guide the etch depth (t) is small, but because the rib is wide

($W \gg r + t$), it is expected that the pseudo-guide will provide an accurate field profile.

Following the development of Varshney and Kumar [15], the field is given by equation (4.77), where the x dependent solutions are

$$X(x) = A_1 \cos\left(2\mu_1 \frac{x}{W} - \theta\right) \quad \text{for } |x| < \frac{W}{2}, \quad (4.90)$$

$$X(x) = A_2 \exp\left(-2\mu_2 \frac{|x|}{W}\right) \quad \text{for } |x| > \frac{W}{2}, \quad (4.91)$$

where

$$\mu_1 = \frac{W}{2} \sqrt{k_o^2 n_1^2 - \beta_1^2}, \quad (4.92)$$

$$\mu_2 = \frac{W}{2} \sqrt{\beta_1^2 - k_o^2 n_2^2}, \quad (4.93)$$

and $\theta = 0$ $\left(\frac{\pi}{2}\right)$ for a mode symmetric (antisymmetric) in x . The y dependent solutions are given by

$$Y(y) = A_b \exp\left(\frac{-\gamma_b y}{t}\right) \quad \text{for } y > r, \quad (4.94)$$

$$Y(y) = A_c \cos\left(\frac{\gamma_c y}{t}\right) + B_c \sin\left(\frac{\gamma_c y}{t}\right) \quad \text{for } -t < y < r, \quad (4.95)$$

$$Y(y) = A_a \exp\left(\frac{\gamma_a y}{t}\right) \quad \text{for } y < -t, \quad (4.96)$$

where

$$\gamma_b = t \sqrt{\beta_2^2 - k_o^2 n_2^2}, \quad (4.97)$$

$$\gamma_c = t \sqrt{k_o^2 n_1^2 - \beta_2^2}, \quad (4.98)$$

$$\gamma_a = \gamma_b. \quad (4.99)$$

Assuming the dominant mode is quasi-TE, the boundary conditions are,

$$n^2 E_x(x, y) \text{ and } \frac{\partial E_x(x, y)}{\partial x} \text{ continuous at } x = \pm \frac{W}{2}, \quad (4.100)$$

and

$$E_x(x, y) \text{ and } \frac{\partial E_x(x, y)}{\partial y} \text{ continuous at } y = -t, r. \quad (4.101)$$

These boundary conditions are applied and an eigenvalue equation determined for the x and y dependent field functions, given by

$$\tan^{-1} \left[\frac{n_1^2 \mu_2}{n_2^2 \mu_1} \right] - \mu_1 + (p-1) \frac{\pi}{2} = 0, \quad (4.102)$$

and

$$\tan^{-1} \left[\frac{\gamma_a}{\gamma_c} \right] + \tan^{-1} \left[\frac{\gamma_b}{\gamma_c} \right] - \gamma_c \left(1 + \frac{r}{t} \right) + (q-1)\pi = 0, \quad (4.103)$$

for the x and y dependent field functions, respectively. For the fundamental mode, $p = q = 1$ in equations (4.102) and (4.103). Constants A_1 , A_2 , A_a , A_b , A_c , and B_c are determined by satisfying the boundary conditions given in equations (4.100) and (4.101) and the electric field profile is calculated using the solutions for β_1 and β_2 .

Perturbation Correction - Guide Effective Index

The error caused by approximating the rib guide with a pseudo guide can be reduced using a first-order perturbation correction to the propagation constant [14]. The first-order perturbation correction minimizes the difference between the actual guide and the pseudo guide.

The following development is from Varshney [15]. The perturbation correction to the effective index, calculated using Marcatili's method, is expressed as [15]

$$\beta'^2 = \frac{k_o^2 \int \int |E_x(x, y)|^2 \delta n^2 dx dy}{\int \int |E_x(x, y)|^2 dx dy}, \quad (4.104)$$

where the integration is over all space and δn^2 is given by

$$\delta n^2 = (n_1^2 - n_2^2) \quad \text{shaded regions (C), (E), (G), and (I),} \quad (4.105)$$

$$\delta n^2 = 0 \quad \text{otherwise.} \quad (4.106)$$

Inserting β' into the following equation produces the corrected value for β ,

$$\beta_o^2 + \beta'^2 = \beta^2, \quad (4.107)$$

where β_o is the propagation constant determined using Marcatili's method. Because $(n_1^2 - n_2^2)$ is small in this case, the correction term is small as well. Once β is determined, the effective index of the guide is calculated using equation (4.45).

Marcatili - Fiber Electric Field

Using Marcatili's technique to calculate the field profile of an elliptical-core fiber has been discussed in the literature with accurate results [14],[42],[43]. For this method, the elliptical core is approximated by a rectangle, for which an analytical solution can be found. The same rectangle dimensions chosen for the EIM are used for this method [42]. Using this rectangle as the pseudo-guide, Marcatili's method as described in section 4.2.2, is used to determine the fiber field profile. The field is

given by equations (4.82) and (4.95) - (4.104), replacing t and r with b' , W with $2a'$, and $B_c = 0$.

Perturbation Correction - Fiber Effective Index

To determine the perturbation correction to the propagation constant, equation (4.104) is used. However, for the fiber, δn^2 is of the form [42],[43]

$$\delta n^2 = (n_1^2 - n_2^2) \quad \text{for regions 1, 3, and 4,} \quad (4.108)$$

$$\delta n^2 = (n_2^2 - n_1^2) \quad \text{for region 2,} \quad (4.109)$$

$$\delta n^2 = 0 \quad \text{otherwise.} \quad (4.110)$$

where the regions are defined in Figure 4.17. Again, this calculation for the effective index is used only for comparison purposes between the methods.

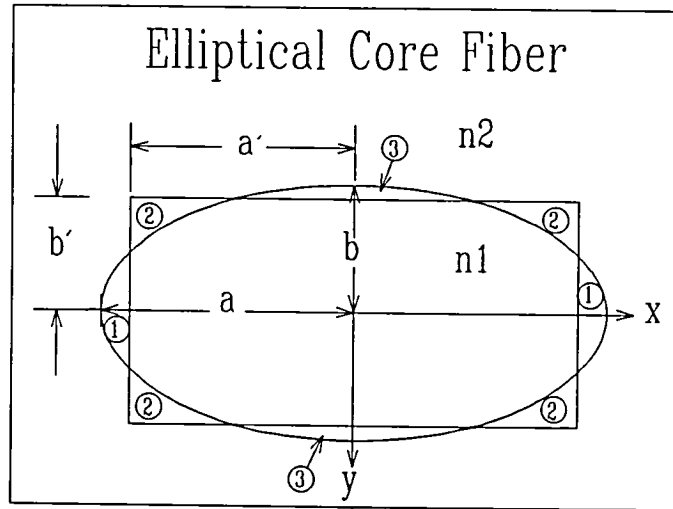


Figure 4.17: Elliptical-core fiber with regions defined for perturbation correction to the propagation constant.

4.2.3 The Fourier Method

Rib Waveguide

The scalar-wave solution applies to waveguides having small index discontinuities in the region of field confinement, which is the case being studied. If the waveguide had a large index difference between the core and cladding where the field intensity was large, a vector solution would have been necessary. Using Maxwell's equations, elimination of either the magnetic or electric field vectors as shown in Chapter III can be achieved, to obtain the wave equations for either the electric field or magnetic field. Analogous to the procedure described in section 4.1.1, the transverse components of the vector wave equations contain two components, which are either E_x and E_y or H_x and H_y . This reduces the solution of the guided mode problem to two simultaneous equations for E_x and E_y or H_x and H_y . Using the vector wave equation for \mathbf{H} , a similar wave equation can be derived similar to that for \mathbf{E} discussed here. Formulating the problem in this way results in identical eigenvalues as for the \mathbf{E} expansion; however, the E_t field results are inaccurate because the discontinuity of the \mathbf{E} field is represented by a continuous \mathbf{H} field [16].

To obtain a solution to the scalar wave equation, E_x is expressed as an infinite series in terms of a complete set of orthonormal functions,

$$E_x = \sum_{\mu=1}^{\infty} \sum_{\nu=1}^{\infty} A_{\mu\nu} \Psi_{\mu\nu}(x, y), \quad (4.111)$$

where

$$\Psi_{\mu\nu} = \frac{1}{\sqrt{L_x L_y}} \sin(\sigma_{\mu} x) \sin(\rho_{\nu} y), \quad (4.112)$$

is a simple and complete orthonormal set of sine functions, where

$$\sigma_\mu = \frac{\mu\pi}{L_x}, \quad (4.113)$$

and

$$\rho_\nu = \frac{\nu\pi}{L_y}, \quad (4.114)$$

and μ and ν are integers. The sine function, $\Psi_{\mu\nu}$, is orthogonal over the finite base domain of $(0 \leq x \leq L_x)$ and $(0 \leq y \leq L_y)$, such that

$$\int_0^{L_x} \int_0^{L_y} \Psi_{\mu\nu}(x, y) \Psi_{\mu'\nu'}(x, y) dx dy = \delta_{\mu\mu'} \delta_{\nu\nu'}, \quad (4.115)$$

where δ is the Kronecker delta function. For this method, the field is described only over this finite base domain; thus, proper choice of the domain limits is critical for this method to produce accurate results. The values for L_x and L_y are chosen such that the field on those boundaries is zero. For well-guided modes these boundaries are small and this method performs well. However, for waves at or near cutoff, the field is not well-confined and the finite domain does not apply.

For the Fourier method, equation (4.111) is inserted into the scalar wave equation, equation (4.60). Multiplying the left side by $\Psi_{\mu\nu}(x, y)$ and integrating over the finite base domain, produces a matrix equation expressed as

$$\sum_{\mu=1}^{m_x} \sum_{\nu=1}^{m_y} (M_{\mu'\nu',\mu\nu} A_{\mu\nu}) = \left(\frac{\beta^2}{k_o^2} \right) A_{\mu'\nu'}, \quad (4.116)$$

where

$$M_{\mu'\nu',\mu\nu} = \frac{4}{L_x L_y} \int_0^{L_x} \int_0^{L_y} \left[n^2(x, y) - \frac{\sigma_\mu^2 - \rho_\nu^2}{k_o^2} \right] \Psi_{\mu\nu}(x, y) \Psi_{\mu'\nu'}(x, y) dx dy, \quad (4.117)$$

which can be rewritten as

$$M_{\mu'\nu',\mu\nu} = \left[\frac{4}{L_x L_y} \int_0^{L_x} \int_0^{L_y} n^2(x, y) \Psi_{\mu\nu}(x, y) \Psi_{\mu'\nu'}(x, y) dx dy \right] - \frac{4}{L_x L_y} \frac{\sigma_\mu^2 - \rho_\nu^2}{k_o^2} \delta_{\mu\mu'} \delta_{\nu\nu'}. \quad (4.118)$$

The index of refraction profile in equation (4.118) is approximated by rectangles of constant index, to obtain a closed form solutions of the integral. Thus, the rib was broken into rectangular regions of constant refractive index for the calculations [35].

Equation (4.116) can be rewritten in terms of a matrix \overline{C} , with eigenvector \overline{X} and eigenvalue $\left(\frac{\beta^2}{k_o^2}\right)$. Increasing the number of terms, by increasing the limit values m_x and m_y , increases the accuracy of the results. For many cases, a series of 10 sine functions in both directions is sufficient to produce accurate results [16]. In this study, 30 was used for m_x and m_y values, due to the large window size. This meant that the order of the matrix was 900, hence there were 900 eigenvalues. These eigenvalues represent both the guided and unguided modes, however, only the fundamental guided mode was of interest.

Using the procedure from Marcuse [16], two FORTRAN programs [86] were developed to determine the propagation characteristics of the rib and fiber. The L_x and L_y chosen values, 15 μm and 10 μm , respectively, were large compared to the fiber and rib guide geometry. This choice was necessary to maintain the zero field condition on the domain boundary while the rib guide was shifted with respect to the fiber, in order to determine the coupling efficiency at various transverse offsets.

Fiber Field - the Fourier method

The Fourier method was applied to the elliptical-core fiber using the development just described to calculate both the field profile and the propagation constant.

The fiber dimension was closely approximated as a single rectangle with the integration performed over the elliptical-core boundary. The same L_x and L_y domain boundaries as well as expansion terms used for the rib were used for the elliptical-core fiber.

The Fourier Method - Validity

The accuracy of the Fourier method and appropriateness of choices for the evaluation boundary and number expansion terms were studied. To determine the validity of the evaluation box boundary and number of expansion terms chosen, an analysis of the Fourier method was conducted to compare the $E^2(x, y)$ values at a particular point for the rib guide.

The L_x and L_y boundary values were varied from a $7 \mu m$ by $2 \mu m$ box to a 15 by $10 \mu m$ box increasing both dimensions in $1 \mu m$ increments. Effects on $E^2(x, y)$ at $\left(\frac{L_x}{2} - 0.05, \frac{L_y}{2}\right)$ are shown in Figure 4.18. From this figure, it appears that all of the boxes produce similar E^2 values with a maximum difference between points of 5.99×10^{-4} , hence a 15 by $10 \mu m$ box is more than adequate for the structures being analyzed in this dissertation.

For the rib, the m_x and m_y values were varied from 5 to 30 in increments of 5 . Results shown in Figure 4.19 indicate that using 15 or more terms produces the same $E^2(x, y)$ value, hence the 30 expansion terms used are more than sufficient.

Another analysis was performed to determine whether the electric field discontinuity at the dielectric interfaces was evident. Field results taken at $x = 0$ and $x = \frac{W}{2}$ slices do not show the discontinuity, as illustrated in Figures 4.20 and 4.21. This is most likely an artifact of approximating the vector wave equation by the

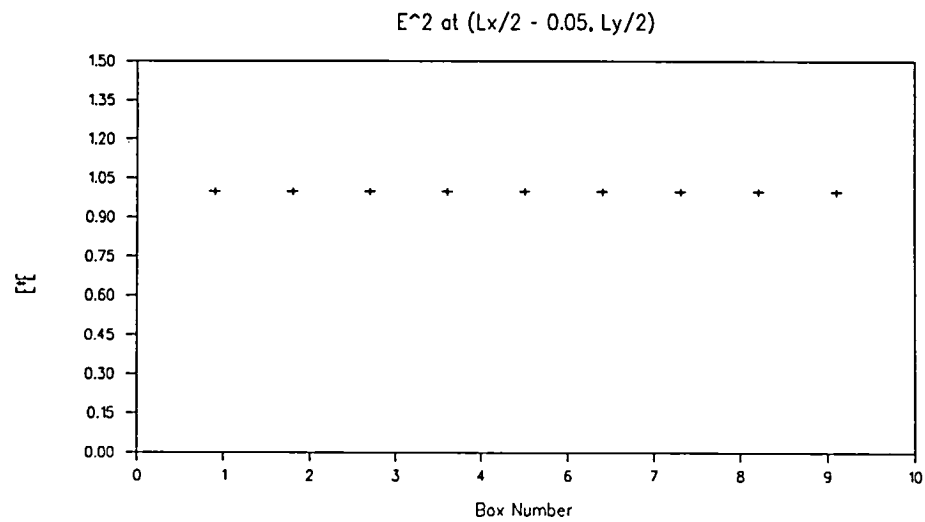


Figure 4.18: E^2 at $\left(\frac{L_x}{2} - 0.05, \frac{L_y}{2}\right)$ vs. box size

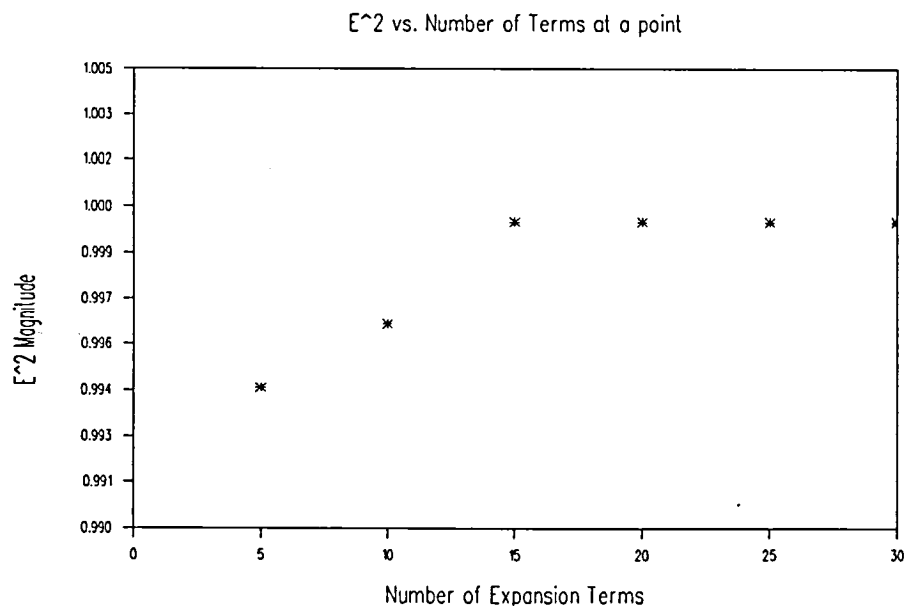


Figure 4.19: $E^2(x, y)$ vs. number of expansion terms at a point.

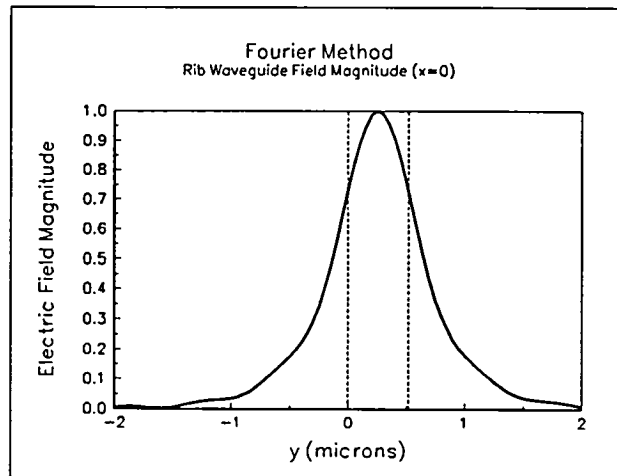


Figure 4.20: Rib waveguide field magnitude at $x = 0$ vs. y calculated using the Fourier method.

scalar-wave equation, but may also be due to the number of expansion terms used or the small dielectric discontinuity.

As a proof of the accuracy of the Fourier method, it was applied to two different rib waveguide geometries found in the literature and field results were compared. The first rib, Rib 1, consisted of a 3 layer guide [60] as illustrated in Figure 4.22. The calculated effective index was 3.437397 and 3.436799 using the EIM and Fourier methods, respectively. This rib was narrow and wide, hence the EIM is not expected to produce accurate results. Using the EIM and finite difference method, field profiles for the rib were given in the literature. The vast difference between the profile calculated using the EIM and finite difference illustrate how approximation techniques must be used with caution, because the EIM is not applicable to all rib guides. Contour plots of the literature results are shown in Figures 4.23 and 4.24.

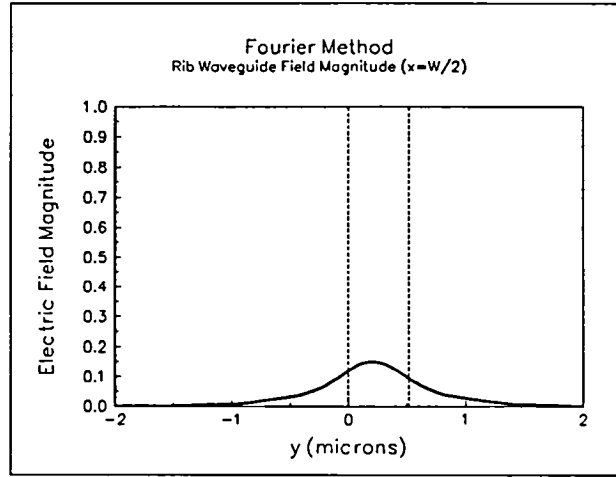


Figure 4.21: Rib waveguide field magnitude at $x = \frac{W}{2}$ vs. y calculated using Fourier method.

Field results using the Fourier method, illustrated in Figure 4.25 closely resemble the finite element.

Rib 2 differs slightly from a standard rib in that the index of the regions external to the rib are not of uniform index as illustrated in Fig. 4.26. The operating wavelength was $1.335 \mu m$ and the rib width was $8 \mu m$. The Fourier method predicted an effected index of 1.57058 which compares well to 1.57081 calculated using the domain integral equation analysis. Field intensity plots appear similar as shown in Figures 4.27 and 4.28.

The propagation characteristics of a circular-core fiber was determined using the three solution techniques and results were compared to the exact solution given in the literature. The fiber and the rectangles used to approximate it for the Fourier method are shown in Figure 4.29. Effective index results are given in Table 4.4 and field results in Figure 4.30. The exact solution field result is shown in Figure 4.31.

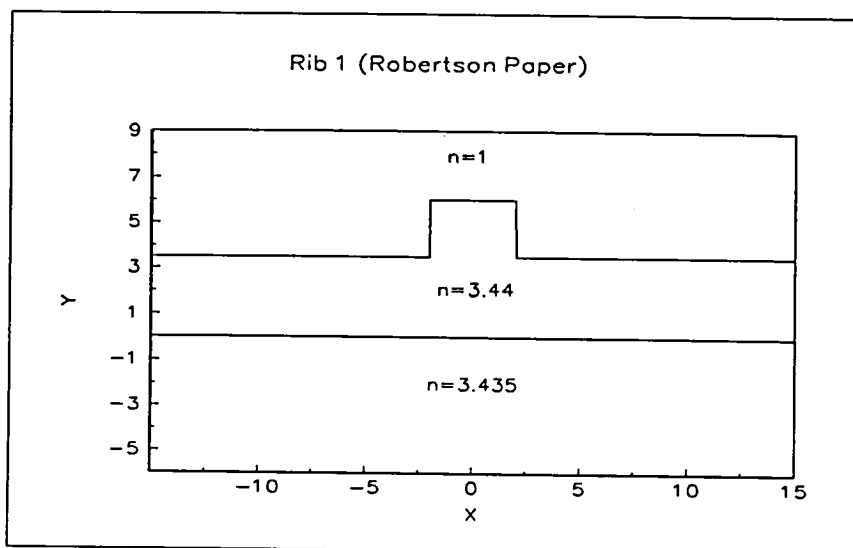


Figure 4.22: Geometry of Rib 1 from Robertson paper.

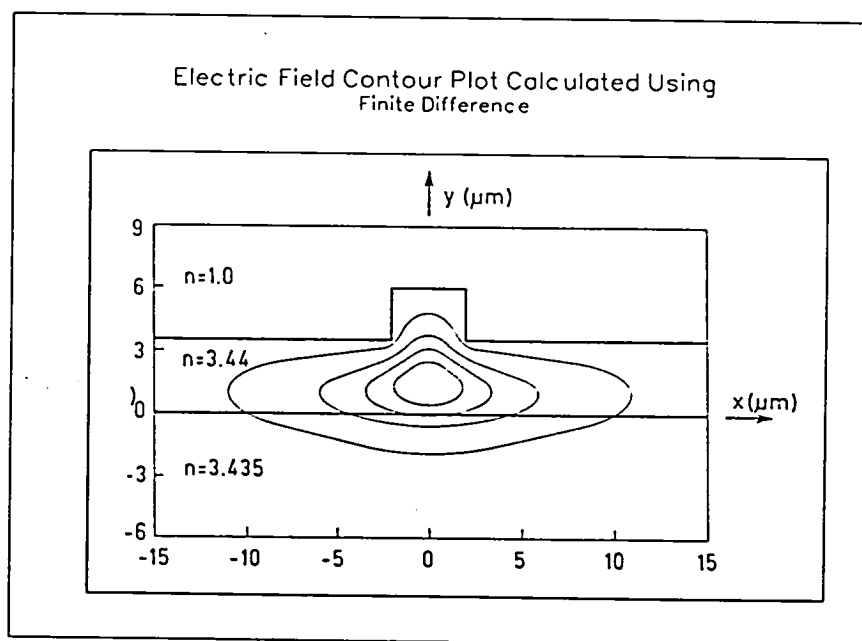


Figure 4.23: Electric field contour plot calculated using finite difference method.

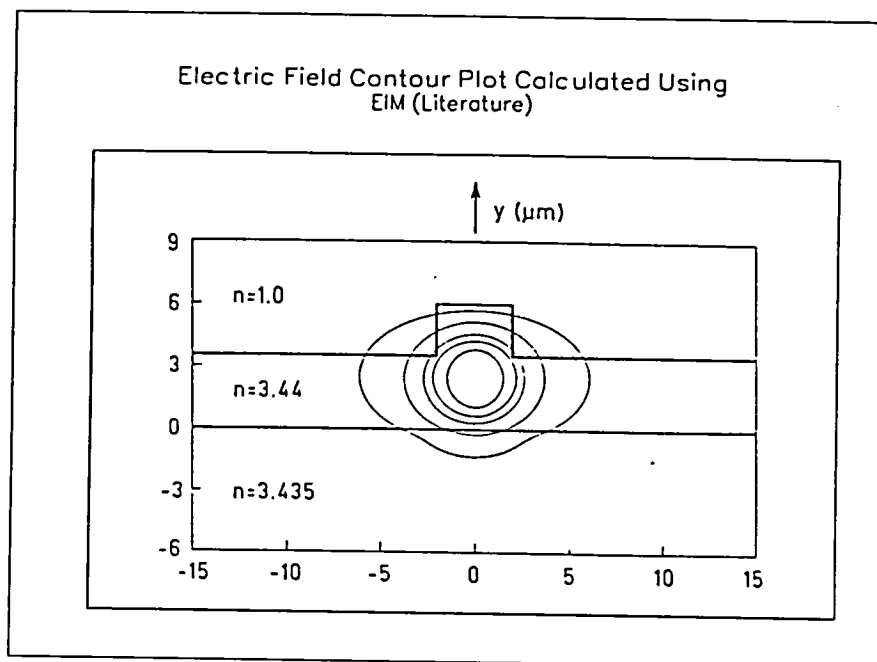


Figure 4.24: Electric field contour plot calculated using the EIM.

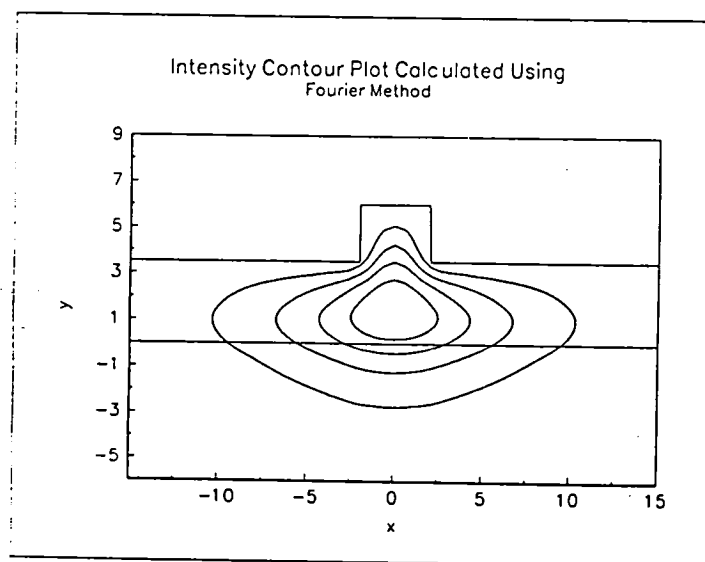


Figure 4.25: Electric field contour plot calculated using the Fourier method.

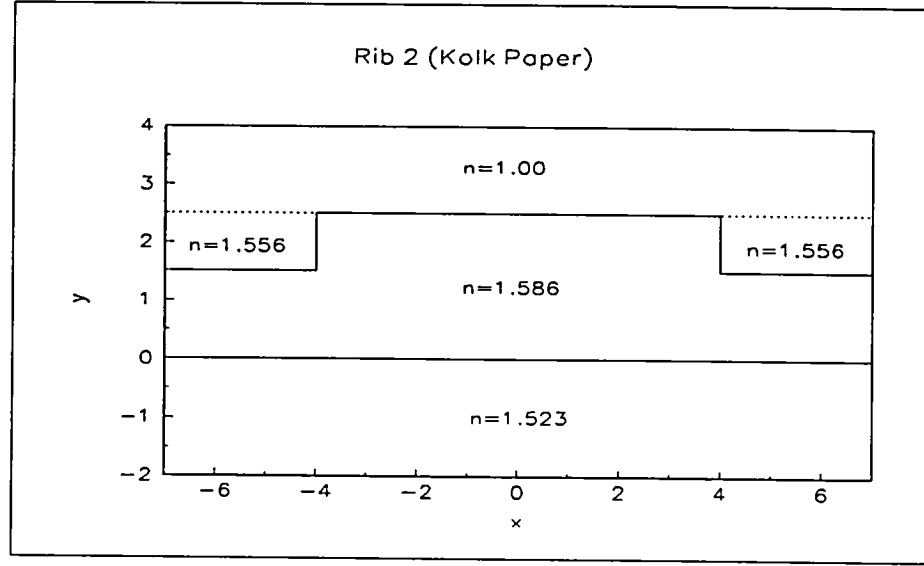


Figure 4.26: Geometry of rib 2 from Kolk paper.

Comparing Figures 4.30 and 4.31, it was evident that the Fourier field result was nearly identical to the exact solution.

4.3 Coupling Efficiency Calculation

There are several causes of interconnect loss between a fiber and a waveguide [50],[55],[57]. These include mode field mismatch, transverse offset (x, y offset), longitudinal separation (z offset), angular offset, and reflection. The loss mechanisms addressed in this study were the transverse offset and mode field mismatch. Mode field mismatch contributes significantly to interconnect loss [37],[57], hence modeling is a necessary tool to design a waveguide whose field profile closely matches that of the input fiber. Physically, mode field mismatch is directly related to the difference between the field profiles of the two components. Since misalignment in the x and y directions is inevitable in practice, the theoretical coupling efficiency results for x

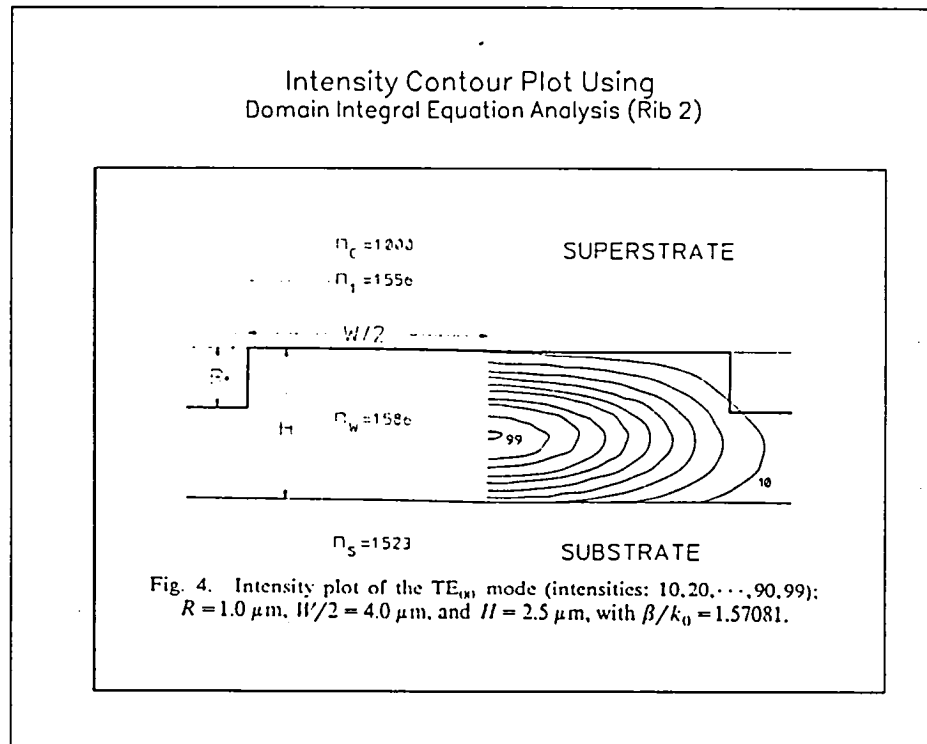


Figure 4.27: Field intensity contour plot for Rib 2.

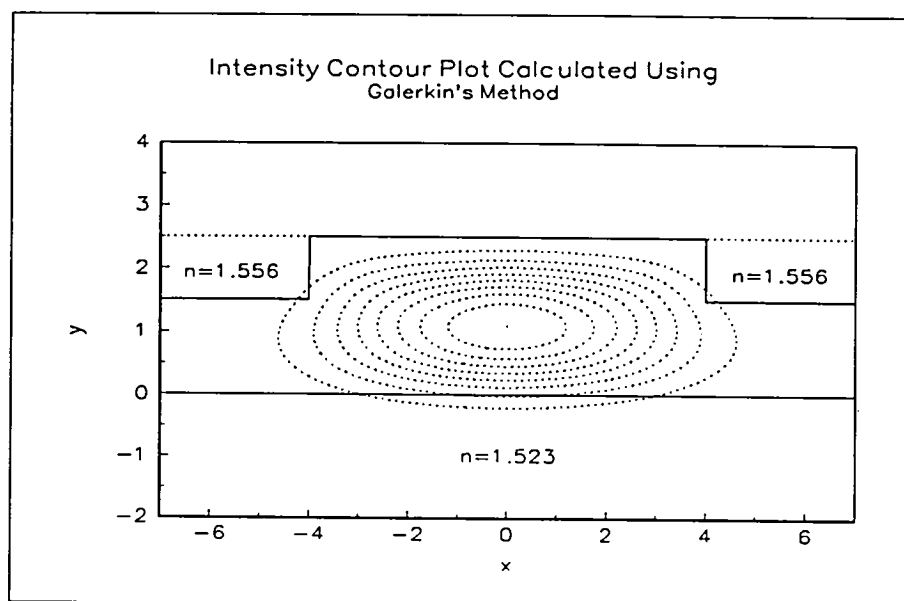


Figure 4.28: Field intensity contour plot for rib 2.

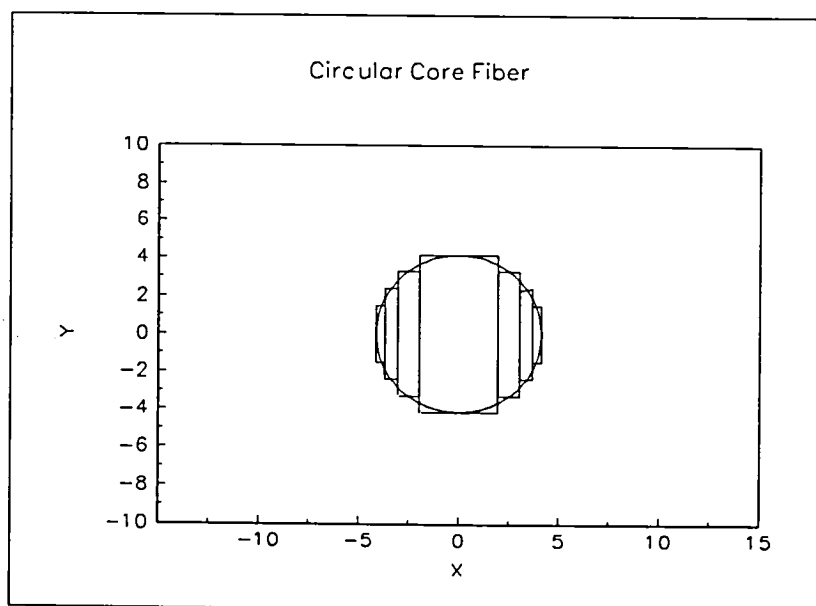


Figure 4.29: Circular-core fiber and rectangles used for approximation.

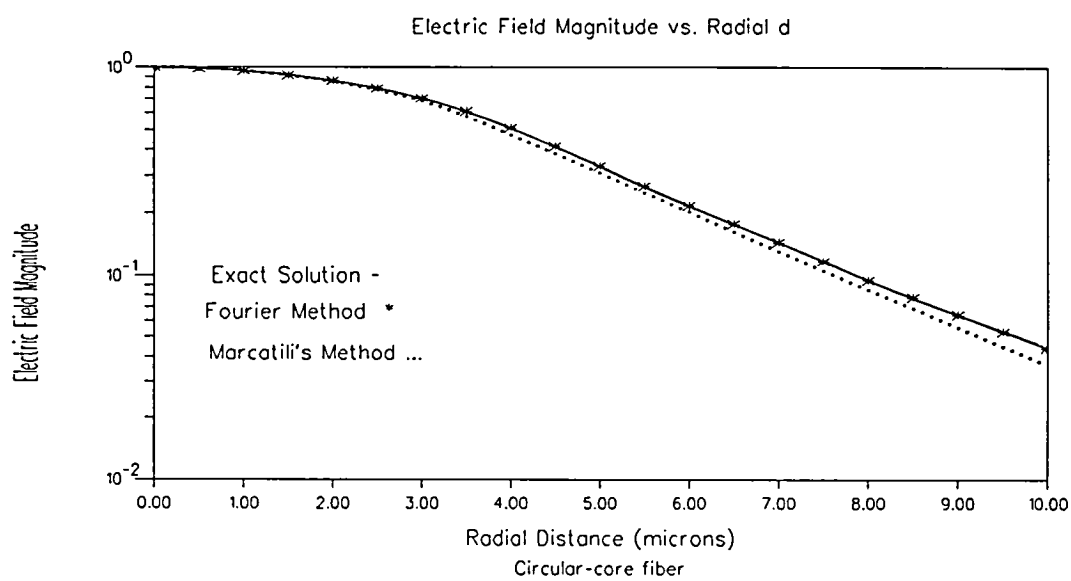


Figure 4.30: Field amplitude versus radial distance for circular-core optical fiber.

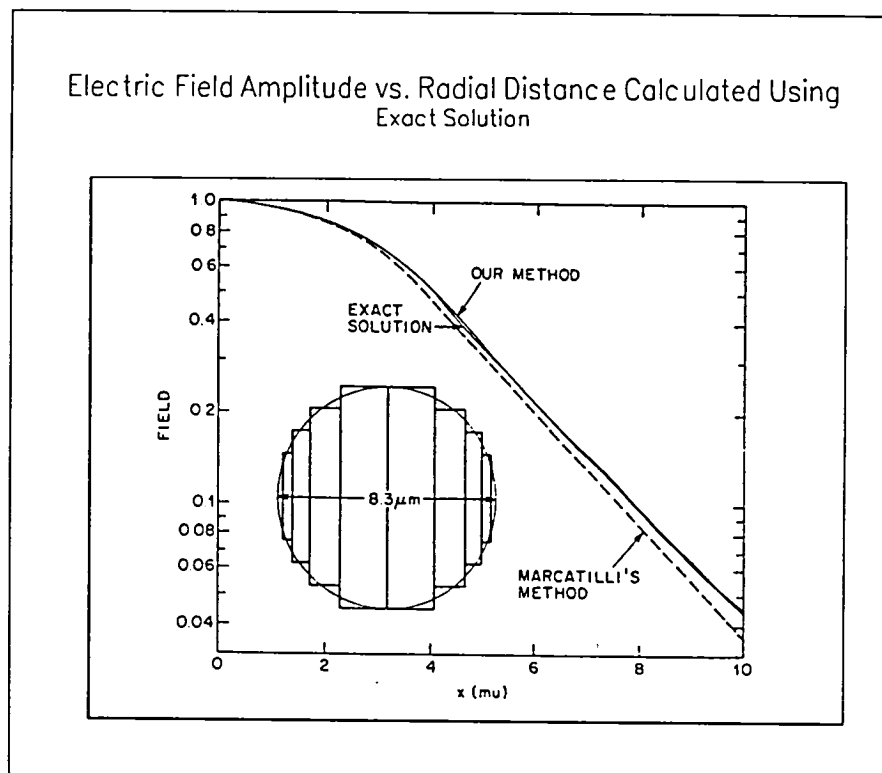


Figure 4.31: Exact field solution for circular-core fiber.

and y offsets are of interest. Because the index of refraction difference between the fiber and waveguide was small, Fresnel reflection loss was neglected [57].

Once the electric fields of the rib guide and fiber are calculated, the efficiency of coupling between the two components can be determined. The coupling efficiency, η , is calculated using the overlap integral [87],

$$\eta = \frac{\left| \int \int E_f(x, y) E_g^*(x, y) dx dy \right|^2}{\int \int E_f(x, y) E_f^*(x, y) dx dy \int \int E_g(x, y) E_g^*(x, y) dx dy}, \quad (4.119)$$

where the integrals are taken over all space and $E_f(x, y)$ and $E_g(x, y)$ are the electric field profiles of the fiber and rib waveguide, respectively. For the EIM and Marcatili's method, this integration is performed directly. Recall for the Fourier method, both the fiber and rib fields are calculated using the same orthonormal basis functions, boundaries, and number of expansion (m and n). Thus, the coupling efficiency is determined as the integral of the product of the fiber and rib guide fields squared, which is

$$\sum_{\mu} \sum_{\nu} A_{\mu\nu} B_{\mu\nu}, \quad (4.120)$$

where $A_{\mu\nu}$ and $B_{\mu\nu}$ are the coefficients of the fiber and rib guide, defined by equation (4.116), which are normalized as

$$\sum_{\mu} \sum_{\nu} A_{\mu\nu}^2 = \sum_{\mu} \sum_{\nu} B_{\mu\nu}^2 = 1. \quad (4.121)$$

The coupling efficiency is related to coupling loss by the relation [60]

$$Loss = -10 \log_{10} \eta \text{ dB}. \quad (4.122)$$

The major axis of the elliptical-core fiber was oriented parallel to the x axis of the guide. The position of zero x and y offset is chosen to correspond to alignment

of the maximum field positions of the fiber and rib [60]. After solving for the aligned case, various x offsets were introduced and a new coupling efficiency calculated for each at two temperatures. This procedure was then repeated for various y offsets while the x offset was zero.

4.4 Concluding Remarks

The field solution for a three-layer planar guide was discussed to provide a foundation for understanding the field solutions for the rib guide. Because there is no exact analytical solution for the rib propagation characteristics, three solution techniques were used. These were the EIM, Marcatili's approximation, and the Fourier numerical method. Results from the three methods will be compared in Chapter V.

The validity of the Fourier method was studied by comparing known solutions to those calculated using the Fourier method. Good agreement between the results was found, confirming the accuracy of the method and supporting its use as the baseline numerical method for comparison with the approximation techniques.

The fiber does have an analytical solution which cannot be determined in closed form, however, it was determined that the three techniques used to solve the rib were also applicable to the fiber, and were expected to produce accurate field results.

Table 4.4: Effective Index Results

Method	Effective Index
EIM	1.44931
Perturbation to Marcatili's Technique	1.44813
the Fourier Method	1.44817

CHAPTER V

RESULTS

This chapter is divided into two main sections; room temperature results and 300°C results. These two temperatures were chosen to represent a nominal and high temperature between which the guide is expected to operate when located near the inlet of an aircraft engine. Results from the coupling efficiency calculations performed at these two temperatures indicate that the device is expected to function properly in this environment.

The field results for both the rib waveguide and elliptical-core fiber will be discussed. The field profiles and coupling efficiency results for x and y offsets will be shown in graphical format. Results for the effective index of both the rib guide and fiber as well as the maximum coupling efficiency calculated between the two components, using the three techniques, will be given in tabular format for comparison.

5.1 Rib Waveguide Results (20°C)

5.1.1 Field Results

Theoretical field results using the EIM, Marcatili's approximation and the Fourier method are illustrated using contour plots. For all the contour plots in this dissertation, each contour indicates a region of equal field magnitude in increments of 0.1, with the maximum field magnitude being equal to 1.0.

The field profile calculated using the EIM is shown in Figure 5.32, with the rib cross-section superimposed. For this method, the solutions to N_I and N_{II} for the constituent guide were 1.5022 and 1.4938, respectively. These values were used to calculate the field as previously discussed.

Using Marcatili's method, the results for β_1 and β_2 were 11.7134 and 11.3120 $\frac{1}{\mu m}$, respectively. The contour plot of the electric field calculated using these variables is shown in Figure 5.33. Field results calculated using the Fourier numerical technique are shown in Figure 5.34.

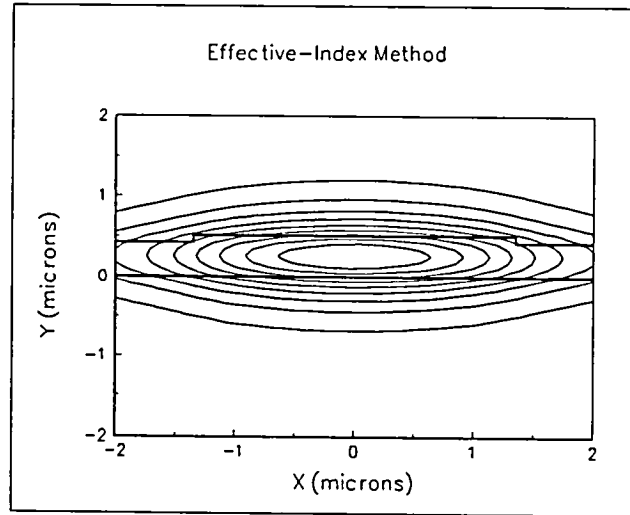


Figure 5.32: EIM: electric field contours of rib guide.

5.1.2 Effective Index Results - Rib

The results of the calculated effective index, n_e , for the rib waveguide using the three methods are given in Table 5.5. The result using Marcatili's method was 1.4963, which was improved by including the perturbation correction, 0.2186.

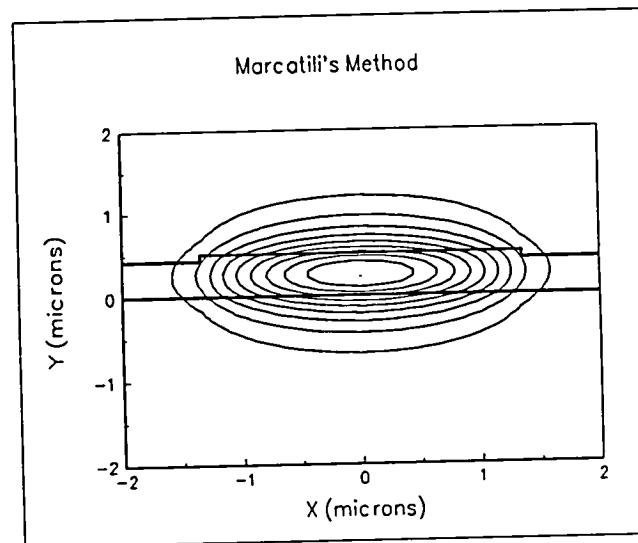


Figure 5.33: Marcatili's method: electric field contours of rib guide.

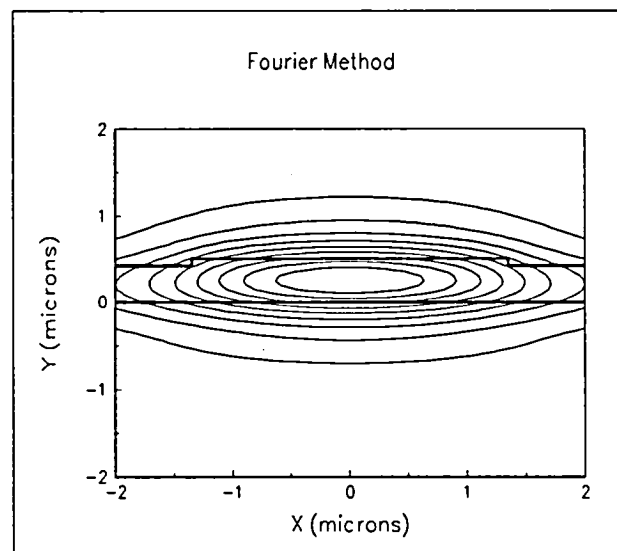


Figure 5.34: Fourier Method: electric field contours of rib guide.

Table 5.5: Rib Effective Index Results (20°C)

METHOD	n_e
EIM	1.4994
Perturbation (to Marcatili's Method)	1.4966
Fourier	1.4993

5.1.3 Comparison

Field results using the EIM were very similar to those from the Fourier method, yet required considerably less computation time. The difference between the fields calculated using the EIM and Fourier method are shown in Figure 5.35. Marcatili's method assumed a tightly confined field, hence the results produced a field more tightly confined than the EIM and the Fourier method. The difference between the field calculated using Marcatili's method and the Fourier method is illustrated in Figure 5.36. Results using the two approximation techniques were completed in a matter of minutes on a computer, however, using the Fourier method, the computation took a few hours on a Pentium computer.

Effective-index results using the EIM and the Fourier method were nearly identical, with a difference of 0.007%; whereas between the perturbation method and Fourier method it was 0.18%. As evidenced here, the EIM is known to consistently predict a higher effective index than the actual value while the perturbation correction to Marcatili's method predicts a lower effective index. Hence, the actual effective index value is bounded above by the EIM result and below by Marcatili's result.

5.2 Fiber Results (20°C)

5.2.1 Field Results

Modeling the elliptical fiber as a rectangle, the field results using the EIM are shown in Figure 5.37 with the fiber elliptical-core cross-section superimposed. For this technique the calculated N_I value was 1.4703 and 1.45 was used for N_{II} . Utilizing Marcatili's method, the fiber field profile was determined using the calculated β_1 and β_2 values, of 11.1892 and 11.1300 $\frac{1}{\mu m}$, respectively. A contour plot of the electric field

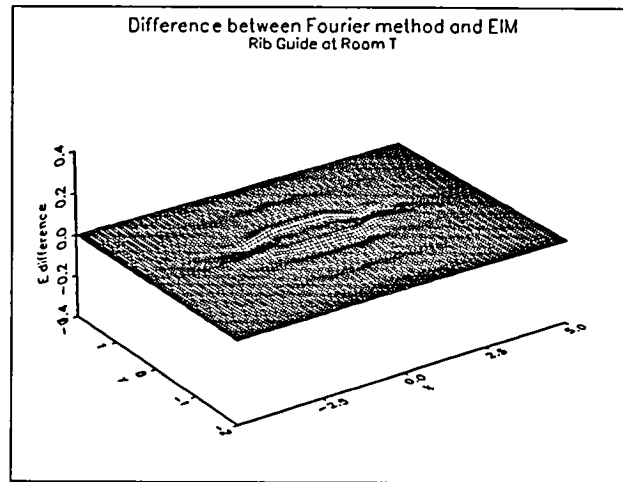


Figure 5.35: Difference between Fourier field result and EIM field result for the rib waveguide.

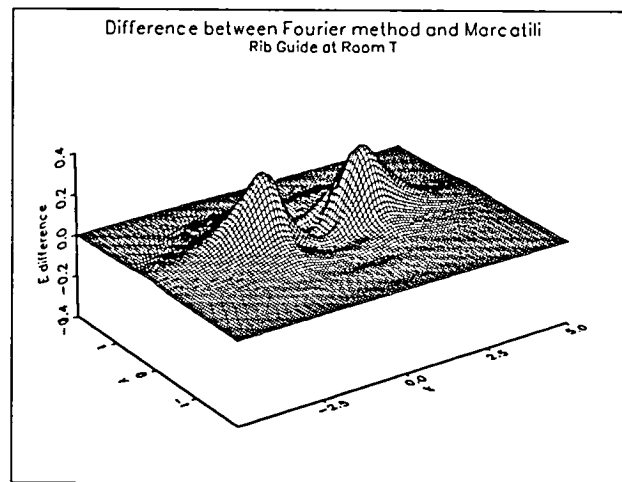


Figure 5.36: Difference between Fourier field result and Marcotili's field result for the rib waveguide.

is shown in Figure 5.38. Field results using the Fourier method for the elliptical-core fiber are shown in Figure 5.39. Analogous to the procedure used for the rib, a $15\ \mu\text{m}$ by $10\ \mu\text{m}$ evaluation domain was used.

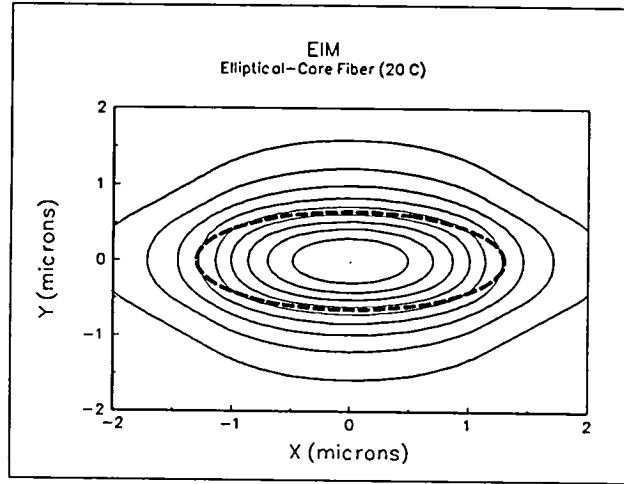


Figure 5.37: EIM: electric field contours of elliptical-core fiber.

5.2.2 Effective Index Results - Fiber

The effective index of the elliptical-core fiber was calculated using the three solution methods with results shown in Table 5.6. The perturbation correction was 0.3678, producing a corrected effective index of 1.4651. Using Marcatili's technique, the calculated fiber birefringence was 2.5×10^{-4} [41] using equation (3.10), where β_x and β_y denote the propagation constants for the TE and TM modes, respectively. This birefringence compares favorably with the manufacturer's nominal value of 1.5×10^{-4} [78].

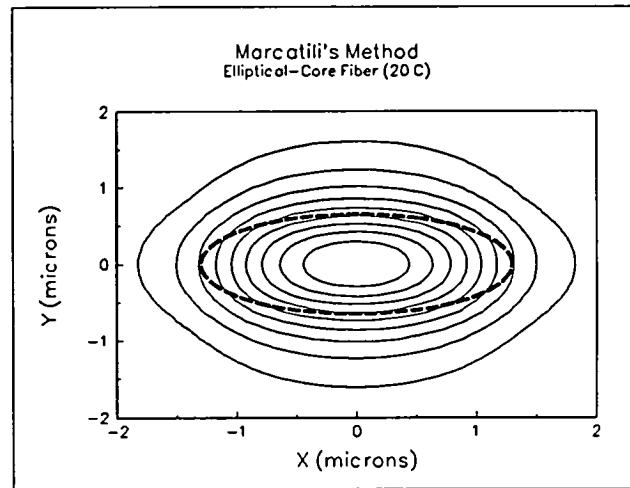


Figure 5.38: Marcatili's method: electric field contours of elliptical fiber.

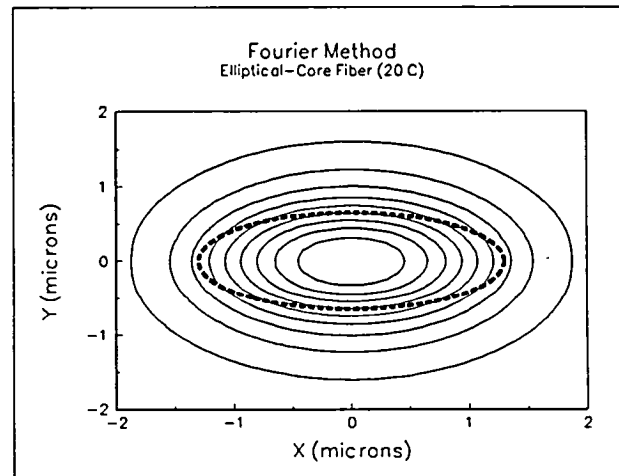


Figure 5.39: Fourier method: electric field profile of elliptical-core fiber.

Table 5.6: Fiber Effective Index Results (20°C)

METHOD	n_e
EIM	1.4653
Perturbation (to Marcatili's Method)	1.4651
Fourier	1.4652

5.2.3 Comparison

Both the field and effective-index results from all three techniques agreed well for the fiber. Differences between the electric field profile calculated using the EIM and Marcatili's method with respect to the Fourier method are shown in Figures 5.40 and 5.41. From these graphs, it appears that the field calculated using the EIM more closely matches that using the Fourier method than the field calculated using Marcatili's method.

The difference between the effective-index calculated using the EIM and the Fourier method was 0.0068% which was the same as the percent difference between the perturbation correction to Marcatili's method and the Fourier method. The EIM overapproximated the effective index while the perturbation correction to Marcatili's method underestimated it. In this case, the two approximation methods produced an effective index that was nearly identical to that of the Fourier method.

5.3 Coupling Efficiency Results

The zero x and y offset position was defined as the alignment of the maximum field positions of the fiber and rib such that the maximum coupling efficiency occurs at this position. An offset in the x direction was then introduced which ranged from $-3 \mu m$ to $+3 \mu m$ in $0.10 \mu m$ increments. The coupling efficiency between the fiber and rib guide, calculated using the three different methods, is shown in Figure 5.42 as a function of the x offset. It was evident from this graph that the EIM and the Fourier method predicted similar results. Marcatili's method predicted the fields of both components more tightly confined in the x direction, which produced a coupling efficiency more sensitive to an x offset. For instance, given a $1 \mu m$ x

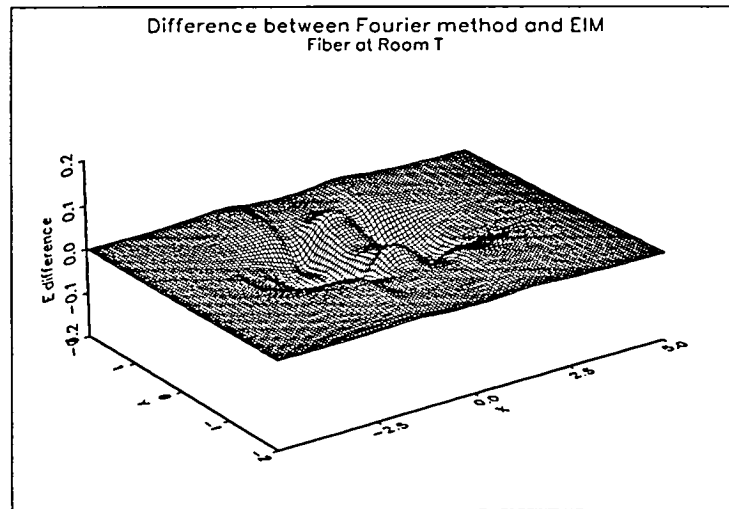


Figure 5.40: Difference between Fourier field result and EIM's field result for the elliptical-core fiber.

offset, the predicted coupling efficiency using the Fourier method was 55%, whereas for Marcatili's method it was 42%.

Similarly for the y direction, keeping the x alignment, the fiber position was varied from $-3 \mu\text{m}$ to $+3 \mu\text{m}$ from the position of alignment. The theoretical coupling efficiency results versus y offset are shown in Figure 5.43. For a $1 \mu\text{m}$ y offset, the predicted coupling efficiency was 18.0% and 18.5% for the Fourier and Marcatili methods, respectively. The coupling efficiency versus y offset was nearly identical for the three methods.

From the graphs in Figures 5.42 and 5.43, it was apparent that alignment was more critical in the y direction. This was expected since the rib field calculated was more tightly confined in the y direction than the x . Using the Fourier method, a

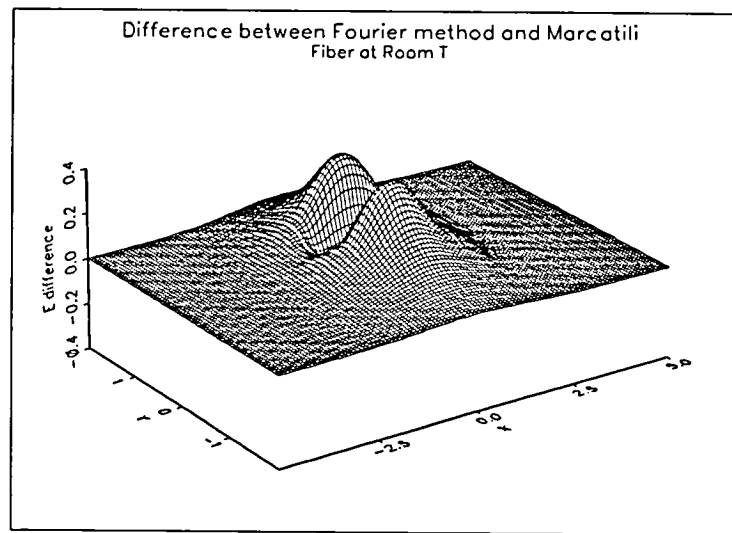


Figure 5.41: Difference between Fourier field result and Marcatili's field result for the elliptical-core fiber.

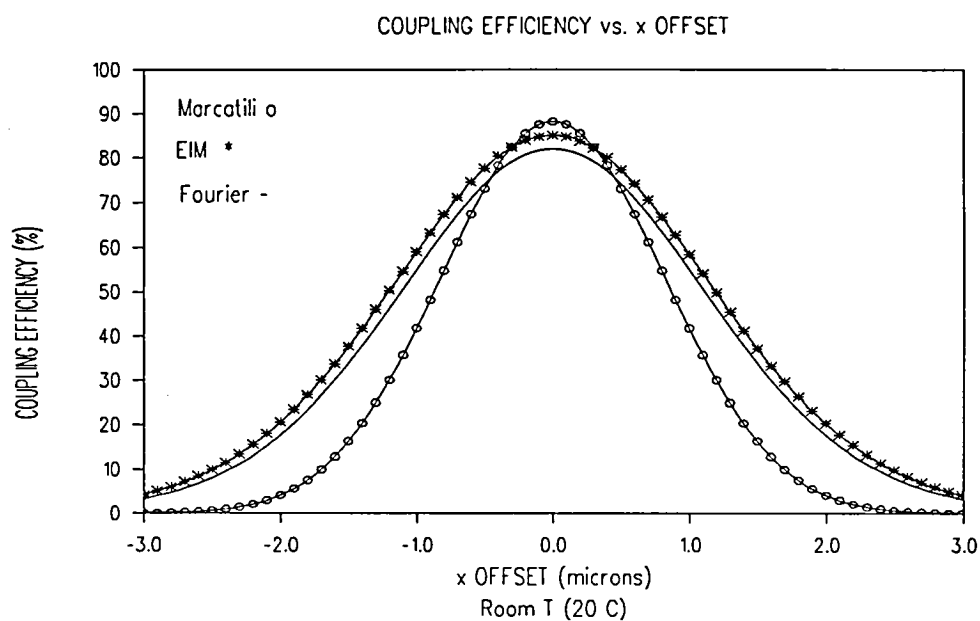


Figure 5.42: Calculated coupling efficiency vs. x offset.

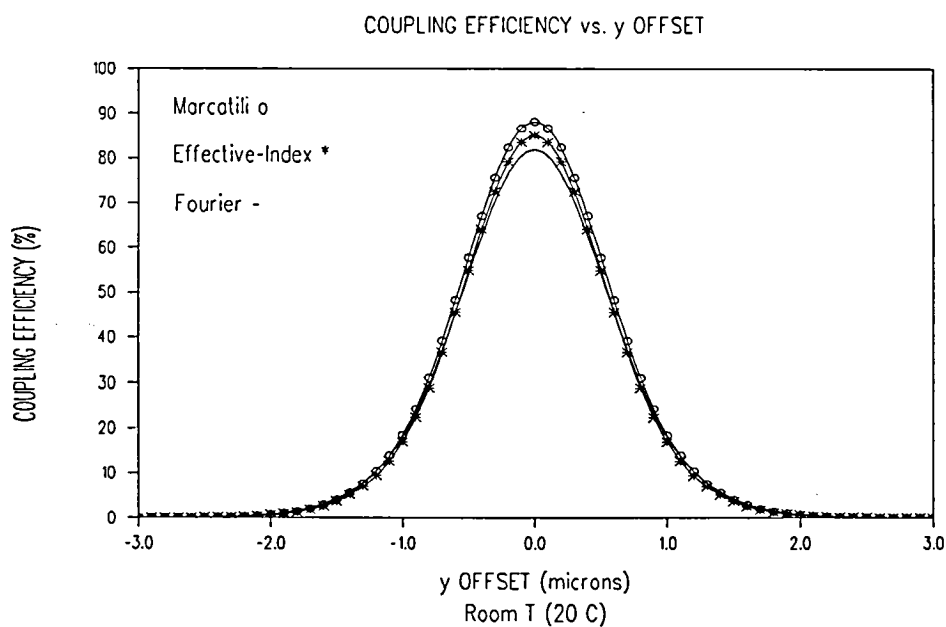


Figure 5.43: Calculated coupling efficiency vs. y offset.

1 μm x offset had a predicted coupling efficiency of 55% whereas a 1 μm y offset had 18.0%. Offsets in the y direction produced coupling efficiency results that were nearly symmetric in y . Only a slight asymmetry in the coupling efficiency results versus y offset was determined, which was so slight that it could not be visually detected from the graphical results.

The maximum theoretical coupling efficiency results are shown in Table 5.7 to four significant figures. This was done to illustrate the minimal changes in the predicted coupling efficiency with temperature. Results using Marcatili's method appeared to be the least accurate due to the method's assumption of a tightly bound field. The results using the EIM and the Fourier method were similar, leading to the deduction that the EIM is the more accurate approximation technique for this type of rib structure.

The zero offset position, in which the maximum field position of the fiber and guide are aligned does not necessarily produce the maximum coupling efficiency [88]. However, due to the symmetry of the rib structure and fiber being studied, the zero offset position was the maximum coupling efficiency position. This was evident in the symmetry of the coupling efficiency graphs versus offset.

5.4 Rib Waveguide Results - 300°C

5.4.1 Physical Changes Due to Temperature

Compared to the 20°C data, the rib and fiber parameters changed slightly when calculated at 300°C. The nominal values for all the parameters were taken at room temperature. The physical features of the rib were determined at 300°C using the relations from Table 3.2, with the subsequent results given in Table 5.8.

Table 5.7: Maximum Coupling Efficiency ($20^{\circ}C$)

METHOD	MAXIMUM COUPLING EFFICIENCY
EIM	85.0348%
Marcatili	88.1608%
Fourier	81.9948%

Table 5.8: Rib Guide Parameter Changes with Temperature

PARAMETER	Equation to Determine Change	RESULT
$W(300^{\circ}C)$	$W(20^{\circ}C) + (6.295 \times 10^{-6} \frac{\mu m}{^{\circ}C} \times 280^{\circ}C)$	$2.701761 \mu m$
$t_{overlay}(300^{\circ}C)$	$t_{overlay}(20^{\circ}C) + (-9.119 \times 10^{-8} \frac{\mu m}{^{\circ}C} \times 280^{\circ}C)$	$0.508975 \mu m$
$t_{unetched}(300^{\circ}C)$	$t_{unetched}(20^{\circ}C) + (-9.245 \times 10^{-8} \frac{\mu m}{^{\circ}C} \times 280^{\circ}C)$	$0.515974 \mu m$
$t_{etched}(300^{\circ}C)$	$t_{etched}(20^{\circ}C) + (-7.632 \times 10^{-8} \frac{\mu m}{^{\circ}C} \times 280^{\circ}C)$	$0.425979 \mu m$
$n_{overlay}(300^{\circ}C)$	$n_{overlay}(20^{\circ}C) + (1.20345 \times 10^{-5} \frac{\mu m}{^{\circ}C} \times 280^{\circ}C)$	1.45637
$n_{rib}(300^{\circ}C)$	$n_{rib}(20^{\circ}C) + (1.1865 \times 10^{-5} \frac{\mu m}{^{\circ}C} \times 280^{\circ}C)$	1.55632
$n_{isolation}(300^{\circ}C)$	$n_{isolation}(20^{\circ}C) + (1.2035 \times 10^{-5} \frac{\mu m}{^{\circ}C} \times 280^{\circ}C)$	1.45637

The isolation layer thickness was not included in this table because that layer was modeled as infinite, hence any minute change in thickness would not alter the results. From the results shown in Table 5.8, it was apparent that the substrate stretched the film causing the rib width to increase while its height decreased. Also, the index of all three layers increased with the increase in temperature. The temperature induced change in the index of refraction was two orders of magnitude greater than the change due to the photoelastic effect, thus being the dominant effect.

5.4.2 Field Results - Rib

For the EIM, the rib field calculated at 300°C is shown in Figure 5.44. Field results for the rib waveguide using the Fourier and Marcatili's methods are shown in Figures 5.45 and 5.46. Comparing these graphical results, the fields calculated using the EIM and the Fourier method were remarkably similar. These field contours were nearly identical to those calculated using 20°C parameters.

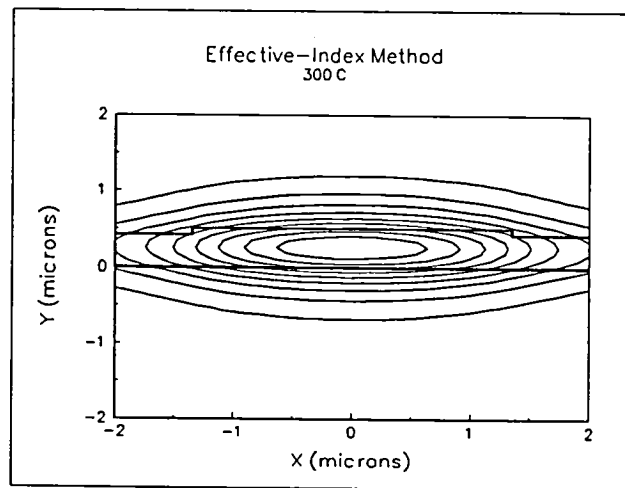


Figure 5.44: EIM: electric field contours of rib at 300°C .

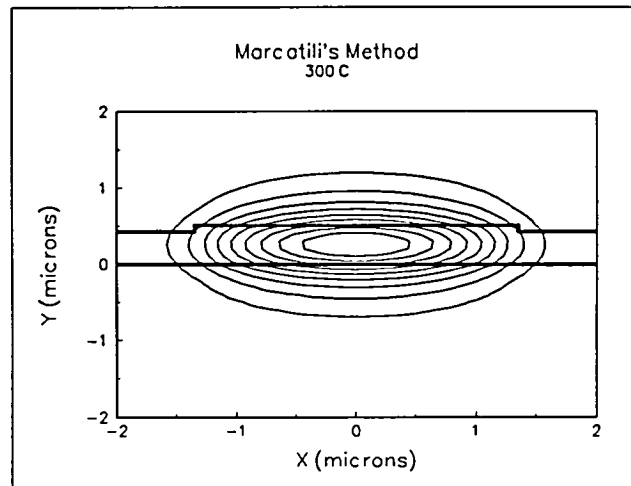


Figure 5.45: Marcatili's method: electric field contours of rib at 300°C.

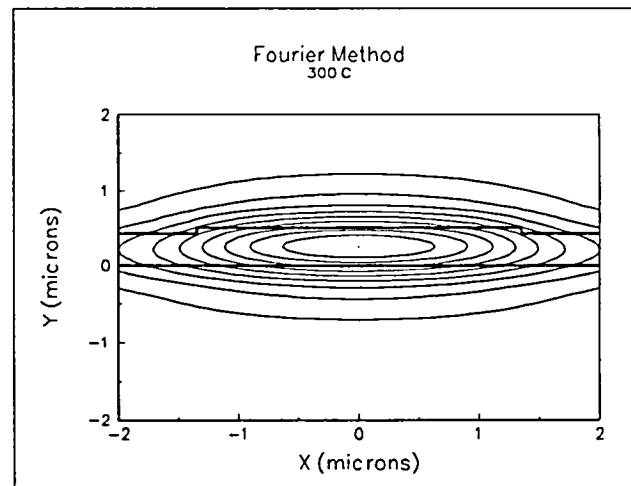


Figure 5.46: Fourier method: electric field contours of rib at 300°C.

5.4.3 Effective-Index Results - Rib

The effective indexes predicted by the three methods for the rib are given in Table 5.9. For the EIM, the values calculated for N_I and N_{II} were 1.5053 and 1.4968, respectively. The propagation constants, β_1 and β_2 , calculated using Marcatili's method were 11.7388 and 11.3876 $\frac{1}{\mu m}$, respectively. The perturbation correction to the propagation constant calculated using Marcatili's technique was 0.2182.

5.4.4 Comparison - Rib

Field results from the three methods at 300°C were nearly identical to the field results at room temperature. There was minimal change in the field results calculated at the two temperatures.

The difference between the effective-index results calculated using the EIM and the Fourier method was 0.0003% whereas between Marcatili's method and the Fourier method it was 0.15691%. This difference was less than that observed between the room temperature results. The effective index change between room temperature and 300°C was 0.00308 using the Fourier method.

5.5 Fiber Results - 300°C

5.5.1 Physical Changes Due to Temperature Increase

Using the values for parameter change per °C, given in Table 3.3, changes in the indexes and core dimensions were determined and results shown in Table 5.10. Using these calculated parameter values, the field and propagation constant were determined using the three methods at this higher temperature. Compared to the room temperature values, the diameter of the fiber's major axis increased by 0.004296

Table 5.9: Rib Effective Index Results ($300^{\circ}C$)

METHOD	n_e
EIM	1.50239
Perturbation (to Marcatili's Method)	1.50003
Fourier	1.50238

Table 5.10: Fiber Parameter Change With Temperature

PARAMETER	Temperature Change	PARAMETER ($300^{\circ}C$)
a	$a(20^{\circ}C) + (7.15 \times 10^{-7}/^{\circ}C \times 280^{\circ}C)$	$1.302148 \mu m$
b	$b(20^{\circ}C) + (3.58 \times 10^{-7}/^{\circ}C \times 280^{\circ}C)$	$0.651074 \mu m$
n_{core}	$n_{core}(20^{\circ}C) + (1.28 \times 10^{-5} \times 280^{\circ}C)$	1.4868
$n_{cladding}$	$n_{cladding}(20^{\circ}C) + (1.28 \times 10^{-5} \times 280^{\circ}C)$	1.4528

Table 5.11: Fiber Effective Index Results ($300^{\circ}C$)

METHOD	n_e
EIM	1.4681
Perturbation (to Marcatili's Method)	1.4679
Fourier	1.4680

μm and the minor axis increased by $0.002148 \mu m$. The indexes of both the fiber core and cladding increased by 0.0028 .

5.5.2 Field Results

Field results for the fiber at $300^\circ C$ calculated using the three methods are illustrated in Figures 5.47 - 5.49. Graphical results appear very similar to those at room temperature. For Marcatili's method, results for β_1 and β_2 were 11.2105 and $11.1514 \frac{1}{\mu m}$, respectively.

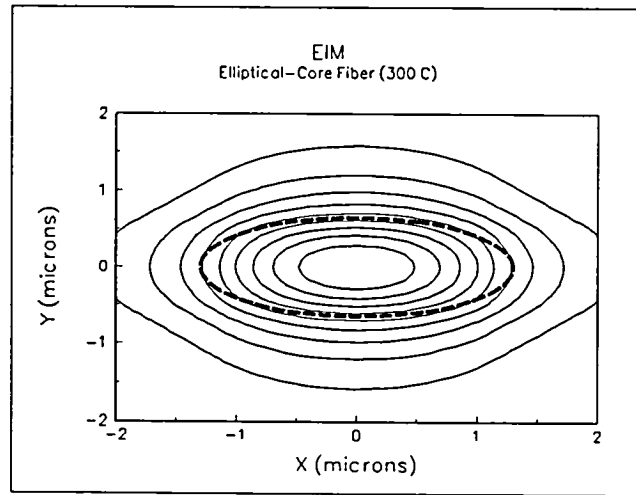


Figure 5.47: EIM: electric field contours of fiber at $300^\circ C$.

5.5.3 Effective Index Results - Fiber

The effective indexes predicted by the three methods for the fiber are given in Table 5.11. For the EIM, the calculated values of N_I and N_{II} were 1.4731 and 1.4528 , respectively. The perturbation correction to the propagation constant determined

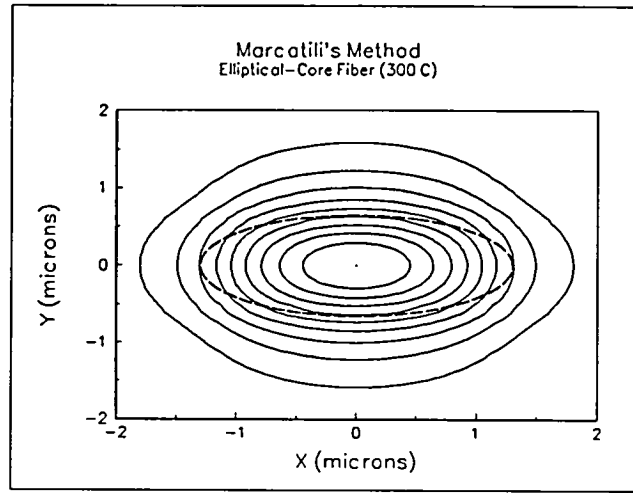


Figure 5.48: Marcatili's method: electric field contours of fiber at 300°C .

using Marcatili's technique was 0.3672. At 300°C , the difference between the results from the EIM method and the Fourier method was 0.0044%.

5.5.4 Comparison of Fiber Results

Results from the Fourier method were expected to be the most accurate. However, the computation time required by this method was orders of magnitude greater than that required by the approximation techniques. From the two approximation methods, the field predicted by Marcatili's method was expected to be more accurate than the EIM. However, graphical field results indicate the opposite, as both approximation methods had a 0.0068% difference in the effective index compared to the Fourier results. Compared to the room temperature result using the Fourier method, the effective index of the fiber increased by 0.0028.

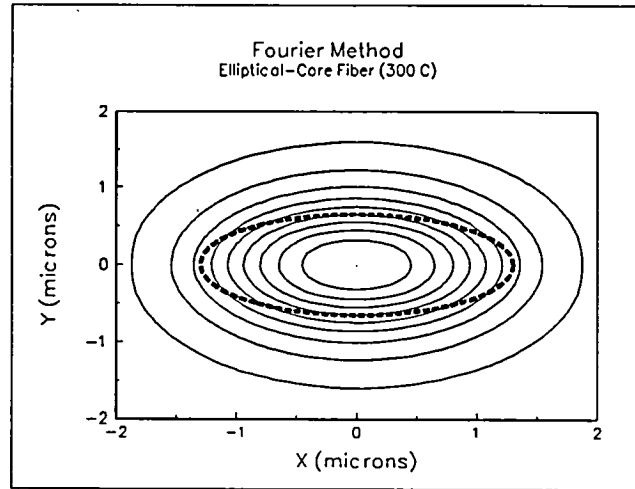


Figure 5.49: Fourier method: electric field contours of fiber at 300°C .

5.6 Coupling Efficiency Results

The maximum field positions of both components were aligned for the zero offset position at 300°C . Due to the symmetry of both components, the maximum coupling efficiency occurred at this perfect alignment position. Graphs of the coupling efficiency versus x and y offsets are given in Figures 5.50 and 5.51.

For the x offsets, Marcatili's method and the Fourier method predicted significantly different results. For instance, given a $1.0\ \mu\text{m}$ x offset, the coupling efficiency was predicted to be 42% and 55% for Marcatili's and the Fourier method, respectively. These are the same coupling efficiency values determined at room temperature.

For the y offsets, the three methods calculated nearly identical coupling efficiencies. This was due to all three methods predicting similar y field confinement. For a $1.0\ \mu\text{m}$ y offset, the predicted coupling efficiency was 17.9% and 18.4% for the Fourier and Marcatili methods, respectively. This result was slightly less than

the 18.0% and 18.5% coupling efficiency predicted at room temperature for the same offset.

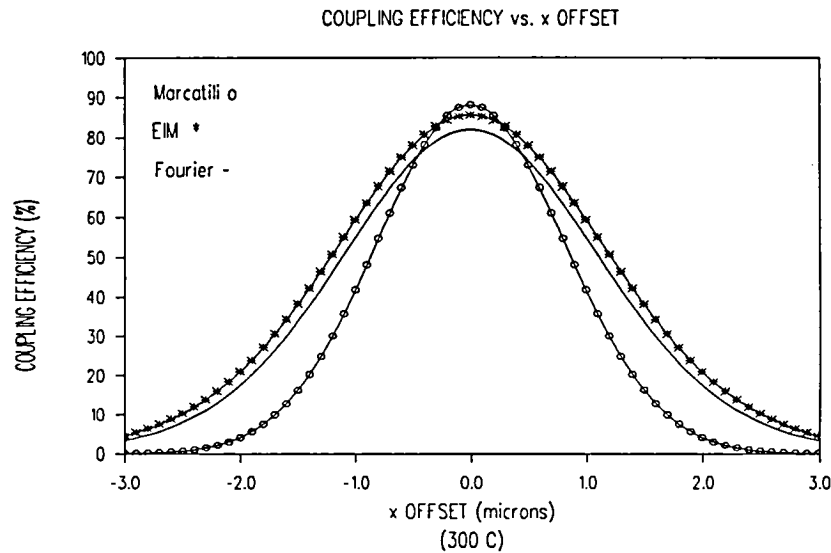


Figure 5.50: Calculated coupling efficiency vs. x offset at 300°C.

Results from the three techniques are given in tabular form in Table 5.12. From this theoretical study, it appears that the coupling efficiency decreases slightly with temperature, by approximately 0.02% using the Fourier method. Results from Marcatili's method predicted a slight decrease in the maximum coupling efficiency, 0.01%, while the EIM predicted an increase of 0.2%. These predicted changes in the coupling efficiency with temperature are negligible and would be difficult to detect in practice.

Table 5.12: Maximum Coupling Efficiency (300°C)

METHOD	MAXIMUM COUPLING EFFICIENCY
Effective Index	85.1815%
Marcatili	88.1462%
Fourier	81.9774%

5.7 Coupling Efficiency Optimization

The optical fiber is commercially available, thus, its parameters cannot be altered. The waveguide can be altered slightly, within physical constraints, to maximize the fiber to rib guide coupling. A preliminary study was performed to determine if the coupling efficiency could be improved. Each parameter was varied to deduce its affect on the coupling efficiency. It was determined that the coupling efficiency increased with decreased rib width and also with increased etch depth. These modified rib waveguide dimensions more closely match the fiber dimensions. Combining the two parameter changes produced the largest increase in the coupling efficiency, 6%, for a maximum coupling efficiency of 88%. Using these new parameters, the coupling efficiency versus x and y offsets was calculated. Results of this calculation are shown in Figures 5.52 and 5.53. Offset affects on the coupling efficiency indicate that the device is more lenient in the x offset tolerance while more sensitive to y offsets.

5.8 Summary

Results indicate that the EIM was surprisingly accurate for both the fiber and rib waveguide, given its lack of enforcement of the field boundary conditions. The EIM is known to consistently predict a higher n_e , which was observed in this study. Temperature induced variations of the rib and fiber indexes and dimensions were much less than expected. Due to the different coefficients of thermal expansion for the rib layers, the rib was stretched by the substrate expansion which slightly decreased its height. The indexes of both the fiber and rib guide increased slightly with the temperature increase. The field profiles of both components at the two temperatures were nearly identical. While results from the Fourier method were more

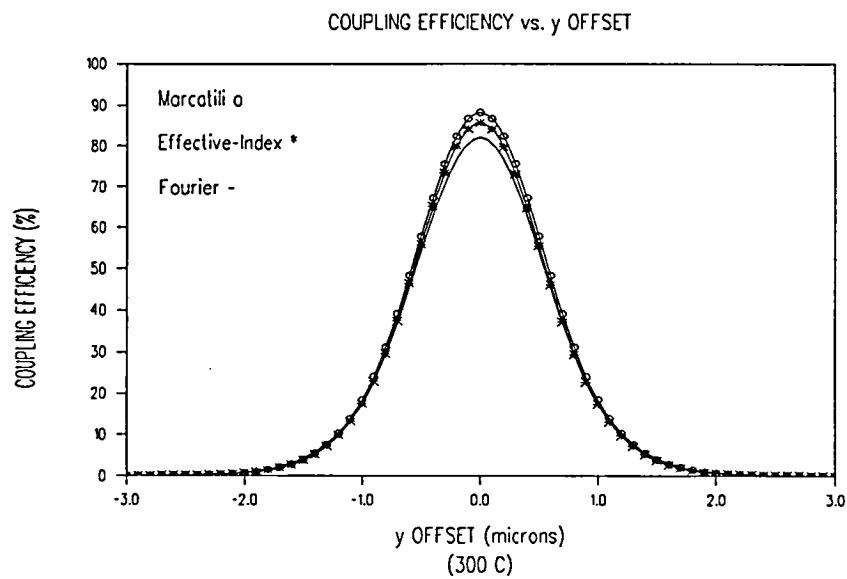


Figure 5.51: Calculated coupling efficiency vs. y offset at 300°C.

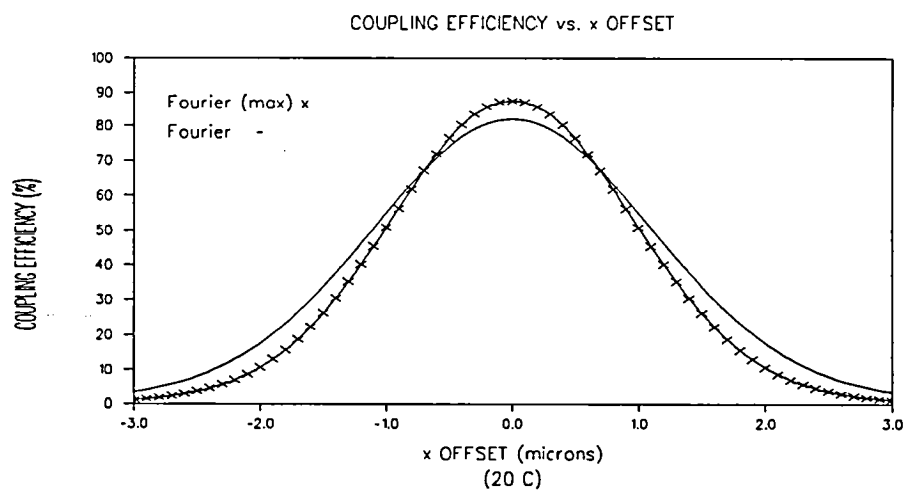


Figure 5.52: Optimum rib waveguide coupling efficiency vs. x offset from the preliminary study.

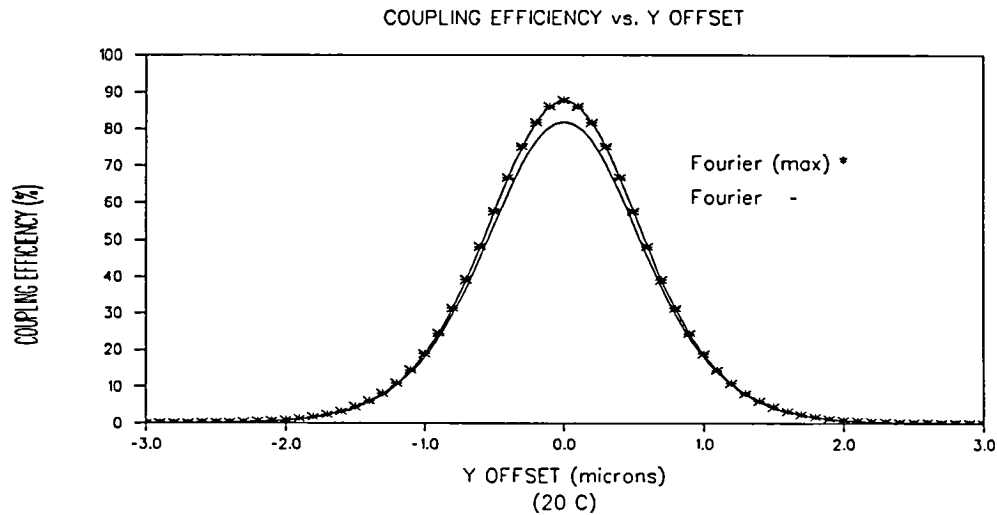


Figure 5.53: Optimum rib waveguide coupling efficiency vs. y offset from the preliminary study.

accurate, the amount of time required to determine the coupling efficiency for x and y offsets was several orders of magnitude greater than that for the approximation methods.

These results indicate that the device is likely to perform properly in an environment with a temperature fluctuating between the two temperatures investigated. The calculated maximum coupling efficiency was higher than expected. Changes in the coupling efficiency with temperature were negligible, and the parameter changes with temperature were lower than expected.

CHAPTER VI

CONCLUSION

6.1 Summary

The electric field profiles of an elliptical-core fiber and a SiON rib waveguide were determined using three methods: two approximation and one numerical. These calculations were performed for room temperature and 300°C parameters. From the field results, the maximum coupling efficiency between the two components was calculated from the overlap integral and found to be higher than expected. Prior to this work, the coupling efficiency had been calculated between a single-mode circular-core fiber and the rib waveguide under study. Results from that work indicated an expected coupling efficiency of only 45% [75]. Therefore, choosing an elliptical-core fiber improved the device coupling efficiency by nearly a factor of 2.

These results indicate that the device is likely to perform in an environment whose temperature ranges from 20°C - 300°C . Changes in the physical parameters with temperature were lower than expected over the 280°C range.

As an offshoot to the problem under study, a comparison of the three solution techniques was performed. The Fourier method was expected to produce the most accurate results for both the fiber and rib guide. Therefore, compared to the Fourier method, it was determined that the EIM produced more accurate results for the rib guide and elliptical-core fiber. For an additional comparison, Marcatili's method was to determine the fiber field and the EIM for the rib. The predicted coupling efficiency

was 81% at room temperature [89], which compares favorably with the Fourier prediction of 82%. Calculations using the Fourier method are computationally intensive while results using the approximation techniques are achieved in minutes, making the approximation techniques useful for preliminary studies.

The theoretical coupling efficiency between an elliptical-core fiber and a rib guide was determined for a range of transverse offsets. Three techniques were used to calculate the theoretical electric field profile of the rib waveguide: the EIM, Marcatili's technique, and the Fourier method. For this channel structure, the EIM and the Fourier method produced similar results. Results from Marcatili's method were not as accurate for the particular rib guide being studied. Similarly, for the fiber, the EIM was determined to be more accurate than Marcatili's approximation technique.

The coupling efficiency results determined using the three methods compared well. Calculations of this kind are essential to optimize the design of a rib guide in order to provide an acceptably low coupling loss.

6.2 Significance of Work

The fiber and rib waveguide were determined to be compatible for interconnection over the 20°C - 300°C temperature range. Minimal changes were determined over this temperature range for the field profiles of the components and the associated coupling efficiency. The rib waveguide under study could be implemented as the input stage for a variety of sensors fabricated using SiON as the guiding layer. These sensors would be expected to function in the temperature environment of the inlet of an aircraft engine. Coupling a single-mode fiber to a single-mode device is more sensitive to offsets than coupling a multimode fiber to the same device, due

to the smaller diameter of the single-mode fiber. However, these results indicate that greater than 50% coupling efficiency is predicted for x offsets within $\pm 1 \mu m$ and y offsets within $\pm 0.5 \mu m$. Offsets in the y direction were determined more critical to the coupling efficiency than in the x direction, which must be considered when designing the coupling configuration. These results are encouraging for future experimental research on interconnection for this fiber and rib waveguide.

The analysis also provided a comparison between three techniques with results from the Fourier method expected to be the most accurate. This demonstrated the surprising accuracy of the EIM for both the rib and fiber. Preliminary calculations can be performed using these approximation techniques without sacrificing much accuracy, which will greatly decrease the amount of computation time required. Marcatili's method was determined less accurate than the EIM for both the rib waveguide and fiber. Approximation techniques must be used with care because they are not applicable to every guide geometry.

6.3 Future Work

Plans to experimentally couple the light output of an elliptical fiber into the rib waveguide sensor at room temperature are under way. Differences between the theoretical and experimental results will be studied to determine the cause. Generally, the experimental coupling efficiency versus x or y offset matches the theoretical results multiplied by a transmission coefficient. This transmission coefficient is used to account for reflection loss, propagation loss, and output coupling efficiency [48].

In regards to the rib waveguide, a few researchers have reported a phenomenon where a rib which begins as single-mode will become multimode as the etch

depth increases, which is expected. However, as the etch depth further increases to a critical point, the device become single-mode again. This has been attributed to spurious modes caused by the finite window size. Modeling the rib and varying the etch depths to replicate this phenomenon would be of interest.

Calculations to determine how the coupling efficiency changes with variations in the gap between the fiber and guide would be useful for determining device operation. It would also be interesting to model the rib waveguide using four layers, instead of three, to determine any differences between the results.

The design for coupling the fiber to the waveguide will use a v-groove configuration, hence thermal changes of the groove will affect the alignment. This alignment change with temperature was not considered in this research, however, during the design stage, these thermal effects will be considered and the subsequent coupling efficiency determined. To eliminate loss due to scattering at the fiber/rib interface, it will be necessary to polish the endface of the rib waveguide.

The issue of bonding the fiber into the groove must also be addressed. Using epoxy as a bond is not a practical choice because epoxy degrades at high temperatures and has a different coefficient of thermal expansion than the fiber and guide, thus altering the alignment with temperature. A flip-chip approach may be applicable to this situation.

REFERENCES

- [1] D. Hondros and P. Debye, *Ann. Physik*, Vol. 32, pp. 465, 1910.
- [2] C. Yeh, "Elliptical Dielectric Waveguides," *J. Appl. Phys.*, Vol. 33, No. 11, pp. 3235-3243, 1962.
- [3] D. Thompson and C. Bedoya, "Optical Fiber Finally Takes Off," *Photonics Spectra*, pp. 82-90, April 1995.
- [4] R.J. Baumbick, "Status of the Fiber Optic Control System Integration (FOCSI) Program," NASA Tech. Mem. 106151, 1993.
- [5] Proceedings of 1994 Fiber Optic and Sensors for Aerospace Technology (FOSAT) Workshop, NASA Publication 10166, held October 18-20, 1994.
- [6] Proceedings on Integrated Optics For Military and Commercial Applications, Special Report RD-AS-94-9, held December 7-9, 1993.
- [7] R.M. Knox and P.P. Toulous, "Integrated Circuits for the Millimeter Through Optical Frequency Range," *Proc. MRI Symposium on Submillimeter Waves*, Polytechnic Press, Brooklyn, pp. 497-516, 1970.
- [8] G.B. Hocker and W.K. Burns, "Mode Dispersion in Diffused Channel Waveguides by the Effective Index Method," *Appl. Opt.*, Vol. 16, No. 1, pp. 113-118, 1977.
- [9] W.C. Borland, "Modeling Optical Waveguide Dispersion: Four-Layer Planar, Channel, and Quantum Well Structures," Ph.D. Dissertation, University of Cincinnati, Cincinnati, Ohio, 1989.
- [10] D. Marcuse, Theory of Dielectric Optical Waveguides, Academic Press, New York, pp. 7-8, 49-59, 1991.
- [11] V. Ramaswamy, "Strip-loaded film waveguide," *Bell. Syst. Tech. J.*, Vol. 53, pp. 697-705, 1974.

- [12] K.S. Chiang, "Performance of the Effective-Index Method," *Opt. Lett.*, Vol. 16, No. 10, pp. 714-716, 1991.
- [13] E.A.J. Marcatili, "Dielectric Rectangular Waveguide and Directional Coupler for Integrated Optics," *Bell. Syst. Tech. J.*, 48, pp. 2071-2102, 1969.
- [14] A. Kumar, K. Thyagarajan, and A.K. Ghatak, "Analysis of Rectangular-Core Dielectric Waveguides: An Accurate Perturbation Approach," *Opt. Lett.*, Vol. 8, No. 1, pp. 63-65, 1983.
- [15] R.K. Varshney and A. Kumar, "A Simple and Accurate Modal Analysis of Strip-Loaded Optical Waveguides with Various Index Profiles," *J. Lightwave Tech.*, Vol. 6, No. 4, pp. 601-606, 1988.
- [16] D. Marcuse, "Solution of the Vector Wave Equation for General Dielectric Waveguides by the Fourier Method," *J. Quant. Electron.*, Vol. 28, No. 2, pp. 459-465, 1992.
- [17] A. Kumar and R.K. Varshney, "Propagation Characteristics of Highly Elliptical Core Optical Waveguides: A Perturbation Approach," *Opt. and Quant. Electron.*, Vol. 16, pp. 349-354, 1984.
- [18] K.S. Chiang, "Analysis of Optical Fibers by the Effective-Index Method," *Appl. Opt.*, Vol. 25, No. 3, pp. 348-354, 1986.
- [19] K.S. Chiang, "Review of Numerical and Approximate Methods for the Modal Analysis of Arbitrarily Shaped Microwave and Optical Dielectric Waveguides," *Opt. and Quant. Electron.*, Vol. 26, pp. S113-S134, 1994.
- [20] S.M. Saad, "Review of Numerical Methods for the Analysis of Arbitrarily Shaped Microwave and Optical Dielectric Waveguides," *IEEE Trans. Microwave Theory Tech.*, MTT-33, pp. 894-899, 1985.
- [21] K.S. Chiang, "Performance of the Effective Index Method for the Analysis of Dielectric Waveguides," *Opt. Lett.*, Vol. 16, No. 10, pp. 714-716, 1991.
- [22] K.S. Chiang, "Dual Effective-Index Method for the Analysis of Rectangular Dielectric Waveguide," *Appl. Opt.*, Vol. 25, No. 13, pp. 2169-2174, 1986.

- [23] C.M. Kim, B.G. Jung, and C.W. Lee, "Analysis of Dielectric Rectangular Waveguide By Modified Effective-Index Method," *Electron. Lett.*, Vol. 2, No. 6, pp. 296-298, 1986.
- [24] T.M. Benson, R.J. Bozeat, and P.C. Kendall, "Rigorous Effective Index Method for Semiconductor Rib Waveguides," *IEE Proceedings-J*, Vol. 139, No. 1, pp. 67-70, 1992.
- [25] P.C. Kendall, M.J. Adams, S. Ritchie, and M.J. Robertson, "Theory for Calculating Approximate Values for the Propagation Constants of an Optical Rib Waveguide by Weighting the Refractive Indices," *IEE Proceedings*, Vol. 134, Pt. A, No. 8, pp. 699-702, 1987.
- [26] G.J. Krijnen, H.J.W.M. Hoekstra, and P.V. Lambeck, "A New Method for the Calculation of Propagation Constants and Field Profiles of Guided Modes of Nonlinear Channel Waveguides Based on the Effective Index Method," *J. Lightwave Tech.*, Vol. 12, No. 9, pp. 1550-1559, 1994.
- [27] A. Kumar, M.R. Shenoy, and K. Thyagarajan, "Modes in Anisotropic Rectangular Waveguides: An Accurate and Simple Perturbation Approach," *IEEE Trans. on Microwave Theory and Techniques*, Vol. MTT-32, No. 10, pp. 1415-1418, 1984.
- [28] K.S. Chiang, "Analysis of Rectangular Dielectric Waveguides: Effective-Index Method with Built-In Perturbation Correction," *Electron. Lett.*, Vol. 28, No. 4, pp. 388-390, 1992.
- [29] J.E. Goell, "A Circular-Harmonic Computer Analysis of Rectangular Dielectric Waveguides," *Bell Syst. Tech. J.*, Vol. 48 pp. 2144-2160, 1969.
- [30] D. Yevick and Björn Hermansson, "New Formulations of the Matrix Beam Propagation Method: Application to Rib Waveguides," *IEEE J. Quant. Electron.*, Vol. 25, No. 2, pp. 221-229, 1989.
- [31] E. Valentinuzzi, "Direct Finite Element Computation of Dispersion Parameters Of Optical Waveguides," *Electron. Lett.*, Vol. 30, No. 15, pp. 1217-1219, 1994.
- [32] A. Sharma and P. Bindal, "An Accurate Variational Analysis of Single-Mode Diffused Channel Waveguides," *Opt. and Quant. Electron.*, Vol. 24, pp. 1359-1371, 1992.

- [33] M. Ohtaka, M. Matsuhara, and N. Kumagai, "Analysis of the Guided Modes in Slab-Coupled Waveguides Using a Variational Method," *IEEE J. Quant. Electron.*, Vol. QE-12, No. 7, 1976.
- [34] W.P. Huang and H.A. Haus, "A Simple Variational Approach to Optical Rib Waveguides," *J. Lightwave Tech.*, Vol. 9, No. 1, pp. 56-61, 1991.
- [35] C.H. Henry and B.H. Verbeek, "Solution of the Scalar Wave Equation for Arbitrarily Shaped Dielectric Waveguides by Two-Dimensional Fourier Analysis," *J. Lightwave Tech.*, Vol. 7, No. 2, pp. 308-313, 1989.
- [36] M. Munowitz and D.J. Vezzetti, "Application of the Fourier-Grid Method to Guided-Wave Problems," *J. Lightwave Tech.*, Vol. 8, No. 6, pp. 889-893, 1990.
- [37] D.J. Vezzetti and M. Munowitz, "Analysis of Finite Rib Waveguides by Matrix Methods," *J. Lightwave Tech.*, Vol. 8, No. 9, pp. 1228-1234, 1990.
- [38] R.E. Collins, Field Theory of Guided Waves, 2nd ed., IEEE Press, New York, 1991.
- [39] R.B. Dyott, J.R. Cozens, and D.G. Morris, "Preservation of Polarisation in Optical-Fibre Waveguides with Elliptical Cores," *Electron. Lett.*, Vol. 15, No. 13, pp. 380-382, 1979.
- [40] K.S. Chiang, "Geometrical Birefringence in a Class of Step-Index Fiber," *J. Lightwave Tech.*, Vol. LT-5, No. 2, pp. 737-744, 1987.
- [41] A. Kumar and R.K. Varshney, "Propagation Characteristics of Dual-Mode Elliptical-Core Optical Fibers," *Opt. Lett.*, Vol. 14, No. 15, pp. 817-819, 1989.
- [42] A. Kumar and R.K. Varshney, "Propagation Characteristics of Highly Elliptical Core Optical Waveguides: A Perturbation Approach," *Opt. and Quant. Electron.*, Vol. 16, pp. 349-354, 1984.
- [43] A. Kumar, R.K. Varshney, and K. Thyagarajan, "Birefringence Calculations in Elliptical-Core Optical Fiber," *Electron. Lett.*, Vol. 20, No. 3, pp. 112-113, 1983.
- [44] R.L. Gallawa, I.C. Goyal, and A.K. Ghatak, "Modal Properties of Circular and Noncircular Optical Waveguides," *Fiber Int. Opt.*, Vol. 11, pp. 25-50, 1992.

- [45] J.C. Campbell, "Coupling of Fibers to Ti-Diffused LiNbO₃ Waveguides by Butt-Joining," *Appl. Opt.*, Vol. 18, No. 12, pp. 2037-2040, 1979.
- [46] T. Hirata, M. Suehiro, M. Hihara, M. Dobashi, and H. Hosomatsu, "Demonstration of a Waveguide Lens Monolithically Integrated with a Laser Diode by Compositional Disordering of a Quantum Well," *IEEE Photonics Tech. Lett.*, Vol. 5, No. 6, pp. 698-700, 1993.
- [47] W.K. Burns and G.B. Hocker, "End Fire Coupling Between Optical Fibers and Diffused Channel Waveguides," *Appl. Opt.*, Vol. 16, No. 8, pp. 2048-2040, 1977.
- [48] D.G. Hall, R.R. Rice, and J.D. Zino, "Simple Gaussian-Beam Model for GaAlAs Double-Heterostructure Laser-Diode-to-Diffused-Waveguide Coupling Calculations," *Opt. Lett.*, Vol. 4, No. 9, pp. 292-294, 1979.
- [49] A.K. Ghosh, "Alignability of Optical Interconnects," *Appl. Opt.*, Vol. 29, No. 35, pp. 5253-5260, 1990.
- [50] R.G. Hunsperger, A. Yariv, and A. Lee, "Parallel End-Butt Coupling for Optical Integrated Circuits," *Appl. Opt.*, Vol. 16, No. 4, pp. 1026-1032, 1977.
- [51] Y. Yamada and M. Kobayashi, "Single-Mode Optical Fiber Connection to High-Silica Waveguide with Fiber Guiding Groove," *J. Lightwave Tech.*, Vol. LT-5, No. 12, pp. 1716-1720, 1987.
- [52] P.S. Chung and M.J. Millington, "Milled-Groove Method for Fiber-to-Waveguide Couplers," *J. Lightwave Tech.*, Vol. LT-5, No. 12, pp. 1721-1726, 1987.
- [53] N. Mekada, M. Seino, Y. Kubota, and H. Nakajima, "Practical Method of Waveguide-to-Fiber Connection: Direct Preparation of Waveguide Endface by Cutting Machine and Reinforcement Using Ruby Beads," *Appl. Opt.*, Vol. 29, No. 34, pp. 5096-5102, 1990.
- [54] H. Kaufmann et. al., "Self-Adjusted Permanent Attachment of Fibres to GaAs Waveguide Components," *Electron. Lett.*, Vol. 22, No. 12, pp. 642-643, 1986.
- [55] E.J. Murphy and T.C. Rice, "Self-Alignment Technique for Fiber Attachment to Guided Wave Devices," *IEEE J. Quant. Electron.*, Vol. QE-22, No. 6, pp. 928-932, 1986.

- [56] C.H. Bulmer, S.K. Sheem, R.P. Moeller, and W.K. Burns, "High Efficiency Flip-Chip Coupling Between Single-Mode Fibers and LiNbO_3 Channel Waveguides," *Appl. Phys. Lett.*, Vol. 37, No. 4, pp. 351-353, 1980.
- [57] Y. Cai et. al., "An Effective Method for Coupling Single-Mode Fiber to Thin Film Waveguide," *J. Lightwave Tech.*, Vol. 9, No. 5, pp. 577-583, 1991.
- [58] M. Warren et. al., "Electronic Optical Bistability in a GaAs/AlGaAs Strip-Loaded Waveguide," *Appl. Phys. Lett.*, Vol. 51, No. 16, pp. 1209-1211, 1987.
- [59] D.J. Vezzetti and M. Munowitz, "Design of Strip-Loaded Optical Waveguides for Low-Loss Coupling to Optical Fibers," *J. Lightwave Tech.*, Vol. 10, No. 5, pp. 581-586, 1992.
- [60] M.J. Robertson, S. Ritchie, and P. Dayan, "Semiconductor Waveguides: Analysis of Coupling Between Rib Waveguides and Optical Fibres," *Integrated Optical Circuit Engineering II*, Proc. SPIE, Vol. 578, pp. 184-191, 1985.
- [61] B.E. Kincaid, "Coupling of Polarization-Maintaining Optical Fibers to Ti:LiNbO_3 Waveguides with Angled Interfaces," *Opt. Lett.*, Vol. 13, No. 5, pp. 425-427, 1988.
- [62] M.L. Tuma, Chapter Entitled: "Integrated and Fiber Optic Sensors", to be published in Integrated Optics, Microstructures, and Sensors, edited by M. Tabib-Azar, Kluwer Academic Publishers, 1995.
- [63] G.N. De Brabander, J.T. Boyd, G. Beheim, "Integrated Optical Ring Resonator With Micromechanical Diaphragm for Pressure Sensing," *IEEE Photon. Tech. Lett.*, Vol. 6, No. 5, pp. 671-673, 1994.
- [64] G.N. De Brabander, J.T. Boyd, G. Beheim, "Integrated Optical Interferometer with Micromechanical Diaphragm for Pressure Sensing," *Integrated Optics and Microstructures II*, Proc. SPIE, Vol. 2291, pp. 144-148, 1994.
- [65] K.E. Petersen, "Silicon as a Mechanical Material," *Proc. IEEE*, Vol. 70, pp. 420-455, 1982.
- [66] E.D. Palik, editor, Handbook of Optical Constants of Solids, Academic Press, Orlando, 1985.

- [67] H.A. Haus and D.A.B. Miller, "Attenuation of Cutoff Modes and Leaky Modes of Dielectric Slab Structures," *IEEE J. Quant. Electron.*, Vol. QE-22, pp. 310-318, 1986.
- [68] G.N. De Brabander, J.T. Boyd, and H.E. Jackson, "Single Polarization Optical Waveguide on Silicon," *IEEE J. Quant. Electron.*, Vol. 27, No. 3, pp. 575-579, 1991.
- [69] S. Valette, S. Renard, J.P. Jadot, P. Gidon, and C. Erbeia, "Silicon-Based Integrated Optics Technology for Optical Sensor Applications," *Sensors and Actuators*, A21-A23, pp. 1087-1091, 1990.
- [70] D. Peters, K. Fischer and J. Müller, "Integrated Optics Based on Silicon Oxynitride Thin Films Deposited on Silicon Substrates for Sensor Applications," *Sensors and Actuators A*, 25-27, pp. 425-431, 1991.
- [71] D.E. Bossi, J.M. Hammer, and J.M. Shaw, "Optical Properties of Silicon Oxynitride Dielectric Waveguides," *Appl. Opt.*, Vol. 26, No. 4, pp. 609-611, 1987.
- [72] Hocker, "Fiber Optic Sensing of Pressure and Temperature," *Appl. Opt.*, Vol. 18, pp. 1445-1448.
- [73] Melles Griot Optics Guide 5, pp. 3-5 and 3-16, 1990.
- [74] C.M. Davis et. al., *Fiberoptic Sensor Technology Handbook*, Optical Technologies, Inc., Herndon, Virginia, 1986.
- [75] M.L. Tuma, "Modeling the Electric Field Profile of a Rib Waveguide," *Bull. Am. Phys. Soc.*, 1994.
- [76] T. Okoshi, Optical Fibers, Academic Press, New York, 1982.
- [77] M.J. Adams, D.N. Payne, and C.M. Ragdale, "Birefringence in Optical Fibres with Elliptical Cross-Section," *Electron. Lett.*, Vol. 15, No. 10, pp. 298-299, 1979.
- [78] Andrew Corporation, D-series elliptical fiber, 205170-820F-2.
- [79] G.R. Elion and H.A. Elion, Fiber Optics in Communication Systems, Marcel Dekker Inc., New York, New York, 1978.

- [80] M.S. Stern, P.C. Kendall, R.C. Hewson-Browne, and P.N. Robson, "Scattering Loss from Rough Sidewalls in Semiconductor Rib Waveguides," *Electron. Lett.*, Vol. 25, No. 18, pp. 1231-1232, 1989.
- [81] T. Tamir, ed., *Integrated Optics*, Topics in Applied Physics, Vol. 7, Springer-Verlag, New York, pp.45-46, 1975.
- [82] E. Mounier et. al., "Improved Loss Characteristics of Buried Waveguides," *Opt. Lett.*, Vol. 18, No. 19, pp. 1624-1626, 1993.
- [83] N.A.F. Jaeger and W.C. Lai, "Calculation of the Effective Index for Nonguiding Regions," *Appl. Opt.*, Vol. 31, No. 34, pp. 7183-7190, 1992.
- [84] A. Kumar, D.F. Clark, and B. Culshaw, "Explanation of Errors Inherent in the Effective-Index Method for Analyzing Rectangular-Core Waveguides," *Opt. Lett.*, Vol. 13, No. 12, pp. 1129-1131, 1988.
- [85] M.J. Robertson, P.C. Kendall, P.W.A. McIlroy and M.J. Adams, "The Weighted Index Method: A New Technique for Analyzing Planar Optical Waveguide," *J. Lightwave Tech.*, Vol. 7, pp. 2105-2111, 1989.
- [86] A. Weisshaar and J. Li, Dept. of Electrical and Computer Engineering, Oregon State University, Oregon, FORTRAN programs written to determine propagation characteristics of optical waveguides.
- [87] R.G. Hunsperger, *Integrated Optics: Theory and Technology*, 2nd ed., New York, Springer Verlag, 1982.
- [88] J. Albert and G.L. Yip, "Insertion Loss Reduction Between Single-Mode Fibers and Diffused Channel Waveguides," *Appl. Opt.*, Vol. 27, No. 23, pp. 4837-4843, 1988.
- [89] M.L. Tuma and G. Beheim, "Calculated Coupling Efficiency Between and Elliptical-Core Optical Fiber and a Silicon Oxynitride Rib Waveguide," *Proc. SPIE* , Vol. 2383, pp. 199-210, 1995.

REPORT DOCUMENTATION PAGE			Form Approved OMB No. 0704-0188	
Public reporting burden for this collection of information is estimated to average 1 hour per response, including the time for reviewing instructions, searching existing data sources, gathering and maintaining the data needed, and completing and reviewing the collection of information. Send comments regarding this burden estimate or any other aspect of this collection of information, including suggestions for reducing this burden, to Washington Headquarters Services, Directorate for Information Operations and Reports, 1215 Jefferson Davis Highway, Suite 1204, Arlington, VA 22202-4302, and to the Office of Management and Budget, Paperwork Reduction Project (0704-0188), Washington, DC 20503.				
1. AGENCY USE ONLY (Leave blank)		2. REPORT DATE October 1995		3. REPORT TYPE AND DATES COVERED Technical Memorandum
4. TITLE AND SUBTITLE Feasibility of Coupling Between a Single-Mode Elliptical-Core Fiber and a Single Mode Rib Waveguide Over Temperature			5. FUNDING NUMBERS WU-None	
6. AUTHOR(S) Margaret L. Tuma				
7. PERFORMING ORGANIZATION NAME(S) AND ADDRESS(ES) National Aeronautics and Space Administration Lewis Research Center Cleveland, Ohio 44135-3191			8. PERFORMING ORGANIZATION REPORT NUMBER E-9950	
9. SPONSORING/MONITORING AGENCY NAME(S) AND ADDRESS(ES) National Aeronautics and Space Administration Washington, D.C. 20546-0001			10. SPONSORING/MONITORING AGENCY REPORT NUMBER NASA TM-107078	
11. SUPPLEMENTARY NOTES This report was submitted as a dissertation in partial fulfillment of the requirements for the degree Doctor of Philosophy to the University of Akron, Akron, Ohio, August 1995. Responsible person, Margaret L. Tuma, organization code 2540, (216) 433-8665.				
12a. DISTRIBUTION/AVAILABILITY STATEMENT Unclassified - Unlimited Subject Category 74 This publication is available from the NASA Center for Aerospace Information, (301) 621-0390.			12b. DISTRIBUTION CODE	
13. ABSTRACT (Maximum 200 words) To determine the feasibility of coupling the output of an optical fiber to a rib waveguide in a temperature environment ranging from 20°C to 300°C, a theoretical calculation of the coupling efficiency between the two was investigated. This is a significant problem which needs to be addressed to determine whether an integrated optic device can function in a harsh temperature environment. Because the behavior of the integrated-optic device is polarization sensitive, a polarization-preserving optic fiber, via its elliptical core, was used to couple light with a known polarization into the device. To couple light energy efficiently from an optical fiber into a channel waveguide, the design of both components should provide for well-matched electric field profiles. The rib waveguide analyzed was the light input channel of an integrated-optic pressure sensor. Due to the complex geometry of the rib waveguide, there is no analytical solution to the wave equation for the guided modes. Approximation or numerical techniques must be utilized to determine the propagation constants and field patterns of the guide. In this study, three solution methods were used to determine the field profiles of both the fiber and guide: the effective-index method (EIM), Marcattili's approximation, and a Fourier method. These methods were utilized independently to calculate the electric field profile of a rib channel waveguide and elliptical fiber at two temperatures, 20°C and 300°C. These temperatures were chosen to represent a nominal and a high temperature that the device would experience. Using the electric field profile calculated from each method, the theoretical coupling efficiency between the single-mode optical fiber and rib waveguide was calculated using the overlap integral and results of the techniques compared. Initially, perfect alignment was assumed and the coupling efficiency calculated. Then, the coupling efficiency calculation was repeated for a range of transverse offsets at both temperatures. Results of the calculation indicate a high coupling efficiency can be achieved when the two components were properly aligned. The coupling efficiency was more sensitive to alignment offsets in the y direction than the x, due to the elliptical modal profile of both components. Changes in the coupling efficiency over temperature were found to be minimal.				
14. SUBJECT TERMS Coupling efficiency; Rib waveguide; Elliptical-core fiber; Effective-index method; Marcattili's method; Fourier method			15. NUMBER OF PAGES 126	
			16. PRICE CODE A07	
17. SECURITY CLASSIFICATION OF REPORT Unclassified	18. SECURITY CLASSIFICATION OF THIS PAGE Unclassified	19. SECURITY CLASSIFICATION OF ABSTRACT Unclassified	20. LIMITATION OF ABSTRACT	

**National Aeronautics and
Space Administration
Lewis Research Center
21000 Brookpark Rd.
Cleveland, OH 44135-3191**

**Official Business
Penalty for Private Use \$300**

POSTMASTER: If Undeliverable — Do Not Return

